

RICE UNIVERSITY

**Studies of one- and two-photon photoassociative  
spectroscopy using ultracold strontium**

by

**James Allen Aman**

A THESIS SUBMITTED  
IN PARTIAL FULFILLMENT OF THE  
REQUIREMENTS FOR THE DEGREE

**Doctor of Philosophy**

APPROVED, THESIS COMMITTEE:

---

Thomas C. Killian, Chair  
Professor of Physics and Astronomy

---

Randall G. Hulet  
Fayez Sarofim Professor of Physics and  
Astronomy

---

Kevin F. Kelly  
Associate Professor of Electrical and  
Computer Engineering

Houston, Texas

April, 2019

## ABSTRACT

Studies of one- and two-photon photoassociative spectroscopy using ultracold  
strontium

by

James Allen Aman

”Lorem ipsum dolor sit amet, consectetur adipiscing elit, sed do eiusmod tempor  
incididunt ut labore et dolore magna aliqua. Ut enim ad minim veniam, quis nostrud  
exercitation ullamco laboris nisi ut aliquip ex ea commodo consequat. Duis aute irure  
dolor in reprehenderit in voluptate velit esse cillum dolore eu fugiat nulla pariatur.  
Excepteur sint occaecat cupidatat non proident, sunt in culpa qui officia deserunt  
mollit anim id est laborum.”

## Acknowledgments

It is difficult to over state how much I have learned during my time in grad school. Not only pertaining to physics, engineering, and computer science but also about myself, my friends, and my communities.

I owe so much to Brian DeSalvo for being an inspiration. It was Brian who showed me my first Bose-Einstein condensate

I bugged him relentlessly as a naive undergraduate with so many questions.

# Contents

Abstract	ii
Acknowledgments	iii
List of Illustrations	x
List of Tables	xii
<b>1 Introduction</b>	<b>1</b>
1.1 Few-body physics . . . . .	1
1.2 Halo molecules . . . . .	2
1.3 Properties of strontium . . . . .	2
1.4 Thesis Outline . . . . .	3
<b>2 The Neutral apparatus</b>	<b>5</b>
2.1 Experimental procedure . . . . .	6
2.1.1 Characteristic trapping performance . . . . .	13
2.2 Vacuum system and atom source . . . . .	14
2.3 Laser systems . . . . .	24
2.3.1 Wideband cooling stage: 461 nm . . . . .	24
2.3.1.1 Overview . . . . .	24
2.3.1.2 922 nm master . . . . .	26
2.3.1.3 Zeeman subsystem . . . . .	27
2.3.1.4 MOT subsystem . . . . .	28
2.3.1.5 Changing isotopes . . . . .	28
2.3.2 Repumping: 481 nm . . . . .	29
2.3.3 Narrowband cooling stage: 689 nm . . . . .	29

2.3.3.1	Overview . . . . .	29
2.3.3.2	689 nm Master . . . . .	31
2.3.3.3	Boson subsystem . . . . .	31
2.3.3.4	Fermion subsystem . . . . .	31
2.3.4	Optical dipole trap: 1064 nm . . . . .	32
2.3.4.1	Alignment Procedure . . . . .	33
2.3.4.2	Trap frequency calibration . . . . .	35
2.3.4.3	Modeling the potential . . . . .	36
2.3.5	Optical lattice trap: 532 nm . . . . .	36
2.3.5.1	Alignment procedure . . . . .	36
2.3.5.2	Lattice depth calibration . . . . .	37
2.3.5.3	Modeling the potential . . . . .	37
2.3.6	Optical toolbox . . . . .	37
2.3.6.1	Absorption imaging system . . . . .	37
2.3.6.2	Chirped blow away pulser . . . . .	40
2.3.6.3	Highly tunable 689 nm spectroscopy system . . . . .	40
2.3.6.4	Spin-manipulation laser with dynamic polarization control . . . . .	41
2.4	Experimental control and electronics . . . . .	41
2.4.1	Computer control and measurement system . . . . .	41
2.4.2	Ancillary laboratory systems . . . . .	41
2.4.2.1	MOT coils . . . . .	41
2.4.2.2	Trim coils . . . . .	41
2.4.2.3	Zero crossing AC line trigger . . . . .	42
2.4.2.4	Pneumatic actuated mirror mounts . . . . .	42
<b>3</b>	<b>Photoassociation in ultracold gases</b>	<b>43</b>
3.1	Introduction . . . . .	43

3.2	Theoretical description of trapped boson gases . . . . .	45
3.2.1	Extracting data from column densities . . . . .	49
3.3	Characterizing collisions . . . . .	55
3.3.1	Classical . . . . .	56
3.3.2	Single channel scattering . . . . .	56
3.3.2.1	Low energy results . . . . .	57
3.3.3	Multichannel scattering . . . . .	59
3.4	Modeling of photoassociation lineshapes . . . . .	65
3.4.1	One-photon excitation of free to bound transitions . . . . .	66
3.4.1.1	PAS near narrow intercombination transitions . . . . .	66
3.4.2	Extension to two-color spectra . . . . .	67
<b>4</b>	<b>Binding energy of the <math>^{86}\text{Sr}_2</math> halo molecule</b>	<b>70</b>
4.1	Probing the ground state potential . . . . .	70
4.2	Experimental setup . . . . .	74
4.2.1	Photoassociation . . . . .	81
4.2.2	Consideration of the trap depth . . . . .	83
4.3	Theoretical description . . . . .	84
4.4	Spectral fitting and determination of energy shifts . . . . .	89
4.4.1	AC Stark shift due to excitation lasers . . . . .	91
4.4.2	Density-dependent frequency shift . . . . .	94
4.4.3	AC Stark Shift due to Trapping Lasers . . . . .	96
4.5	Unperturbed halo binding energy . . . . .	98
4.6	Calculating the bound-bound Frank-Condon factor . . . . .	99
<b>5</b>	<b>Strongly coupled PAS of a weakly bound molecule</b>	<b>110</b>
5.1	Introduction . . . . .	110
5.2	Experimental methods . . . . .	110
5.3	Three level model . . . . .	111

5.4	Resonance positions . . . . .	111
5.5	Lineshape . . . . .	111
5.6	Emergence of multi-photon Raman coupling . . . . .	112
<b>6</b>	<b>Progress towards studies of quantum magnetism</b>	<b>113</b>
6.1	532 nm optical lattice: installation and characterization . . . . .	113
6.1.1	Background . . . . .	114
6.1.2	Setup . . . . .	120
6.1.3	Measurement and results . . . . .	121
6.1.3.1	Kaptiza-Dirac Scattering . . . . .	121
6.1.3.2	Heating of a quantum degenerate gas . . . . .	123
6.2	Spin manipulation of $^{87}\text{Sr}$ . . . . .	126
6.3	Search for narrowline PA molecules using various spin mixtures . . .	126
<b>7</b>	<b>Conclusion</b>	<b>127</b>
<b>Bibliography</b>		<b>129</b>
<b>Appendices</b>		<b>139</b>
<b>A</b>	<b>Two-particle momentum probability distribution</b>	<b>140</b>
A.1	Standard form . . . . .	140
A.2	Truncated form . . . . .	141
<b>B</b>	<b>Imagefit analysis routine</b>	<b>146</b>
B.1	Background removal . . . . .	146
B.1.1	Principal component analysis . . . . .	146
B.1.2	Comparison of PCA implementations . . . . .	148
B.2	Fitting the spatial distribution . . . . .	148

B.3	Evaluating fit parameters . . . . .	148
B.3.1	Writing new plug-ins . . . . .	148
B.3.2	Suggested improvement . . . . .	148
<b>C</b>	<b>neuKLEIN - Killian lab experimental interface</b>	<b>150</b>
C.1	Labview code . . . . .	150
C.2	FPGA code . . . . .	150
C.3	Possible future improvements . . . . .	151
<b>D</b>	<b>Experimental control computer hardware</b>	<b>152</b>
D.1	Overview of status . . . . .	152
D.2	Migration to a new machine . . . . .	152
D.3	PixelFly camera system . . . . .	152
<b>E</b>	<b>Neutral apparatus</b>	<b>153</b>
E.1	Opening vacuum - data and process . . . . .	153
E.2	Nozzle redesign - neuNozzle 2018 . . . . .	153
<b>F</b>	<b>Gaussian Beam Programs</b>	<b>155</b>
F.1	Simple beam propagation . . . . .	155
F.2	Laser beam profile fitting . . . . .	155
F.2.1	Data taking template . . . . .	155
<b>G</b>	<b>Concise derivation of effective volumes</b>	<b>156</b>
<b>H</b>	<b>Repair of 922 Lynx master</b>	<b>157</b>
<b>I</b>	<b>Custom circuitry</b>	<b>158</b>
I.1	AC line zero crossing trigger . . . . .	158
I.2	Hard drive shutters . . . . .	158

I.3	Power locks . . . . .	158
I.4	Photodiodes . . . . .	158
I.5	Infinite sample and hold . . . . .	158
I.5.1	Reduced intensity fluctuations for sub-hertz exposures . . . . .	158
<b>J</b>	<b>Miscellaneous tips and tricks</b>	<b>159</b>
J.1	Alignment of GHz AOM . . . . .	159
J.2	Using the Picoscope in Labview(TM) . . . . .	159
J.3	Liquid crystal retarder . . . . .	159
J.4	Newport(TM) optomotion control . . . . .	159
J.5	Fast analog lock for 689 nm . . . . .	159
J.6	Porta CoM technique . . . . .	159
J.7	Measuring Rabi frequencies . . . . .	159
J.8	CAD drawing for shallow angle Bragg setup . . . . .	159

# Illustrations

1.1 Properties of strontium. Left: Natural abundances and s-wave scattering lengths for all mixtures of Sr. Right: Simplified energy level diagram of Sr showing the relevant states used for trapping and cooling of the atomic gas . . . . .	2
1.2 Properties of strontium . . . . .	3
2.1 Complete Neutral apparatus vacuum system . . . . .	16
2.2 Source assembly - side view . . . . .	17
2.3 Source assembly - rear view . . . . .	17
2.4 2D collimator assembly . . . . .	18
2.5 Cryo tower assembly . . . . .	18
2.6 Typical fluorescence of Zeeman beam looking down 2D collimator . .	25
2.7 Ablating strontium coating from window . . . . .	26
3.1 Ballistic expansion of particles . . . . .	50
3.2 Strontium interatomic wavefunctions . . . . .	59
3.3 Schematic representation of a Feshbach resonance . . . . .	61
4.1 Strontium PAS potential . . . . .	73
4.2 Strontium two-photon photoassociation . . . . .	75
4.3 Schematic of PAS light generation . . . . .	77
4.4 Histogram of PAS beam intensity variation . . . . .	79

4.5	Characteristic view of the PA beatnote . . . . .	80
4.6	PAS laser setup . . . . .	81
4.7	Variation of 1064 nm trap depth . . . . .	90
4.8	Variation of 689 nm excitation . . . . .	92
4.9	Fit of 689 nm AC Stark shift . . . . .	93
4.10	Measurement of halo state susceptibility, $\chi_{1064}$ . . . . .	97
4.11	Determination of 86 scattering length . . . . .	100
4.12	Variation of halo susceptibility as a function of $\Delta_1$ . . . . .	101
4.13	Estimate of bound-bound coupling via isolated resonance model . . .	104
6.1	1D band structure as a function of lattice depth . . . . .	116
6.2	Calculated interaction energies and tunneling rates for each isotope of strontium . . . . .	119
6.3	Evolution of plane wave population using Kapitza-Dirac . . . . .	122
6.4	Evolution of condensate fraction over time after adiabatically ramping on the lattice to $9 E_r$ . a,b) Comparison of total number and condensate fraction for a sample held in the optical dipole trap (red squares) or in a deep lattice (blue circles). c) Time of flight images after ramping on the lattice and diabatically projecting back to plane wave states. . . . .	123
6.5	Observation of driven sideband transitions . . . . .	125

## **Tables**

# Chapter 1

## Introduction

The ability to engineer and manipulate quantum states lies at the heart of modern atomic physics experiments using ultracold gases [? ? 14, 44, 39? ]. Two important tools for this pursuit are Feshbach resonances [16, 37] and optical lattices [? ]. This proposal will detail our recent work building and characterizing a three-dimension optical lattice for use with ultracold and quantum degenerate gases of neutral strontium. Furthermore, we will present the first experiment we hope to pursue with the optical lattice; the creation of Feshbach molecules using an optical Feshbach resonance. We will also briefly discuss other future plans such as the production of highly excited ground state  $\text{Sr}_2$  dimers through adiabatic internal state transfer.

Should probably mention somewhere that this is long-range PA, in contrast to short-range stuff being explored now.

Julienne form of the corss section 6.16 in CM. Discuss how important the phase space density is, the timescale for interactions, and the complex

[1]

### 1.1 Few-body physics

field of photoassociation in ultracold gases, wherein studies of molecular structure have revealed the most accurate descriptions of atomic interactions and have become

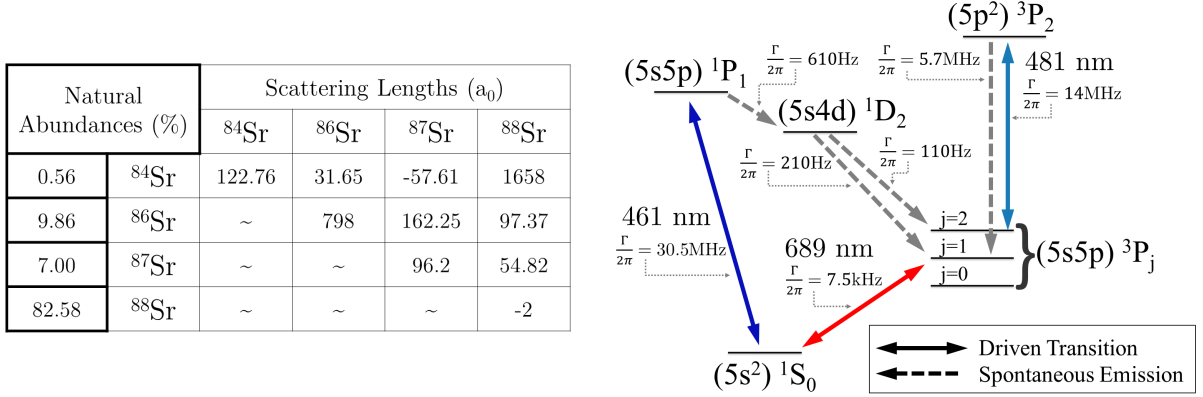


Figure 1.1 : Properties of strontium. Left: Natural abundances and s-wave scattering lengths for all mixtures of Sr. Right: Simplified energy level diagram of Sr showing the relevant states used for trapping and cooling of the atomic gas

a fundamental probe of the ultracold toolbox [35].

## 1.2 Halo molecules

Mostly studied in helium

Comes from bound state of the dirac potential. Unsure how much detail I want right here

Check out CM Juleinne pg 229. He has a ref

## 1.3 Properties of strontium

The experiments in this proposal will be realized using an ultracold gas of atomic strontium. Fig. 1.3 shows all of the stable isotopes of strontium, their natural abundance, as well as their inter-particle scattering lengths. The isotopic differences in strontium have important implications for their use in certain experiments. For example, none of the bosonic isotopes of strontium ( $^{88}\text{Sr}$ ,  $^{86}\text{Sr}$ , or  $^{84}\text{Sr}$ ) display hyperfine

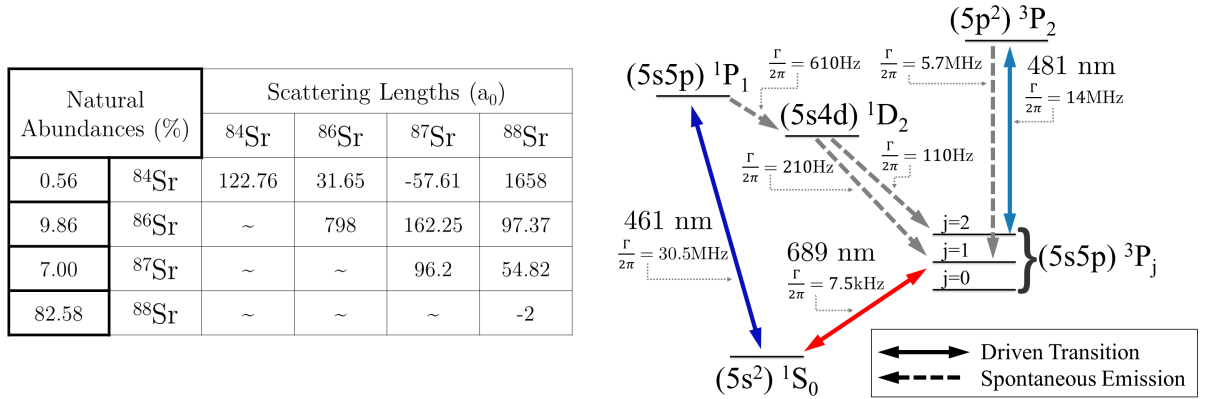


Figure 1.2 : Properties of strontium

Properties of strontium. Left: Natural abundances and s-wave scattering lengths for all mixtures of Sr. Right: Simplified energy level diagram of Sr showing the relevant states used for trapping and cooling of the atomic gas

structure since they have no nuclear spin,  $\mathbf{I} = 0$ . However, the fermionic isotope  $^{87}\text{Sr}$  has a large nuclear spin,  $\mathbf{I} = 9/2$ , which makes it an ideal candidate for exploring exotic phases of quantum magnetism [7? , 15]. In the studies presented in this proposal, we are sensitive to the isotopic shifts of the bosonic photoassociation lines along the  $^1S_0 \rightarrow ^3P_1$  transition as well as the various interspecies scattering lengths.

## 1.4 Thesis Outline

”Lorem ipsum dolor sit amet, consectetur adipiscing elit, sed do eiusmod tempor incididunt ut labore et dolore magna aliqua. Ut enim ad minim veniam, quis nostrud exercitation ullamco laboris nisi ut aliquip ex ea commodo consequat. Duis aute irure dolor in reprehenderit in voluptate velit esse cillum dolore eu fugiat nulla pariatur. Excepteur sint occaecat cupidatat non proident, sunt in culpa qui officia deserunt

mollit anim id est laborum.”

$$V(x) = V_{lat} \sin^2(k_L x) \quad (1.1)$$

## Chapter 2

### The Neutral apparatus

The Neutral apparatus was one of the pioneering experiments for the trapping, cooling, and creation of quantum degenerate gases of neutral strontium. As such, there is a plethora of previous theses and publications which extensively outline the details for how to achieve these goals. refs. In particular, we refer the reader to the PhD theses of previous Killian lab students: Francisco Camargo, Brian DeSalvo, Mi Yan, Pascal Mickelson, Natali Martinez de Escobar, and Sarah Nagel.

Building upon this previous work, this chapter will forego an extensive review of the basic laser cooling techniques for strontium. We refer the reading to the extensive works for a formal discussion of the theory behind laser cooling and trapping.

Instead, we will focus on the systems and processes which are most crucial to the operation of the experiment with an emphasis on technical findings and changes which remain, as of yet mostly, undocumented.

Since it has been 7 years since the last broad apparatus overview and the experiment has grown significantly in complexity, the goal of this chapter is to serve as a reference for future work and students. As such, the following is highly technical and will provide an in-depth review of the operation and current status of the Neutral apparatus.

Where appropriate we will refer the reader to the relevant thesis or published work. Future experiments on the Neutral apparatus aim to explore quantum magnetism

using strontium 87 and as such several key changes have been made to the 461 locking and 689 trapping systems which will be detailed below.

Say something about referring to the isotopes by their number for shorthand.

This chapter will begin with a brief overview of our trapping procedure in order to contextualize the remaining sections which focus on the hardware implementations used.

## 2.1 Experimental procedure

Our experiments begin by cooling and trapping atomic strontium utilizing well-established atomic physics techniques [59? , 31, 49, 48, 41? ? , 5, 46? , 62].

Fig. 1.3 shows the simplified energy level diagram employed in our cooling process. Once cooled, we typically obtain bulk samples in an optical dipole trap containing on the order of  $10^6$  atoms at temperatures  $< 1\mu\text{K}$  and densities between  $10^{12} - 10^{15} \text{ cm}^{-3}$  depending upon the isotope. Samples of ultracold atoms can then be directly loaded into an optical lattice potential by ramping up the intensity of the laser beams forming the optical lattice.

Reference stellmers thesis, natalis thesis, and pascal for strontium colling and trapping

Brians thesis refs - [27, 28, 29, 30, 31, 32] for cooling and trapping

This section will outline the experimental procedure followed to laser cool and trap atoms. This process has remained relatively stable throughout the years so we provide only a brief overview and reserve the detailed discussion to the relevant sections following this overview.

that begin nearly every measurement taken on the Neutral machine

The procedure presented here is generally followed for trapping all isotopes of strontium with the major difference being timescales and of course laser frequencies.

Trapping of the bosonic isotopes of strontium is nearly an identical procedure while fermionic 87 poses a significant challenge due to its high nuclear spin when attempting to cool on the intercombination transition.

We refer the interested reader to the fermion portion of section 2.7.3 in the PhD thesis of Simon Stellmer for a well written discussion of the relevant physics of trapping  $^{87}\text{Sr}$  in the red MOT.

The previous work of Brian DeSalvo on the Neutral apparatus created the first quantum degenerate gas of Sr 87 and interested readers can find a thorough discussion of the nua

Over the time frame of this PhD, we have performed experiments using all four common isotopes of strontium.

In the case of switching

**FRANCISCO** The experiments described in this thesis are performed using ultracold samples of  $^{84}\text{Sr}$  in either a thermal or BEC phase. To obtain such samples, we go through multiple stages of laser cooling and trapping. First, we utilize the 461nm  $(5s2)1S0 - (5s5p)1P1$  broad-line transition to reach 1mK (Fig. 2.1) in a Magneto-Optical Trap (MOT) in combination with a magnetic trap [48]. Subsequently we load a narrow-line MOT using the 689nm  $(5s2)1S0 - (5s5p)3P1$  transition cooling down to 2 muK [49]. Finally, a recycled-beam optical dipole trap (ODT) [50, 51] is turned on, which can trap millions of atoms at 2mK. We conduct experiments at this stage but may also choose to begin an evaporative cooling trajectory which results in BEC

samples of several hundred thousand atoms.

Room temperature strontium is a metallic solid. As such, we load strontium into an ‘oven- nozzle’ which is heated to 425 C, metallic pellets sublime resulting in gaseous strontium emitting from the nozzle with a mean velocity of about 450 m/s. We achieve trapping of these atoms by employing the 461nm transition in three stages (Fig. 2.2): a 2D-Collimator, a Zeeman Slower, a broad-line MOT (all using the 461 nm, 30.5MHz wide transition). Additionally, there is a decay path to the magnetically trappable 3PJ manifold from the 1P1 line. These atoms are collected by the quadrupole MOT field and are repumped back to the ground state for further cooling using the 481nm (5s5p)3P2 - (5p2)3P2 transition.

Immediately following the output of the oven, a 2D-Collimator cools the atoms via optical molasses in the radial direction. A retro-reflected beam incident on the atoms in two orthogonal directions perpendicular to the direction of the atom-beam propagation is used. By cooling in the transverse direction, we greatly increase the flux of atoms that will enter the trapping region of the MOT. We observe approximately an order-of-magnitude increase in the loading rate of the MOT with the inclusion of the 2D-Collimator red-detuned by half the natural linewidth.

Next, the atomic beam enters the Zeeman Slower where the mean axial velocity is reduced from about 450 m/s to about 30 m/s, slow enough for the MOT to capture. Using an acousto-optical modulator (AOM), the Zeeman laser beam is red-detuned by 18 times the natural linewidth of the transition in order to avoid scattering in the region of the MOT, therefore a spin-flip configuration is implemented such that somewhere along the path of the Zeeman slower the direction of magnetic field is reversed. The relative direction of Zeeman Slower fringe field compared to the on-

axis field of the MOT can have a significant impact. We find that an anti-parallel configuration is optimal by a factor of apprx 2.

The output of the Zeeman Slower leads to the MOT region. The MOT light is set at a red-detuning of 1.8 times the linewidth of the 461nm transition. A large loss channel is present due to decay from the  $(5s5p)1P1$  state to  $(5s4d)1D2$  and subsequently to the  $(5s5p)3P1,2$  states. However, the low-field seeking  $3P2$  states are trapped by the anti-Helmholtz magnetic field of the MOT. These atoms can therefore be reintroduced into the main cycling transition by repumping with a 481nm laser to the  $(5p2)3P2$  state. Experimentally we find that it is optimal to repump for 50ms after having loaded the magnetic trap for several seconds instead of having the repump beam on during the whole loading procedure. Details of the repumping laser can be found in Pakorn Wongwaitayakornkul's undergraduate thesis. For a 2 s load time, this scheme yields  $20 \times 10^6$  atoms of  $^{84}\text{Sr}$  near the Doppler temperature limit. Although  $^{84}\text{Sr}$  is the least abundant isotope, at 0.6 perc, and we could instead generate much larger MOT sample with the other isotopes, we chose to use  $^{84}\text{Sr}$  for these experiments due to the 123a0  $^{84}\text{Sr}$  -  $^{84}\text{Sr}$  scattering length, which is ideal for evaporative cooling. More details on our broad-line cooling and trapping scheme, including a description of the 461nm laser system, can be found in Ref. [48].

Having produced a trapped gas of ten's of millions of atoms at about 2mK, the next stage of cooling consistses of a narrow-line MOT. Utilizing the  $(5s2)1S0$  -  $(5s5p)3P1$  transition enables us to reach a much colder temperature because of a reduction in line-width of over three orders of magnitude compared to the broad-line MOT. The theoretical temperature limits due to the Doppler limit and atom recoil are comparable at about 200 nK, however, experimentally we only cool to about 1 muK which

is sufficient to subsequently transfer atoms to the ODT. To bridge the gap between broadline MOT and initial ODT temperaures, the narrowline MOT must capture apprx 2mK atoms and cool them to apprx 1 muK. To achieve this, we dynamically change the trap parameters. Initially, the narrow-line MOT begins with large laser intensity compared to the saturation intensity, far red-detuning compared to the transition line-width, and a dither of the laser frequency that is also large compared to the line-width. This ensures that the initial range of atom velocities at the end of the broad-line MOT will experience cooling and trapping on the 689nm transition. As cooling takes effect and temperature falls, these experimental parameters follow suit and are changed to address a narrower velocity distribution, ultimately yielding apprx 1 muK samples of about two million atoms. Details of our narrow-line cooling MOT can be found in Ref. [49].

We load atoms from the narrow-line MOT into a 1064nm infra-red (IR) ODT with two perpendicularly crossed paths (Fig. 2.3). Each path is made up of three laser beams co- propagating with 10's of microns of separation [52], yielding a ‘Top-Hat’ laser profile. After loading the Top-Hat ODT, the intensity of the outer two beams linearly decrease to zero over 400ms while maintaining constant intensity in the center. At this juncture, apprx 106 atoms at apprx 2 muK are trapped in the ODT and represent a cold thermal sample which we have used for several of our measurements. Further cooling via forced evaporation can be employed, which enables an increase in phase-space density sufficient enough to create Bose-Einstein condensates (BEC) of  $^{84}\text{Sr}$  [19, 20]. We produce samples where 75 perc of trapped atoms are in the BEC phase. Several hundred thousand atoms enter the condensate phase at a peak number density of apprx  $4 \times 10^{14} \text{ cm}^{-3}$ .

BRIAN For laser trapping and cooling, we need to work with gaseous Sr, so we begin by heating a sample in an oven up to approx 350C to obtain a significant vapor pressure. Directly out of the nozzle, the atoms undergo a stage of two dimensional optical molasses to further collimate the beam. After the transverse cooling, the atoms are decelerated in a Zeeman slower to velocities suitable for capture in a magneto-optical trap (MOT). These initial cooling stages, and our first stage MOT, utilize the 1S0 1P1 transition in Sr, which requires a laser operating at a wavelength of 461 nm. The broad linewidth of the transition results in a large saturation intensity, 40.5 mW/cm<sup>2</sup>, so laser powers on the order of 100 mW are necessary for the initial cooling stages. Our system is based on frequency doubling of IR diode lasers, which can provide the power necessary. Laser cooling on the 1S0 1P1 transition is ideal for the initial cooling stage owing to the fast cooling rate and large capture velocity which results from the short lifetime of the excited state and short wavelength of the transition. This lifetime yields a broad (30.5 MHz) linewidth. However, laser cooling on this transition also comes with the significant drawback that the Doppler temperature is high by ultracold atom standards, TD = 1 mK. The lack of nuclear spin in bosonic Sr means that sub-Doppler cooling is not possible in this system. Therefore the temperature of the 461 nm MOT cannot be reduced below this limit. There is a leak in this transition which we can take advantage of. The 1S0 1P1 transition is not completely closed, and atoms from the 1P1 state can decay via the 1D2 state to the 3P2 state with a probability of  $16 \times 10^{-5}$ . This state is metastable and has a long lifetime, limited in experiment by blackbody radiation to about 25 s. Within the 3P2 manifold, atoms in low-field seeking mj states can be magnetically trapped by the quadrupole field of the MOT where they remain for their lifetime while being dark to

the cooling light [33]. The observed 25 s lifetime of this trap is orders of magnitude longer than the lifetime of the MOT, which allows us to use long loading times. While the loading rate of atoms into the magnetic trap is clearly reduced compared to the loading rate of the MOT (we need to scatter 105 photons for an atom to end up in the magnetically trapable state), the loss rate is reduced further. After this collection phase, the atoms are returned to the ground state via a repumping transition. Within the last few years, we have begun repumping along the  $(5s5p)3P_2 - (5p2)3P_2$  using a 481 nm laser. This transition has a few advantages over other schemes used so far for repumping Sr. Other schemes include using 497 nm [34] or 3  $\mu\text{m}$  [35], which require expensive laser systems for such an uninteresting purpose. Another popular choice is the combination of 707 nm and 679 nm. While these are less expensive diode lasers, the requirement of two independent laser systems makes this scheme more complicated than desired. By using the  $(5s5p)3P_2 - (5p2)3P_2$  transition, only a single diode laser is necessary. say something about isotope shifts of these other repumping transitions?. With the atoms retuned to the ground state, we employ a second MOT operating on the  $1S_0 - 3P_1$  transition which features a narrow 7.5 kHz linewidth. This significantly reduces the Doppler temperature to a few hundred nK and in practice we regularly obtain samples between 1 - 2  $\mu\text{K}$  after 200 ms change this of laser cooling. Following this cooling stage, we load atoms into a crossed optical dipole trap (ODT). The ODT is derived from a multimode 18 W IPG fiber laser at 1064 nm. add footnote about this laser dying. After an a period of free evaporation being held in the ODT, we begin evaporative cooling for to produce our final sample of ultracold or quantum degenerate gases. The end of the evaporation typically marks the beginning of the experimental phase and the divergence of our protocol into the

specific procedures necessary. These may include ramping or pulsing on lattice beams, exciting a collective mode, probing the gas with PAS laser, shelving, etc. Once we have completed the experimental phase, we perform absorption imaging along the strong 461 nm transition to determine the characteristics of the gas. Typically we perform absorption imaging following a time-of-flight so as to measure both the atom number and temperature at the time of release. However, this is not strictly necessary and certain experiments may result in low atomic densities which are not amenable to a time-of-flight due to their low optical depth.

NATALI Atoms in the 3P2 state (8.3 min. lifetime [77]), however, can be trapped by the quadrupole field of the MOT [78, 79, 80, 65] where they do not scatter 461 nm light. As the 461 nm MOT cooling stage continues, atoms keep accumulating in the 3P2 dark state.

### 2.1.1 Characteristic trapping performance

The following subsections outline typical trapping parameters and performance for each isotope. Note, that while we have demonstrated the ability to dual trap 84 and 87, full characterization and optimization of this process is currently the subject of future research.

#### <sup>84</sup>Sr

Timing diagram Blue MOT Repump Broadband red MOT Single Freq red MOT IR loading Evaporation: typically around 1 to 7s Time of flight Imaging Typical settings table Performance table

$^{86}\text{Sr}$

$^{87}\text{Sr}$

Remember the switch to single frequency

What about values for the experiments?

would like to put a timing diagram here showing a typical timing sequence for 84,  
86, and 87

Where the heck does that calibration for the MOT coils come from??

## 2.2 Vacuum system and atom source

### Overview

The Neutral apparatus is built around a stainless steel chamber positioned above the table to facilitate optical access.

Pressuess within this chamber ar typically of the order blah

Details on the original construction can be found in Natali's thesis so this section is mainly devoted to covering the few changes which have occured in the intervening years.

The vacuum system can be decomposed into several subcomponents, namely

1. Atom source (assembly of atom oven housed within the source chamber)
2. 2D collimator
3. Zeeman slower
4. Science chamber

## 5. Cryo tower

Figure 2.1 shows a complete overview of these assemblies which form our vacuum system. Figures 2.2 - 2.5 also show various views of the atom source & 2D collimator and cryo tower assemblies. Note the red markers and green arrows denote the positions of heater bands and thermo-couples respectively. For more information please see App. E.

From left to right, the system starts with an oven source based around a custom nozzle design which uses a rod heater to vaporize elemental strontium. Next, there is a 6 way tee used for the optical molasses step which we refer to as the 2D collimator. From here atoms pass through a narrow differential pumping tube and into the entry port of the Zeeman slower where a majority of the laser cooling takes places. Following the Zeeman slower, atoms enter the science chamber where a plethora of lasers are used to manipulate and probe their behavior. Chief among these are the MOT sequences and the high intensity far off-resonant optical dipole traps used for the final stage of confinement. Lastly, the body of the science chamber is supported by the cryo tower which houses a titanium sublimation cartridge (model: somethgin) and is the entry point for the Zeeman laser. It is worth explicitly noting that this Zeeman window is necessarily directly opposite the atomic source and therefore is subject to a flux of hot atomic strontium which will eventually coat the vacuum side.

While the source and science chamber have remained largely unchanged since the publication of Natali's thesis, several key improvements and events have occurred over the last few years\*. These differences will be the subject of our discussion in the

---

\*As of April 2019, the most up to date CAD drawing for the Neutral appa-

Scattering Lengths ( $a_0$ )		
$^{86}\text{Sr}$	$^{87}\text{Sr}$	$^{88}\text{Sr}$
31.65	-57.61	1658
798	162.25	97.37
~	96.2	54.82
~	~	-2

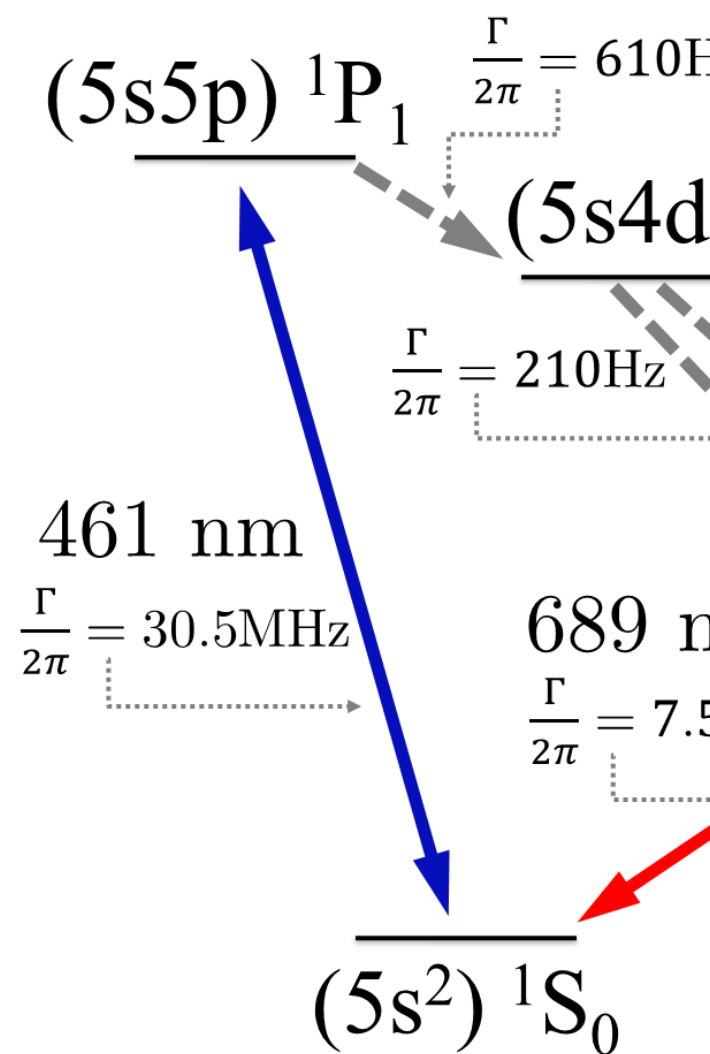


Figure 2.1 : Complete Neutral apparatus vacuum system

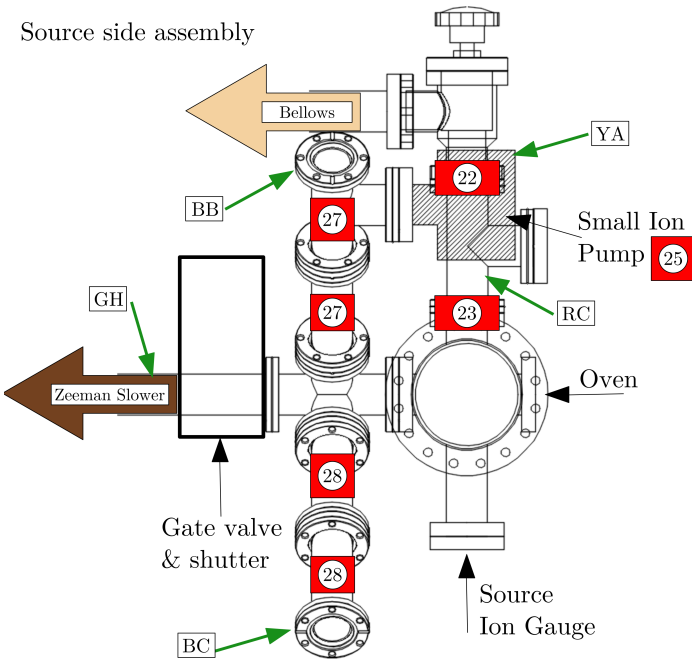


Figure 2.2 : Source assembly - side view

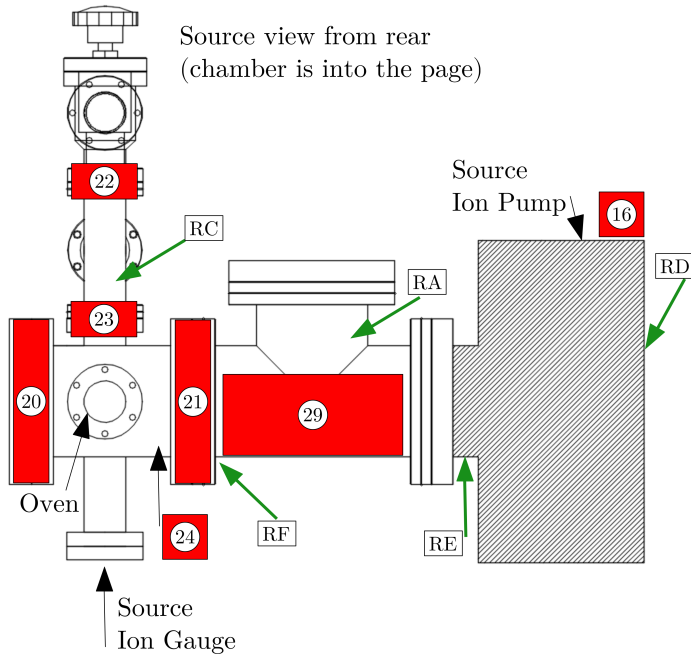


Figure 2.3 : Source assembly - rear view

2D Collimator view from rear  
(source is out of page and chamber is into page)

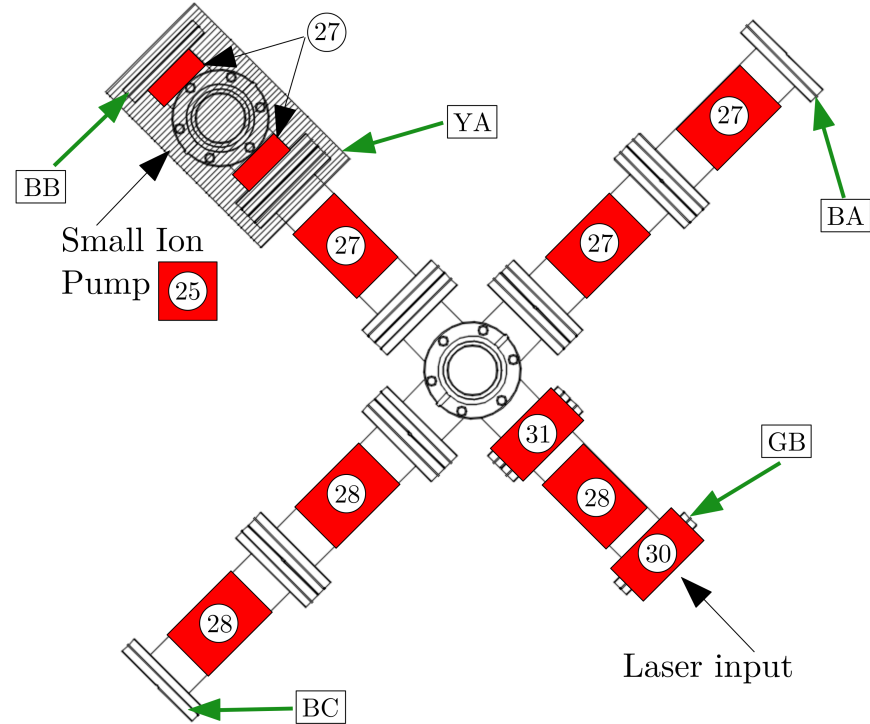
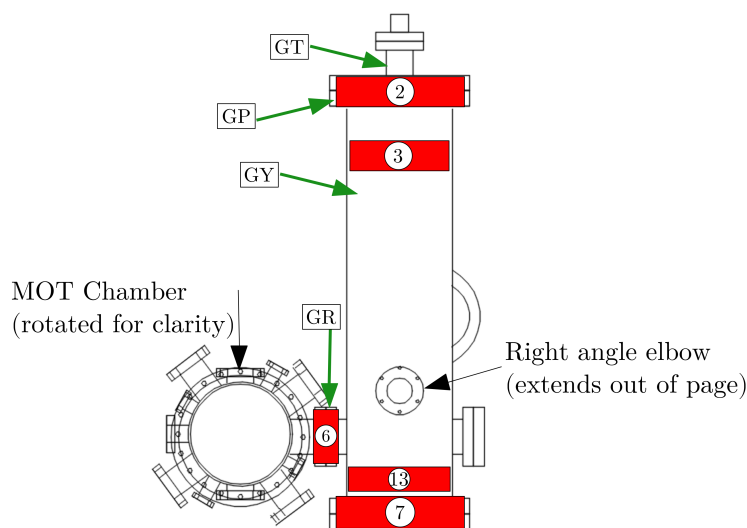


Figure 2.4 : 2D collimator assembly

Right view of tower



Left view of tower

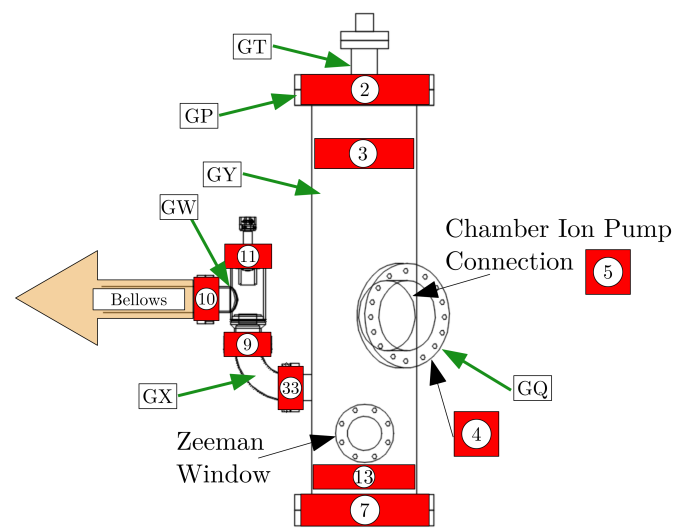


Figure 2.5 : Cryo tower assembly

latter part of this section.

Fig something defines a coordinate system and directional labels used throughout this thesis. We also show the orientation of various lasers through the science chamber to orient the reader. Zeeman beam enters through a certain port in the cryo tower.

Companion figures to those shown in Fig above are also available in Fig something with the positions of heater coils and thermocouples labeled and catalogued which were used for a recent bakeout performed in December 2017. Appendix something covers the process of this bakeout in greater detail.

## Recent changes

### Clarifications from de Escobar thesis

Thesis references two version of the high vacuum tower. The second version is currently in use and was installed around the time the lab moved into it's new location Cryo tower and titanium sublimation cartridge installed. This assembly is referred to as the "second version of HV chamber" in Natali's thesis. This apparatus was

Installation of an improved nozzle design in late 2011. The primary incorporating an array of collimating tubes. Research and modeling of this design

### Ablating strontium off window

Figs Recreate A.49 but with different labels (instead show the laser directions) Create an entire side view of apparatus? Add assembly views of source and cryo tower Nozzle

---

ratus is located at KillianDrobo:\Neutral\Laboratory Systems\Vacuum Chamber\Neutral Chamber\2017.12.26\_strontiumvacuum35\_latticetable.dwg. Additionally, please consult the README file located in this folder for further information.

pictures

Resolve Needle model?

While unchanging during the time of this phd we have learned a number of crucial  
The original drawings of these components can be found in App. A.10 of [? ]  
along with detailed information of the window and ion gauge placements.

Firstly, when moving labs in 2011 a titantium sublimation pump (model?) was installed in the cryo tower which replaced version one of the high vacuum system shown in Fig. A43 of [? ]. Figs blah - blah show an assembled view of the current apparatus with additional views of the cryo tower and source chambers for clarity. Additionally, the original atom oven was upgraded to include capillary tubes constructed from AWG-21 hypodermic needles (model??) to further collimate the atomic beam directly out of the oven [? ]. Fig blah shows a view of the oven currently in the Neutral apparatus and the capillary tubes that were added.

First, the atom source was upgraded to included  $2\mu\text{m}$  capillary tubes model to further collimate the atomic beam out

Description very good resource for design considerations of a similar experiment in Francy's masters chapter 3 Appendix A.10 of Natali's thesis gives specifics about the construction the most notable upgrade to the apparatus since Natali's description was the addition of an extensive second layer surrounding the main chamber. The primary purpose was for shaping the optical dipole and lattice traps but due to its proximity to the chamber, nearly every laser which illuminates the atoms is laucnhed from this platform. Details for the construction of this

Lifetime of atoms once we got vacuum back?

Details of the consturction of the vaccuum system are available in so and so

The goal of this section is to provide an overview of the most recent history of the vacuum system as well as to clarify some of the slightly more ambiguous points about what the construction of the apparatus.

Potentially discuss the concerns we've had about the platform and movement between the chamber and the table. THis can lead to the addition of struts tying the chamber to the platform. This remains a source of concern for heating of the atoms particularly in the optical lattice.

These concerns are exacerbated by an our finding that increased stability came when adding a partial cover over the platform optics for the optical dipole and lattice traps. Although initially meant as a proctective measure, the addition of this cover resulted in a noticeable decrease in shot to shot fluctuations of the cloud position after a time of flight. We found that this stability was a result of mitigating air currents due to the closely located ventilaition system meant to mitigate dust acculation on the optical components.

Drawings for the atom source currently in use on the experiment (as of March 2019) are available in the App [vacuum](#). This oven design is labeled "new nozzle summer 2010", and outlines a heat shield that was ultimately abandoned due to lack of a mechanism to secure it to the base flange. This led to the heat shield falling off when attempting to secure the flange in the apparatus. We hypothesized that lack of a heat shield led to uneven distribution of the thermal energy throughout the oven so we undertook the design of a new oven design to address this issue.

In the late fall of 2017 the neutral apparatus had been under vaccuum for approx 6? years and ater extensive testing we determined that we likely ran out of elemental strontium within the atomic source. This led us to breaking vaccuum, reloading

strontium, and performing a small bakeout procedure to restablish our presssure. ripor to this event we enjoyed lifetimes on the ordr of 25s s measured by background lifetimes measurements within our IR optical dipole trap. Apprximately a year affer this event we have observed lifetimes on the order of approx 15s, the cause of the discrepancy is currently unknown. During the time of breaking vaccuum we decided to attempt everal upgrades to the apparatus such as adding a gate valve between the pumping tower and the zeeman window and redesigning the nozzle source to incorporate a heat shield around the heating element to produce a more even heating environemnt along the nozzle. De to timing we did not install the gate valve before re-establishing vaccuum. The hope in doing this upgrade was to provide a better method for replacing the end cap window which the atom source directly points at. During the course of our experiments this window slowly accumulates a thin layer of strontium which may act as a parital mirror and attenuate the crucially important zeeman beam. As a note of interest, it was shared through private communication with professor Killain that pulsed 532 nm light (such as from a q-locked Verdi system used in the Plasma laboratory) might vaporize the strontium off the window and restore any loss in power. Using a test appartus we were able to verify that indeed we can ablate the strontium off of a coated window, as shown in figure something. This promising test led us to install an optical traversal port, shown in figure, connecting the two labs. Unfortunately, while flashing the verdi on a small section of the neutral experimental window we found that the energy needed to ablate the strontium was accompanied by deformation of the optical surface of the window. We attritbute this to the thicknes of the coating as the key difference between the experiment and the Neutral machine. With that fun aside, we oder an extra window and the gate valve

to replicate the system put in place on the Rydberg apparatus so that future needs to repalce the window coul be accomplished by simply back filling the chamber with dry nitrogen or argon, closing the gate valve and simply replacing it quickly without the need to expose the main chamber body to direct atmospheric gas.

Reudction of the time the window was exposed to hot strontium led us to install a small servo motor driving the valve (model something) and integrate this mechanism into the experimental runtime. This allows the shutter to only be open during the times that we are actively trapping atoms. Details of the servo motor trigger integration into the neuKLEIN control system are available in App somewhere.

The second improvement that we attempted was to redesign the nozzle to include a heat shield. A CAD image is shown in figure. Unfortunately, due to the high tolerances of the base flange and surrounding enclosure the machining required for this custom piece was deemed prohibitvely expensive. A prototype was design following the machine drawings available in App someplace but was abandoned due to a bend that developed in the tubing which holds the fire rod.

However, the largest constraint was due to the flange size of 2 3/8" as the basis for the design. This provides very tight confinement and w

What is the model number for the firerod? What were the materials that were used?

During the course of realignment of having the vaccuum chamber open, we took the opporunity to replace the atom source with an uncoated window to aid alignment of the zeeman beam through the entire length of the vaccuum system. While doig this we learned that there is a slight angle to the differential pumping tube which separates the atom source chamber from 2D collimation chamber. While we were not

able to determine the severity of the misalignment the main symptom of its existence is the partial occlusion and loss of power in the zeeman slowing beam. With an input power of approx. 120 mW before expansion optics and entering the chamber, we measured 60 mW of power transmitted through the window during our testing. Replacement of this differential pumping tube is problematic as it is part of a copper flange held between flanges connecting the aomt source chamber and 2D collimator. This positioning necessitates a drastic and practically infeasible deconstruction of the vaccuum system to replace. Our goal here is simply to inform future students of this issue as we believe it is the primary cause of the much longer load times needed in the Neutral apparatus when compared to the newly designed Rydberg machine.

## 2.3 Laser systems

The heart of any atomic physics experiment is the laser systems which can be utilized for various studies.

Our lab relies heavily upon the use of injection locked lasers [ref](#)

### 2.3.1 Wideband cooling stage: 461 nm

#### 2.3.1.1 Overview

The first stage of laser cooling happens on the 1S0 - 1P1 transition which is separated by approx 461 nm. We generate this light by amplifying and frequency doubling 922 nm light.

Generation of 461 nm Overview isotope shifts Components 922 Master MOT light generation Zeeman light generation Sat Abs Diagram

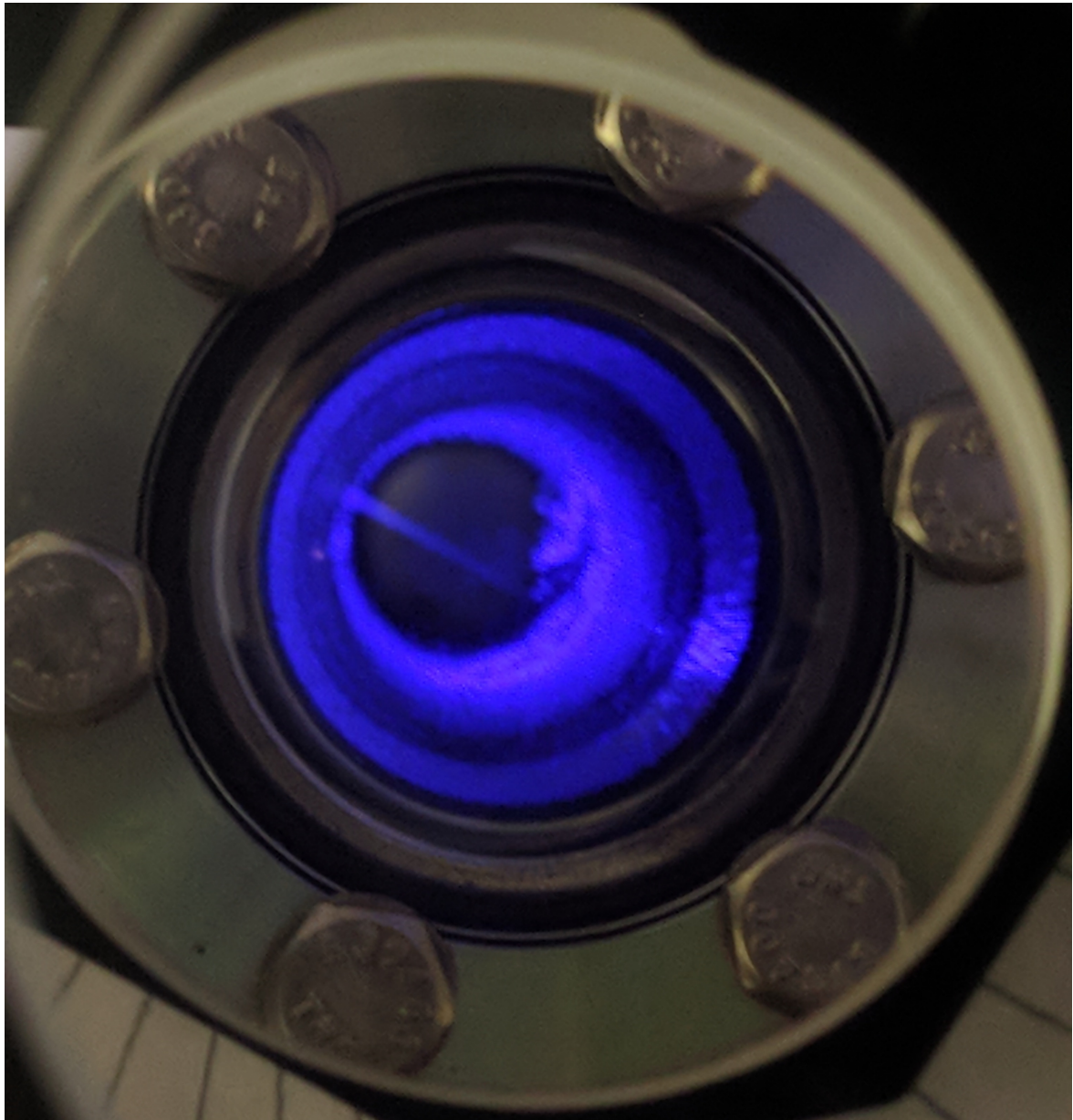


Figure 2.6 : Typical floorescence of Zeeman beam looking down 2D collimator

This view is found using a 2 in mirror aligned along the path of the first pass of the 2D collimator (near mirror 3 in the diagram), looking down the collimator tube. While looking at this angle, we are able to see the Zeeman beam move across the atom column when moving the last turning mirror. Reduction in this fluorescence signal from that shown was the primary indicator of lack of strontium in the source.



Figure 2.7 : Ablating strontium coating from window

Comparison of the before (left) and after (right) when using a pulsed 532 nm Verdi to ablate strontium. The residue visible in the after image was due to a higher energy pulse which was reduced as we moved towards the center of the window.

### 2.3.1.2 922 nm master

The master is a Sacher Lync 922 nm IR diode laser in a Littman Metcalf ECDL configuration. As shown in figure something, the light from this diode is shaped and directed into a fiber optic cable (model?).

Light is coupled into the fiber, then on the output goes through an AOM which detunes the diffracted order by (how much?). The diffracted and zeroth order are then separated with the unshifted beam sent towards the MOT generation subsystem and the shifted light towards the Zeeman subsystem.

The output of the 922 light has sideband directly on it from a high-pass filter coupled directly to the laser diode.

These sidebands are used to lock perform the PDH locking necessary for locking the cavity length. Once 461 nm light has been generated using the MOT subsystem, a small portion is picked off and used to interrogate a saturated absorption cell. Using frequency modulated Doppler-Free saturated absorption we generate an error signal which is used to complete the feedback loop and maintain the frequency position of the complete 461 nm system. Figure outlines this process.

922 master specifics description typical running current and temp feedback characteristics tips of operation beware of changing temp beware of using the sacher voltage control Locking characteristics addition of slow lock reference that Josh will provide code in his thesis note that addition of this slow lock enabled the experiment to stay locked for upwards of 24 hours at a time. As expected, such an increase in stability has greatly improved our ability of taking data. main lock circuit RF source?

### **2.3.1.3 Zeeman subsystem**

Zeeman path Description construction outlined in chapter 2 of AArón's Saenz's masters thesis Components TA Cavity AOMs Shutters

Zeeman TA Description who built Components Mounts Optics Circuits current control board temp control board note the thermistor in use Typical running values in power out power TA current TA temp Tips power drops occasionally, flip on and off alignment can be difficult, try to stabilize in a lower mode History water got on TA so it might be finicky

Cavity Description who built Components Optics Circuits PDH lock Typical running Tips

### 2.3.1.4 MOT subsystem

The MOT path generates light used for a multitude of processes including the first MOT stage, the 2D collimator, the absorption imaging, and the blow away beam, as shown in fig blah.

MOT light path Description Components TA Cavity AOMs Shutters Tips advisable to peak up alignment on a daily basis fairly robust but must keep an eye on as power may fluctuate by as much as 15 percent over the course of a day

MOT TA Description who built Components Mounts Optics Circuits current control board temp control board note the thermistor in use Typical running values in power out power TA current TA temp Tips

Cavity Description who built Components Optics Circuits PDH lock Typical running Tips

### 2.3.1.5 Changing isotopes

The magnetic tunability utilized to control the 461 nm light is well documented in Natali, Pascal, Michael Viray writeup, others? While the basic setup has not changed over the many year, we have recently moved away from the original current source based on a home built high-current FET amplifier to a Bi-polar something model blah. This change allows for more expansive coverage of the 1S0-1P1 isotopes shifts. The previous current source limited our dual trapping capability of 87+88, and required an AOM to be tweaked and the sat. abs. to be realigned for trapping 84 and 86. Using the BOP we can now span the range of 84 and 87 within a single experimental cycle. However, trapping of 88 still requires the realignment procedure. Care should

be taken when adjusting this alignment as the paths are highly coupled as can be seen in Fig [blah](#). Below we outline a straightforward algorithm for adjusting this alignment

1. Change the sat. abs AOM detuning using the potentiometer attached to the sat. abs. VCO.
2. Peak up the AOM alignment

Using the magnetic tunability of the sat abs as outlined in

### **2.3.2 Repumping: 481 nm**

Plot from Rydberg

Discuss the change with the EOM Frequency center of EOM and range?

Data on picking the timescale? I know I choose like 40ms (including delay, but did I take data on this)

### **2.3.3 Narrowband cooling stage: 689 nm**

#### **2.3.3.1 Overview**

Generation of 689 nm Overview Components Toptica Master Boson setup Fermion setup Sat Abs Diagram AOMs

Throughout the course of this PhD, the Neutral 689 nm system has grown significantly and been almost entirely restructured. The master laser system is now shared between the Rydberg and Neutral laboratories and therefore a more modular approach was adopted to ensure independence of the labs experimental schedules.

This process began with the replacement of our homemade Littman-Metcalf ECDL 689 master with a Toptica DL-Pro system. Additionally, at the time of this writing (spring 2019) we are currently in the process of migrating from the original high-finesse cavity used for the last 15 years [? ] of the experiment to an ultra-low expansion cavity system.

Our new approach to sharing the 689 light is based on fixing the lock point of the 689 light and fiberizing this fixed frequency light to the separate experiments. From this master fiber we utilize a series of AOM's to choose the correct frequency needed for the experiment at hand. This movement to a fiber based system culminated in the spring of 2018 when the Neutral apparatus significantly refactored our red system and transitioned to an entirely fiber based injection locking scheme. Optical fibers provide several key advantages when used to injection lock slaves, namely a much TEM00 output mode that can be easily mode-matched to the slave. Additionally, fibers provide a quick and effective means for ensuring optimal alignment of the injection locking light by coupling the rejected light from the slave diode "backwards" through the fiber. Although rejected light is typically minimized when setting up a slave diode, by temporarily placing a waveplate before the isolator you can scramble the input polarization and increase the rejected power to facilitate alignment through the fiber. This process generally results in a quite robust alignment of the fiber output and the laser diode and is much faster than the free space method of coupling over a long distance. This alignment advantage along with improved mode matching has allowed us to injection lock a slave diode with as little as  $300 \mu\text{W}$  while producing up to 24 mW of usable output power.

The rest of this section will detail the setup of the 689 system including the

master system and both boson and fermion subsystems used for narrowline cooling and spectroscopy.

### **2.3.3.2 689 nm Master**

Description Original reference Diagram Components Mounts Riser Optics Fiber mounts and launchers Circuits FALC connections RF setup Systems High finesse cavity Sat. Abs. Gigahertz AOM Typical running characteristics DLC-Pro settings FALC settings Figures of linewidth measurements of noise Profiles Tips for operation History

### **2.3.3.3 Boson subsystem**

Description Diagram Profiles? Components optics isolator cubes lenses mounts custom diode holder aoms RF circuits circuits temp controller current controller Spectrum analyzer reference? refer to the better version developed by Roger Runnign characteristics Example spectrum? MOT path powers

### **2.3.3.4 Fermion subsystem**

Discuss the combination of all the paths using the D mirros and how you have to try and do the best you can with alignment. Typically found it best to align beams to center on the cubes and align to the chamber picking one of the paths. Then when adding additional path be careful to only touch the last two mirrors which independetly affect that path.

## Stir laser

Description Diagram Profiles? Components optics isolator cubes lenses mounts custom diode holder aoms RF circuits circuits temp controller current controller Spectrum analyzer Runnign characteristics Example spectrum? MOT path powers

## Trap laser

Description Diagram Profiles? Components optics isolator cubes lenses mounts custom diode holder aoms RF circuits circuits temp controller current controller Spectrum analyzer Runnign characteristics Example spectrum? MOT path powers

### 2.3.4 Optical dipole trap: 1064 nm

save

Discuss how our only method for evaporative cooling is through light traps since we do not have a magnetically sensitive ground state.

Addres hisotry o laser and say that the current IPG died in fall of last year.

How much power roughly is split between the arms? AOMs are back to back which couples the power stability of the two arms. This setup allows us to more fully utilize the available power from the IPG and in practice while two completely decoupled independent arms may add a slight complication, when accounted for this has generally not been a major source of concern. We have found it useful though to continuously monitor the evaporation trajectory from shot to shot though. As a problem, say with a misbehaving power lock, along one arm may result in intensity fluctuations of both arms.

Several different types of traps have been formed, ref Ying thesis. There are two paths split, named the loading arm and the sheet/dimple arm. Give stats on the loading path. The loading path has the ability to be recycled on itself but we have not utilized this capability in many years due to complications of measuring the trap frequencies.

The sheet/dimple arm can take two configurations as it's name suggests. The sheet trap is an approx. 400 x 40um sheet with the short axis parallel along gravity. This geometry is useful for the low densities needed for Sr 86 to minimize the effects of three body recombination. Alternatively, by switching out a mirror we can direct this power

Formula for ramp

#### **2.3.4.1 Alignment Procedure**

Will focus on independent arm alignment of loading trap and sheet trap

Also useful to imagine three orthogonal axes with their origin set at the center of the chamber.

Need a figure showing the beam prop directions and the setup I'm envisioning.

From the figure, we see that the loading trap propagates primarily along the X-direction. We start by aligning loading trap since it is generally less sensitive and the ports that it goes through are equidistance from the ori

Can generally get away with centering vertically on the chamber windows. goal is to rotate about the center point, can verify this by equalizing the distance from the edge of the window on both sides of the chamber

Letting the atoms extend along a single dimension of the trap.

Moving the red MOT up and down with the z-trim. Dynamic control of z-trim is useful here as you can define a loading b field value then a science b field value.

Use the shortpass dichoric mirrors to counter propagate a red loss beam. Alignment of the red beam follows the usual procedure making sure to reduce the exposure time and power as low as possible while maintaining a loss signal which should maximize alignment.

The sheet trap propagates primarily along the y-axis. This direction has one port extended away from the main chamber body due to the ion gauge. This can complicate the alignment. You

is a little more complicated because it

For peaking up the the sheet trap alignment, hit the red MOT with the loading trap, then extinguish the red MOT away and hold in the single arm loading trap for approx 10-20ms. This allows the red MOT to fall away and the atoms caught in the ODT will expand along the arm, mapping out the spatial profile. Once the untrapped atoms have fallen away, image the the atoms in situ (i.e. without a time-of-flight). With the spatial profile outlined you should be able to scan the sheet trap vertically looking for horizontal confinement along the loading trap. As the sheet is so tight along the vertical direction, this alignment is done using the last cylindrical lens before the chamber.

Dimple trap follows the same process as the sheet alignment but there is a Newport Pico motor for finely adjusting instead of a lens.

### 2.3.4.2 Trap frequency calibration

Measurement of trap frequencies had previously relied upon parametric heating via intensity modulation of the optical dipole trap [cite Ying thesis](#). This process would observe atom loss via resonant heating when the modulation frequency matched a trap oscillation frequency. While this is a convenient and simple process it can lead to quite a complicated spectrum since the heating process does not discriminate directional information and may lead to coupling of higher harmonics of the trap frequencies.

Cover both methods, moving the laser beam itself and snapping back or using the 532 beam to pull.

Primarily have used the kicking method for the measurement of trap frequencies using independent arm ODT (combination of the loading and sheet/dimple trap).

With the recent addition of the high power 532 nm for the optical lattice, we have explored an alternative method of inducing a center-of-mass oscillation. This method uses a single pass of the green light purposely misaligned to the equilibrium position of the ODT to pull the atoms and excite an oscillation.

#### Kicking method

Primarily have used this For the loading trap. Keep the sheet the

Use the RF meter to measure the output frequency (eliminates any offset in voltage readings) Use a dynamic voltage output to load into a trap that is slightly misaligned. Both the

The process for measuring the horizontal is For the current configurations of traps we have found an approx 1 MHz change to the overall RF frequency of 82 (?) MHz

to provide a reasonable amplitude.

Vertical oscillation can be excited by flashing off the sheet trap for 1-2 ms.

Example time dynamics

### **Pulling method**

As alluded to above

we have installed an absolute positioning pico motor mirror mount

#### **2.3.4.3 Modeling the potential**

Need to discuss this

Give formulas and then approx on harmonic potential and methods for estimating the oscillation freq

#### **2.3.5 Optical lattice trap: 532 nm**

Brief theory

profiles

Causes for concern thermal lensing (both optical power and RF power)

Formula for tanh ramp

##### **2.3.5.1 Alignment procedure**

Porto technique Lookup note in onenote

Dropping through arm C

### **2.3.5.2 Lattice depth calibration**

Cover the simple approx and the Gadway method

### **2.3.5.3 Modeling the potential**

Give the simple forms (plane waves) and the more complete formulas

## **2.3.6 Optical toolbox**

### **2.3.6.1 Absorption imaging system**

Description Diagram Components

Give ref to appendix for in-depth technical discussion of image processing

Ref to Mi App A on imaging system

Discuss time of flight pixel calibration as well as the optical magnification system put in place by Mi

Give timing diagram, name the first pulse the atom pulse and the second the background pulse.

Actualy diagram of the imaging system, the light path and the relation of the beam to the chamber

Give reference to section with theory but discuss the technical limitations

Absorption imaging is a destructive measurement process which is predicated on measuring the spatially distributed attenuation of laser light after passing through an atomic cloud. In this section we will discuss the technical details of the Neutral absorption system and reserve the theoretical description of the process to Sec.3.2.1.

We must consider the bit depth of the camera's pixels, which in turn influences

the number of photons (the intensity) we can illuminate the cloud with over a certain time. this must be related to the thinness of the sample right? Thick clouds also mean multiple scatters? Find someone that discusses this idea.

The number of photons needs to be in a certain range, not to little but not too much. perhaps discuss the real world implication of counting photons (changing the exposure time)

This consideration means we generally aim for an optical depth around unity which is an order of magnitude difference the atom and background pulse.

We use such and such camera include datasheet in appendix since it is hard to find which has a double shutter function. More details can be found in the appendix some sec. We care about the timing since the laser intensity and frequency might drift between the atom and background images. Variations in intensity have straightforward implications for errors since the measurement of the atomic number density assumes the only difference between the images is due to the presence of scatters, Sec. some sec, and does not account for fluctuating photon number. Very occasionally, the Neutral apparatus will experience an underexposed shot (of either the atom or background image) that must be discarded due to large, noticeable, fluctuations. We hypothesize that these occurrences are the result of environmental perturbations (acoustic noise, vibrations through the table, spurious ground or electrical noise). However, the precise cause is unknown as the absorption imaging happens very quickly at the end of the experimental cycle when multiple systems begin to reset for the next sequence and in practice, these fluctuations do not occur often enough to be a major cause for concern.

The more insidious source of error in absorption imaging is variation of the optical

frequency. Coherent, frequency stabilized radiation is used to illuminate the atom cloud so that we may control the optical absorption cross section and accurately measure the atomic number density. However, this laser light is passed through many optical components on it's path to the atoms and ultimately the imaging camera. Small reflections along this path result in a multitude of interferometers which causes small scale spatial intensity variation across the beam. Exacerbating this problem are short time frequency drifts that may occur between the atom and background images which result in slightly different fringe patterns in the atom and background images. Fringes patterns are a well known nuisance in experimental AMO images and it has become routine to use linear algebra techniques to create a composite background image for each atom image during analysis [? ]. A brief discussion of the principal component analysis (PCA) algorithm employed by the Neutral analysis routine is outlined below, while a more discussion can be found in Sec. [some sec.](#). Briefly, this approach is as follows:

1. Find a basis set of background images from a large set of raw background images.
2. For a single atom image, construct an initial guess at a composite background image using coefficients to weight each basis image resulting in a superposition of the basis images.
3. Segment the atom image into multiple regions by separating out the region of interest around the atom cloud.
4. Comparing similar regions between the composite background and the atom

background region, perform a least-squares minimization by tweaking the weighting coefficients of the composite background.

5. Once a suitable composite background has been found, calculate the optical depth using the atomic region of interest and the corresponding region of the minimized composite background image.

This procedure is repeated for each atom image using a static background basis set that is periodically recalculated using recent background images to account for long term drifts of the apparatus. This may be numerically intensive as it is done for each atom image but the results have proven remarkable for even modest computational resources.

add picture showing the fringe removal

### **2.3.6.2 Chirped blow away pulser**

Reference Josh's master for construction

Reference Natali's(?) thesis for shelving

Discuss usage in measuring Rabi frequencies (add appendix discussing the fitting of the optical bloch equations?)

### **2.3.6.3 Highly tunable 689 nm spectroscopy system**

Discuss all the ways this guy can be injection locked.

Reference Weixuan's writeup. Did he leave a writeup?

Default boson probe beam Used for general spectroscopy of 3P1, PAS, and rabi oscillations. Discuss various configurations and the frequencies resulting in their usage

Bragg beam inputs and reference to Brian's thesis Figure - outline various light paths for each config Outline the inputs and the outputs for the spectroscopy slave

#### **2.3.6.4 Spin-manipulation laser with dynamic polarization control**

Outline path, discuss LCR, reference Josh's masters

### **2.4 Experimental control and electronics**

Huge amount of electronic needed to run this experiment. Primary method of control is analog voltage control or serial connections.

#### **2.4.1 Computer control and measurement system**

Control Pulseblaster for timing NI cards for voltage control make a table with model number and importnat characteristics discuss limitations that must be watched out for FPGA system

Measurement Pico scope pixelfly wavemeter

#### **2.4.2 Ancillary laboratory systems**

##### **2.4.2.1 MOT coils**

Find reference for circuit

What is the current source

Discuss possible future improvement

##### **2.4.2.2 Trim coils**

Standard trim coil apparatus with the coils in a helmholtz configuration.

Used to trim out static residual B-fields and to apply dynamic and well controlled external magnetic fields.

Should include the trim coils in here somewhere and discuss how to zero the B field as well as provide what the calibration factor is for the coils

Model numbers for Gwinstek drivers on Z and Y. Reference something about the BioChip for the X box and give a model number for its current source.

Beware of the high sensitivity of the 3P1 state to B fields. Small changes in current can affect the position of the MOT. Particularly noticeable when attempting to zero the field as there may be unknown offsets. It is recommended to

#### **2.4.2.3 Zero crossing AC line trigger**

Give circuit diagram and the logic gates needed to correctly trigger both pulseblasters.

Give data showing that the pulseblasters are synced (if I have it)

#### **2.4.2.4 Pneumatic actuated mirror mounts**

Any references?

Diagram Description Components Circuits

## Chapter 3

### Photoassociation in ultracold gases

#### 3.1 Introduction

This part needs to be brief and really should motivate the idea of PAS.

PA is not unique to atomic physics, chemists have been using light to interrogate molecular structure for a long time

physicists molecule

PA can come in many forms (in a lattice, in a bulk gas, via dissociating molecules)

Experimentally we observe PA by looking for trap loss **doublon paper**.

There are multiple flavors of PAS. Can do one-photon or two-photon.

Can even be used to modify the scattering length of atoms through mixing of atomic eigenstates.

Pioneering work done in the early 90's used PA to interrogate the structure of interatomic potentials to deduce the scattering lengths between atoms.

a photoassociation experiment can be used to map the square of the scattering wave function in the ground electronic state at the Condon points corresponding to the different excited bound levels. [11] What about the history of scattering? Most of what we know about quantum mechanics comes from either scattering experiments of spectroscopy. Definitely need some BS about how simple scattering theory has been a hallmark of atomic physics and Photoassociation spectroscopy is an important field

which relies on both of these properties.

Alkaline earth atoms, such as Sr, were hypothesized to take advantage of OFR's since there is a narrow transition easily accessible which could provide large changes in the elastic cross section while minimizing the losses due to the inelastic contribution. This was thought to be possible by controllable detuning the closed channel from the incoming open channel and balancing the loss rate (check this). While there were observations of a strontium OFR, notably work done on this very apparatus (citations), they were accompanied by unexpectedly high loss rates. Recent work by Nicholson et. al. were able to explain some of this behavior through a quantum interference effect whereby the elastic loss rate returns to zero between bound states as the effects of bound states cancel each other out. They used a coupled-channel description to describe the physics.

rabi oscilations between atomic and molecular condensates (cite ours and the lattice experiment that followed)

short-range PA This work is focused on long-range PA but in recent years groups have also developed short-range PA techniques for the creation of rovibrational ground state molecules. These techniques rely heavily on favorable overlap integrals betwwen molecular wavefunctions and typically searching for favorable intermediate states is a pain (that is why our large FCF might be useful)

While the general idea of photoassociation is straightforward, a rigorous theoretical understanding of the process requires discussion of several key topics related to the behavior of ultracold gases. fix this segue The photoassociation process is effected by the residual kinetic energy of the atoms, external potential energy from trapping potentials, and the internal potential energy due to inter-particle scattering between

atoms. In the following sections we will introduce how to determine the spatial and momentum density distributions of bulk atomic gases using a statistical mechanics approach. Next, we'll explore the two-body problem of cold collisions physics which is essential to understanding the photoassociation process. This approach will develop a quantum mechanical model describing interacting atomic particles. Finally, we'll extend this fully quantum theory with the addition of external fields and subsequently apply simplifying assumptions to formulate analytic expressions for modeling photoassociation spectra.

### 3.2 Theoretical description of trapped boson gases

Add equations Itrans from page 51 of natali's thesis

This section will briefly discuss the

Need to know the spatial and momentum distribution of atoms in the trap. Concerned with space as the likelihood of PA is dependent on the interatomic separation and the overlap integral between wavefunctions plays a big role. Highest probability of excitation is near the Condon point [citations?](#)

Momentum distribution needs to be known as this effects how the wavefunction looks as well as the distribution of energies within the cloud which can lead to line-broadening and asymmetric lineshapes

Essentially first part of chapter 2 from Res

We need

Since photoassociation is a two-body process, an accurate description of the spatial

[Ben](#) This chapter will briefly cover the statistical mechanics of trapped atomic

gases, both both at thermal temperatures and at near-zero temperatures for bosons and fermions. In our experiment, we typically acquire data by imaging the atomic density profile either in-situ or after releasing the atoms and allowing them to freely expand for a variable time-of-flight (TOF). I will discuss the expected density profiles for these various regimes and the related fit functions that we use to extract physical information from our samples. To illustrate the properties of trapped atomic gases, let us first consider a system in the grand canonical ensemble. For non-interacting particles at a temperature  $T$ , the average occupation of the state  $i$  with energy  $E_i$  is

**James** Typically our samples have a fixed number of particles,  $N$ , so the chemical potential,  $\mu$ , is constrained such that

In the limit of large particle number we can describe the gas semi-classically assuming that the occupation of the ground state is negligible.

The semi-classical distribution is defined such that the average number of particles in the phase-space volume  $d\mathbf{p}d\mathbf{r}$  is given by  $f(\mathbf{r}, \mathbf{p})d\mathbf{p}d\mathbf{r}/(2\pi)^3$  and

check the equation numbers in pethick and smith Consider the number density of atoms per phase space volume  $(2\pi\hbar)^3$  integrated from  $\epsilon > 0$

$$n(\mathbf{r}) = \int \frac{d\mathbf{p}}{2\pi\hbar^3} \frac{1}{\exp((E_r(\mathbf{r}) - \mu/k_B T) - 1)} \quad (3.1)$$

where we are neglecting the full quantum nature of the atoms and considering them as point masses with free particle energy  $E_r(\mathbf{r}) = \frac{p^2}{2m} + V(\mathbf{r})$

next we define the quantities

$$x = \frac{p^2}{2mk_B T} z(\mathbf{r}) = e^{\mu - V(\mathbf{r})/k_B T} \quad (3.2)$$

define  $\xi$

then performing a change of variables and plugging into above eq we find

$$n(\mathbf{r}) = \frac{2}{\sqrt{\pi} \lambda_T^3} \int dx \frac{\sqrt{x}}{z^{-1} e^x - 1} \quad (3.3)$$

where  $\lambda_T = \sqrt{\frac{2\pi\hbar^2}{mk_B T}}$  is the de Broglie wavelength cite?. This integral is of a certain form and can be rewritten using cite Demarco pg 237 footnote

need to put bound on these integrals from 0 to inf where does the 3/2 come from?

$$\begin{aligned} \int_0^\infty dx \frac{x^{\gamma-1}}{z^{-1} e^x - 1} &= \sum_{n=1}^{\infty} \int_0^\infty dx x^{\gamma-1} e^{-nx} z^n \\ &= \Gamma(\gamma) \text{Li}_\gamma[z] \end{aligned} \quad (3.4)$$

where  $\text{Li}_\gamma[z]$  is the polylogarithm function defined by cite something

$$\text{Li}_\gamma[z] = \sum_{n=1}^{\infty} \frac{z^n}{n^\gamma} \quad (3.5)$$

This function is also known as the bose enhancement function cite ketterle and describes the bunching of bosonic particles near degeneracy

Using this identity we can write the thermal distribution as

$$\begin{aligned} n(\mathbf{r}) &= \frac{\text{Li}_{\frac{3}{2}}[z(\mathbf{r})]}{\lambda_T^3} \\ &= \frac{1}{\lambda_T^3} \text{Li}_{\frac{3}{2}}[\exp(\mu - V(\mathbf{r})/k_B T)] \end{aligned} \quad (3.6)$$

For harmonic traps  $V(\mathbf{r}) = \frac{m}{2} \sum_i \omega_i^2 r_i^2$  where  $r_i$  represents the Cartesian coordinates. Plugging this into previous eq then the *in-situ* density profile is given by

$$n(\mathbf{r}) = \frac{1}{\lambda_T^3} \text{Li}_{\frac{3}{2}} \left[ \xi \exp \left( \sum_i \frac{-m\omega_i^2 r_i^2}{2k_B T} \right) \right] \quad (3.7)$$

Argue what  $z$  is what is it's range?, then say that it is small when  $T$  is large. Therefore, writing the first few terms of the series expansion of Eq.3.5

$$\text{Li}_\gamma[z] = z + \frac{z^2}{2^\gamma} + \frac{z^3}{3^\gamma} + \dots \quad (3.8)$$

we see that  $\text{Li}_\gamma[z] \approx z$  for  $z \ll 1$ . This corresponds to the high temperature limit which should result in recovery of the MB solution and indeed it does. In the classical, or high-temperature, limit  $\text{Li}_{\frac{3}{2}}[z(\mathbf{r})] \approx z(\mathbf{r})$ . From Eq. we see that this that in the limiting case we get the expected Maxwell-Boltzmann density profile what happens with  $\xi$ . In the following we will continue to use the full expressions with an explicit dependence on the polylogarithm as it is the most general form, however, we will use this approximation to ensure our expressions match those expected from a classical Maxwell-Boltzmann description of the gas.

this can be simplified

$$n(\mathbf{r}) = \frac{\xi}{\lambda_T^3} \exp \left( \sum_i \frac{-m\omega_i^2 r_i^2}{2k_B T} \right) \quad (3.9)$$

I'd like to put in something about the momentum distribution

MI PA [33] is a phenomenon in which two colliding atoms absorb a photon to create a bound, electronically excited molecule. Figure 1.1 shows the PA process of Sr: the bottom one is the  $1S0+1S0$  ground state potential, the long-range part of which is described by the R-6 van de Waals term, and the top one is the excited molecular  $1S0+3P1$  potential whose interaction at large separation is given by the R-3 dipole term. Two free ultracold Sr atoms in the ground state  $1S0$  with the thermal collision energy of  $E_g$  approach each other, and absorb a photon with the energy of  $h\nu$  to photoassociate to a molecular bound state of the excited potential around the Condon point  $R_c$ . The bound state  $\psi_e$  has the binding energy of  $E_b$ , and the Condon point  $R_c$  is the interatomic separation where PA occurs most likely which is characterized by the Franck-Condon overlap integral discussed later. The formation of the molecule is followed by spontaneous or stimulated decays, usually

creating either two free atoms with high kinetic energy or ground state molecule, both of which usually are lost due to extra high energies. Detecting the loss of atoms is a typical method to perform PA. According to the conventional treatment [33, 34], the strength of the PA transition is proportional to the Franck-Condon overlap integral between wave functions of ground-collisional and excited bound state. Since the wave functions oscillate fast at the short interatomic separation, the Franck-Condon overlap integral is dominated by the amplitude of the ground-state wave function near the Condon point  $R_c$  [33]. It is noticed that in  $^{88}\text{Sr}$  the Franck-Condon overlap between the second least bound state on the  $1\text{S}0+3\text{P}1$  potential and the ground-collisional state is large, which is a crucial feature to the applicability of experiments discussed in this thesis. PA has proven to be a very powerful tool in ultracold physics, such as determining absolute binding energies, extracting atomic collisions information, modifying collision strength, and making ultracold molecules [33].

### **3.2.1 Extracting data from column densities**

This description of the atoms in the trapping potential is useful but we need to go a step further because we use absorption imaging to determine properties of the atom after a time of flight.

Maybe put in something about different measurement techniques and reference the ketterle and pethick and smith again.

Removing the trap results in ballistic expansion with the above spatial density profile as the initial conditions. To derive how we find the properties of the atoms, consider the above spatial density profile as the initial conditions.

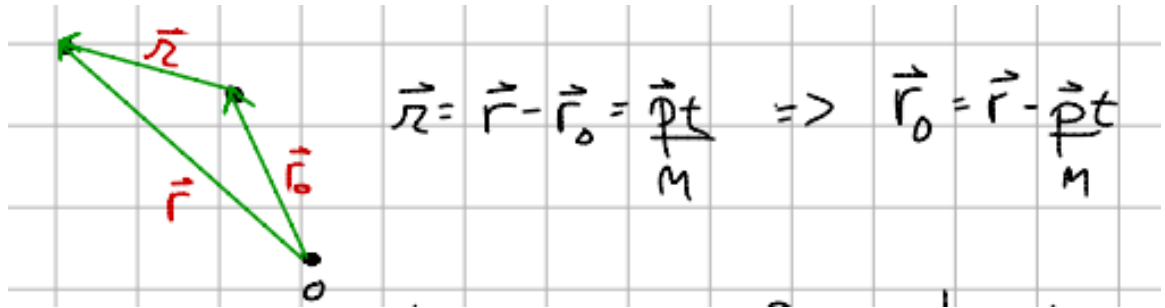


Figure 3.1 : Ballistic expansion of particles

Schematic representation particle displacement vectors used to determine how time-of-flight expansion transforms the initial density distribution

Atoms expand ballistically according to

$$\frac{d\mathbf{r}}{dt} = \frac{\mathbf{p}}{m} \text{ and } \frac{d\mathbf{p}}{dt} = 0 \quad (3.10)$$

Thus, an atom measured at position  $\mathbf{r}$  after the time-of-flight,  $t$ , will have moved a distance  $\zeta = \frac{\mathbf{p}t}{m} = \mathbf{r} - \mathbf{r}_0$  from its initial position  $\mathbf{r}_0$

make the tof density  $n'$  the spatial density evolves then double check  $2\pi\hbar$  denom

$$\begin{aligned} n(\mathbf{r}, t) &= \int \frac{d^3\mathbf{r} d^3\mathbf{p}}{(2\pi\hbar)^3} \frac{1}{\exp\left(\left[\frac{p^2}{2m} + V(\mathbf{r}') - \mu\right] \frac{1}{k_B T}\right) - 1} \delta^3\left(\mathbf{r} - \frac{\mathbf{p}t}{m} - \mathbf{r}'\right) \\ &= \int \frac{d^3\mathbf{p}}{(2\pi\hbar)^3} \frac{1}{\exp\left(\left[\frac{p^2}{2m} + V\left(\mathbf{r} - \frac{\mathbf{p}t}{m}\right) - \mu\right] \frac{1}{k_B T}\right) - 1} \end{aligned} \quad (3.11)$$

Plugging in the harmonic potential we find that free expansion after release from a harmonic trap is self-similar and amounts to rescaling the the spatial coordinates by check Demarco's thesis. Thus the scaled spatial profile is given by

$$n'_{th}(\mathbf{r}, t) = \frac{1}{\lambda_T^3} \left( \prod_{j=1}^3 \frac{1}{1 + \omega_j^2 t^2} \right) \text{Li}_{\frac{3}{2}} \left[ \xi \exp \left( \sum_{i=1}^3 \frac{-m\omega_i^2 r_i^2}{2k_B T} \frac{1}{1 + \omega_i^2 t^2} \right) \right] \quad (3.12)$$

Using this description of the spatial distribution after time-of-flight expansion, we must now consider how to relate our absorption measurement to the physically relevant variables of the gas.

Finally we must consider the column density along one direction since we are taking absorption images of the atoms. A brief description of absorption imaging and system used for this process is given in some sec.

Simply stated, absorption imaging is the process of illuminating a gas of atoms with resonant (or near resonant) laser light and taking a spatially resolved image of the laser beam. As the light is tuned near a resonant transition, the atoms will absorb and scatter photons out of the original laser beam resulting in a "shadow" which is proportional to the number of scatters within a certain spatial region. This shadow image is then normalized by taking another picture of the laser after the atoms have fallen out of the imaging region. This relation of the light attenuation to the number density of scattering particles is known as Beer's law and results

Using Beer's law cite, we can relate the total absorption of photons to the number density of scattering particles along the optical path multiplied by the absorption cross section. This results in a measurement of the "optical depth" of the gas along a column density. Measurement along a particular direction limits our description of the gas to the two-dimensional plane orthogonal to the laser beam as shown in some fig from ch 2.

Experimentally, the optical depth is trivially computed by taking the natural logarithm of the ratio of the images obtained from the camera. We then equate this OD image to be proportional to the spatial density profile after the time-of-flight

expansion integrated along the optical path through the atoms.

$$\begin{aligned} \text{OD} &= \ln \left( \frac{\text{Atom Image}}{\text{Background Image}} \right) = \sigma_{abs} \int_{-\infty}^{\infty} dz n'_{th}(\mathbf{r}, t) \\ &= \frac{\sigma_{abs}}{\lambda_T^3} \left( \prod_{j=1}^3 \frac{1}{1 + \omega_i^2 t^2} \right) \int_{-\infty}^{\infty} dz \text{Li}_{\frac{3}{2}} \left[ \xi \exp \left( \sum_{i=1}^3 \frac{-r_i^2}{2\sigma_i^2} \right) \right] \end{aligned} \quad (3.13)$$

where  $\sigma_i^2 = \frac{k_B T}{m \omega_i^2} (1 + \omega_i^2 t^2)$ . Need to say something about the integral in Eq.[prev](#) and evaluating the integral along  $z$  so going to write out the explicit spatial dependence in cartesian coordinates. Additionally, we'll rewrite the polylogarithm in terms of it's series representation in order to see an identity

$$\int_{-\infty}^{\infty} dz \text{Li}_{\frac{3}{2}} \left[ \xi \exp \left( \sum_{i=1}^3 \frac{-r_i^2}{2\sigma_i^2} \right) \right] = \int_{-\infty}^{\infty} dz \sum_{n=1}^{\infty} \frac{\xi^n}{n^{3/2}} \exp \left( \frac{-x^2}{2\sigma_x^2} - \frac{y^2}{2\sigma_y^2} - \frac{z^2}{2\sigma_z^2} \right)^n \quad (3.14)$$

Defining  $\rho = \exp \left( \frac{-x^2}{2\sigma_x^2} - \frac{y^2}{2\sigma_y^2} \right)$  and expanding the series out, Eq.[above](#) becomes

$$= \int_{-\infty}^{\infty} dz \xi \rho \exp \left( \frac{-z^2}{2\sigma_z^2} \right) + \frac{\xi^2}{2^{3/2}} \rho^2 \exp \left( \frac{-z^2}{2\sigma_z^2} \right)^2 + \frac{\xi^3}{3^{3/2}} \rho^3 \exp \left( \frac{-z^2}{2\sigma_z^2} \right)^3 + \dots \quad (3.15)$$

In this form we can readily separate out the dependence on  $z$  and perform the integral making use of the following identity [check identity](#)  $\int_{-\infty}^{\infty} dz \sum_{n=1}^{\infty} \exp \left( \frac{-z^2}{2\sigma_z^2} \right) = \frac{\sqrt{2\pi}}{n^{1/2}} \sigma_z$ . Eq.[above](#) then reduces to

$$\begin{aligned} &= \int_{-\infty}^{\infty} dz \sum_{n=1}^{\infty} \frac{\xi^2 \rho^n}{n^{3/2}} \exp \left( \frac{-z^2}{2\sigma_z^2} \right) \\ &= \sqrt{2\pi} \sigma_z \underbrace{\sum_{n=1}^{\infty} \frac{\xi^n \rho^n}{n^2}}_{\text{Li}_2[\xi \rho]} \end{aligned} \quad (3.16)$$

We are now ready to plug this result for the integral back into the full expression for the optical depth. Retaining the explicit expression in cartesian coordinates,

Eq.[above](#) becomes

$$OD(x, y) = \frac{\sqrt{2\pi}}{\lambda_T^3} \frac{\sigma_{abs}\sigma_z}{(1 + \omega_x^2 t^2)(1 + \omega_y^2 t^2)(1 + \omega_z^2 t^2)} \text{Li}_2 \left[ \xi \exp \left( \frac{-x^2}{2\sigma_x^2} - \frac{y^2}{2\sigma_y^2} \right) \right] \quad (3.17)$$

This equation still has one unknown,  $\sigma_z$ , that we cannot readily measure. This problem is solved by recognizing that we can readily calculate and measure a specific value of Eq.[something](#), namely the peak optical depth ( $OD_{peak}$ ) located at  $x = 0, y = 0$ .

$$OD_{peak} = \frac{\sqrt{2\pi}}{\lambda_T^3} \frac{\sigma_{abs}\sigma_z}{(1 + \omega_x^2 t^2)(1 + \omega_y^2 t^2)(1 + \omega_z^2 t^2)} \text{Li}_2[\xi] \quad (3.18)$$

thus the relation between the measured optical depth and the spatial density distribution is given by

$$OD(x, y) = \frac{OD_{peak}}{\text{Li}_2[\xi]} \text{Li}_2 \left[ \xi \exp \left( \frac{-x^2}{2\sigma_x^2} - \frac{y^2}{2\sigma_y^2} \right) \right] \quad (3.19)$$

and in the limit of long expansion time during time-of-flight, namely  $t \gg \omega_x^{-1}, \omega_y^{-1}, \omega_z^{-1}$  then the measured widths reduce to  $\sigma_i^2 = \frac{k_B T}{m} t^2$  and the atom temperature is given along each axis by

$$T_i = \frac{m\sigma_i^2}{k_B t^2} \quad (3.20)$$

Regarding the assumption that the expansion time is much greater than the trap frequencies, we should note that limiting factors in the expansion time are due to center of mass motion of the cloud under the influence of gravity. In the Neutral apparatus we typically utilize drop times are  $\approx 30$  ms. For shallow traps, where  $\omega_i$  is small, then the atoms may not have enough time during expansion to achieve fully ballistic expansion. In these cases it is typical to quote temperatures of the sample as measured along the tightest axis of confinement.

Last thing to do is to relate our expression for optical depth and number density to the total number of atoms in the trap. This task is straightforward by recalling the boson normalization requirement

$$\begin{aligned} N &= \int_{-\infty}^{\infty} d^3\mathbf{r} n_t h(\mathbf{r}) = \int_{-\infty}^{\infty} d^3\mathbf{r} n_t h'(\mathbf{r}, t) \\ &= \int_{-\infty}^{\infty} d^3\mathbf{r} \frac{\sigma_{abs}}{\lambda_T^3} \frac{1}{(1 + \omega_x^2 t^2)(1 + \omega_y^2 t^2)(1 + \omega_z^2 t^2)} \sum_{n=1}^{\infty} \frac{\xi^n}{n^{3/2}} \exp\left(\frac{-x^2}{2\sigma_x^2} - \frac{y^2}{2\sigma_y^2} - \frac{z^2}{2\sigma_z^2}\right)^n \end{aligned} \quad (3.21)$$

This equation is the same problem we saw above but integrated over all axes instead of just one. Therefore we can apply the same expansion and identity we employed to solve for the optical depth to find

$$N = \frac{(2\pi)^{3/2}}{\lambda_T^3} \frac{\sigma_x \sigma_y \sigma_z}{(1 + \omega_x^2 t^2)(1 + \omega_y^2 t^2)(1 + \omega_z^2 t^2)} \text{Li}_3[\xi] \quad (3.22)$$

From our expression for the optical depth, Eq.**some**, we can simplify this to

$$N = \frac{2\pi \sigma_x \sigma_y}{\sigma_{abs}} \text{OD}_{\text{peak}} \frac{\text{Li}_3[\xi]}{\text{Li}_2[\xi]} \quad (3.23)$$

Eq.**above**

All of our information comes from taking pictures of our atomic clouds and inferring the physical properties of the gas before the time-of-flight expansion. This is possible since we know the density profile of the gas in-situ. In the absence of external fields, other than gravity, turning off the trapping potential results in ballistic expansion described by  $\mathbf{r} = \mathbf{r}_0 + \frac{p^2}{2m}t$ , where  $\mathbf{r}_0$  and  $p$  are the position and momentum at the moment of release from the trap and  $t$  is the expansion time. Neglecting the center-of-mass motion due to gravity and assuming long expansion times, then we can easily find a regime where  $\frac{p^2}{2m}t \gg \mathbf{r}_0$  and therefore

$$\mathbf{r} \approx \frac{p^2}{2m}t \quad (3.24)$$

This

[? ] get demarco thesis?. Thus, for atoms

Thus, for atoms starting at a position  $\mathbf{r}_0$

Density profile expands self-similarly

Time of flight is essentially a Fourier transform which turns the initial momentum information into spatial information.

### 3.3 Characterizing collisions

understand how to treat quantum two-body problem with external field coupling

Collisions are one of the key ways we learn things about atoms

In atomic physics, our low density gases are mainly within the regime of small interactions.

Here is where I cite sources of some of the original PA work, feshbach stuff collisions as an interferometer of the incoming and outgoing off the barrier, but also of different partial waves.

I want the reader to know that PA dis concerning the scattering wavefunction, that it comes from the overlap integral of the two wavefunctions (why do I need to know this? because this means that it is sensitive to positions of the nodes and can be used to map out the potentials. [this will motivate discussing low energy physics](#)

This spatial dependence is mapped onto the internal energy levels of each atom.

I want to say dressed state model here (review atom-photon coupling, atomic physics book).

### 3.3.1 Classical

cross sections as a measure of the time between collisions

potentials where they come from centrifugal barrier analog - slide 16 Julianne just  
r xp of particles

center of mass coordinates only care about relative (generally) simplifies calculations

### 3.3.2 Single channel scattering

quantum solve time0independent SE just need potential, basis set, and boundary conditions

structureless pasrticles scattering free space plane waves de Broglie wavelength strontium de Broglie at 1uK

delta function unitarity limit supports one bound state - the true halo state where the wavefunction comes from

r-dependent potential show 1.1 from Hutson gneerally very complicated between atoms long-range part is typically has a power law drop off important that  $V_{-} \propto R^{-\zeta}$  as  $R \rightarrow \infty$  for ground state atoms dominant long-range part is  $R^6$

scattering states ( $E < 0$ ) repulsive barrier - particle scatter attrative well - particles accelerate

bound states boundary conditions dictate might have quasibound states (shape resonances)

wavefunctions General appraoch is incoming plane wave plus spherical wave common appraoch to expansion of wavefunction in partial wave expansion redefine

SE in terms of partial waves Asymtotic solution from WKB  $V \sim 0$  so must go to plane wave See phase shift

total cross section as sum over all partial waves

this results in a potential that supports bound states.

consider the two particle system as a single entangled particle long range part of this quasi-particle is just the eigenstates of the separate particles themselves (only composed of two parts) but the short range part is going to be determined by some complex physics (new eigenstates, what is the coupling mechanism?) the vdW point is the boundary distance? coupling is due to the interatomic potential, there is at least the long-range part falling off as  $R^{-6}$ , what are the types of interactions which make up the internal wall?

### 3.3.2.1 Low energy results

Simple form for scattering length gives limits on cross sections slide 24 (not sure I get the upper bound bit)

scattering length is a phase accumulation scattering length is very sensitive to details of potential can't really calculate ab initio

a number that represent all the complex physics within the interaction region

simple interpretation as peak shift at long range slide 12 julienne

Another way of seeing the origin of  $a$  is as the collisional  $E$  goes to zero wavefunction should go to a straight line plot from bertlett  $a$  is the intercept of that line on the internuclear axis this is one of the methods of actually determining  $a$

the scattering length as a coupling parameter in length units The mean field energy (I think I had a reference on this) slide 26

Determining  $a$  is not so easy because the interatomic potential is not known this was one of the pioneering uses for photoassociation PA is sensitive to the collisional wavefunction and therefore can help to map out the spatial distribution of the ground state Simple WKB estimation predicts zero-energy bound state as  $E \approx 0$  every atom would have infinite scattering length at low energy obviously not the case, GF first to determine analytic corrections due to long-range vdW interaction comes about because of phase contribution from the long-range part This is the regime we explored with our work in chapter 4 probing a bound state just near the dissociation threshold makes us extremely sensitive to the entire phase of the well

free atoms scattering as single particle state (different eigenstate) interaction determined by some gnarly stuff From scattering theory we know that the long range behavior is determined by short range physics how do we know this? (the dalibard intro) Can we come up with good enough pseudo potentials to describe the short range physics and then solve the schrodinger equation to extract wavefunctions? we want wavefunctions because that is the full characterization we don't know the right eigenbasis for the short range part but we can make some guesses (in particular Hund cases setup eigen states for various possible internal states) Bohn and Julianne theory guessed based on using quantum defect theory this pre-supposes that the bound and free wavefunctions are similar (I forgot in what respect) but that the bound ones must go to zero as  $R \rightarrow \infty$  If we have some notion of the wf then we can construct matrices which define interactions once we add additional coupling to the scattering problem now in a position where I need to connect scattering theory and the PAS

Once we have the ground state wavefunction of our new particle we can construct the internal structure by considering the internal energy structure of the constituent

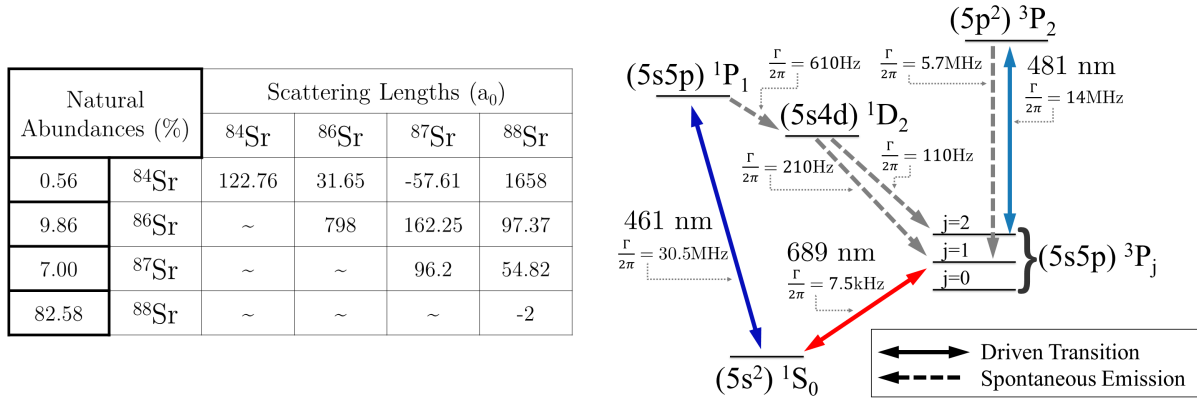


Figure 3.2 : Strontium interatomic wavefunctions

Res 6.3

atoms Can I make a connection that since it is a composite particle we must consider all the various configurations available?

### 3.3.3 Multichannel scattering

Everything we discussed was for unstructured particles this is the power of the scattering length

this would be the end of the story if all of these potentials were "separable" (or independent) you'd find your configuration, describe the potential, solve it, and you're done of course this isn't actually the case because the eigenstates of the separate potentials couple to one another. Even understanding the natural coupling between coupling between potentials is not easy tie back to complexity of understanding short range physics We don't really know what coupling exist and which energy levels are most important mostly effects the bound states of the system strontium example of the D state coupling in the 3P1 potential references to Res and other work

address somewhere that these types of problems are generally solved via coupled-channel methods which follow the same recipe for the scattering problem as in the single channel case but does so considering all channels simultaneously through matrices defining potentials and their couplings to one another. coupled equations are complicated point out references from Julienne, Mies, Bao, Hutson

But can match at asymptotic wavefunction again and get a lot of insight  
example: multichannel use to describe atom-diatom coupling multi-channel model  
(normal MFR diagram) other potentials are due to different combinations of atoms  
in hyperfine states these potentials can have different magnetic moments means that  
addition of a magnetic field can tune them relative to one another MFR has been  
extensively studied and is a common tool used in atomic physics

scattering resonances are due to off diagonal coupling between bound closed channels and scattering open channels give picture hand wavy explanation is that bringing a bound state close will modify the open channel (potential?) this results in a tweak of the phase shift which results in a change in scattering length can describe this as a change in the elastic cross section of the incoming open channel in general there is also an inelastic cross section that may contribute if the bound state has a finite lifetime.

define open and close channels  
S matrix - defines scattering phases and amplitudes due to couplings between various open and closed channels S found from the asymptotic solutions

if single channel then S reproduces above results if inelastic then get complex scattering length (need better way to segue, Julienne 2014 slide 19 - unitarity argument maybe) complex scat Real part is the elastic cross section Imag part if the inelastic

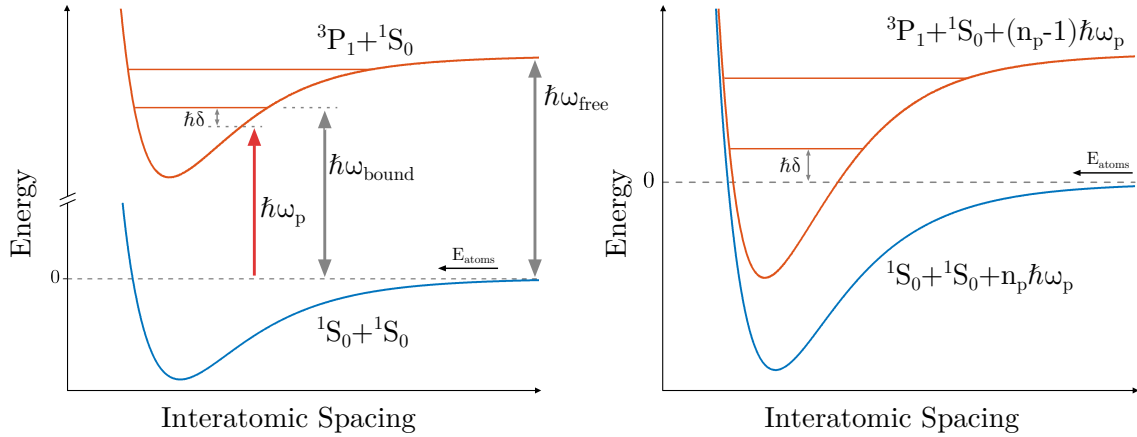


Figure 3.3 : Schematic representation of a Feshbach resonance

(a) Potentials for the open ( $^1S_0 + ^1S_0$ ) and closed ( $^3P_1 + ^1S_0$ ) channel of an optically coupled Feshbach resonance in strontium. (b) The same coupling shown in (a) in the dressed state model. Tuning of the excited potential is achieved by varying the laser frequency detuning,  $\delta = \omega_p - \omega_{bound}$ , and  $\omega_{free}$  is the  $^1S_0 \rightarrow ^3P_1$  atomic transition frequency.

Also the Chin '10 review on feshbach resonances

Follow the Nicholson 15 paper method of introing the elastic and inelastic cross sections

The use of a laser field as the coupling scheme in a Feshbach resonance introduces several advantages and complexities that must be considered when determining the expected properties of optical Feshbach molecules. In order to understand these differences, we will briefly outline the key concepts behind Feshbach resonances and the distinctions between optical and magnetic Feshbach resonances.

The basic idea of a Feshbach resonance is outlined in Fig. 3.3.3. Consider a simple

two channel system, denoted by the open channel and the closed channel. The open channel is generally a ground state potential for two free atoms near threshold. Atoms occupying this state can undergo elastic collisions and, in the absence of any external perturbation, will remain in the open channel. Conversely, the closed channel is a bound state of a higher lying potential who's energy can be tuned relative to the open channel. In the absence of coupling between the states, the open and closed channel remain eigenstates of the system as the tuning parameter, and therefore the energy of the closed channel, is changed. However, in the presence of coupling between the channels, the original eigenstates are mixed and develop an avoided crossing between the bare open and closed channels, when tuned across the resonance. The power of Feshbach resonances comes from the ability to externally manipulate the degree of state mixing, which results in control of the s-wave scattering length and the creation of low energy Feshbach molecules.

Magnetic Feshbach resonances (MFR) are used extensively in alkali metal systems to tune the scattering properties of ultracold gases since the ground states of these systems feature a magnetic moment due to an unpaired electron in the valence shell. Thus, MFRs utilize interactions between low lying ground state molecular potentials via spin-dependent couplings. Since both the open and closed channel are ground state potentials, MFRs often exhibit extraordinarily long lifetimes [16, 37]. Conversely, in strontium the ground state is a  ${}^1S_0$  state, as shown in Fig. 1.3. This state is not magnetically sensitive, so no MFRs exist near the  ${}^1S_0+{}^1S_0$  interatomic potential. Fortunately, optical Feshbach resonances (OFR) serve as another method to introduce coupling between the ground state potential (open channel) and a molecular state of an electronically excited potential (closed channel). Our work has utilized coupling

between the  ${}^1S_0 + {}^1S_0$  and  ${}^3P_1 + {}^1S_0$  two-body potentials via the narrow  ${}^1S_0 \rightarrow {}^3P_1$  atomic transition at 689nm. Fig. 3.3.3 shows a schematic of the potentials involved in the OFR of strontium in both the bare atomic and dressed state pictures. In the dressed basis we consider the combined atom + photon field system such that the channels become  $|{}^1S_0 + {}^1S_0 + n_p \hbar \omega_p\rangle$  as the open channel and  $|{}^3P_1 + {}^1S_0 + (n_p - 1) \hbar \omega_p\rangle$  for the closed channel. As the light field frequency,  $\omega_p$ , is varied the excited closed channel potential will experience an energy shift relative to the open channel, resulting in resonant coupling between the open and closed channels. [19, 9? ]

Both MFRs and OFRs can be treated by the same theoretical formalism, as a modification of the collisional properties between two particles [51, 16]. One of the hallmarks of ultracold physics is the simplicity of atomic collisions. As bosonic atoms get colder they can only collide via  $\ell = 0$  partial waves and thus the elastic collision rate between two atoms becomes energy independent and can be parameterized by a single fixed quantity,  $a_s$ . This parameter is known as the s-wave scattering length and is determined by the short range molecular potential between two colliding atoms. Through a similar approach, collisions near Feshbach resonances can be modeled by introducing a complex s-wave scattering length,  $\tilde{\alpha}$ . In this model, the magnitude of  $\tilde{\alpha}$  influences the elastic scattering rate between particles while the imaginary part describes losses through inelastic scattering. Under an isolated Feshbach resonance model at low energies, this complex scattering length is given by [16]

$$\tilde{\alpha} = a - ib = \frac{a_s \Gamma_0}{-E_0 + i(\gamma/2)} \quad (3.25)$$

where  $E_0$  and  $\Gamma_0$  are the energy independent parameters for, respectively, the resonance position and coupling strength between channels, and  $\gamma$  is a general decay

term associated with loss from the closed channel. Using Eq. 3.25, we can note the two main differences between MFRs and OFRs. Most experimentally useful MFRs, such as in Li and K, have negligible closed channel decay,  $\gamma = 0$ , and a fixed coupling strength between the open and closed channels. Thus, the change in the s-wave scattering length takes on a particularly simple form,

$$\tilde{\alpha} = a_s \left( 1 - \frac{\Delta}{B - B_0} \right) \quad (3.26)$$

where  $B_0$  is the resonance position and the coupling strength is parameterized by a magnetic width  $\Delta$ , such that  $\Gamma_0 = \delta\mu\Delta$  with  $\delta\mu$  the difference in magnetic moments between the open and closed channel.

Conversely, OFRs offer the possibility to tune the coupling strength between the open and closed channel, since the coupling depends on the transition matrix element which varies with the square root of laser intensity. Furthermore, since OFRs utilize electronically excited states which have a natural lifetime,  $\gamma$  is nonzero. This results in inelastic loss processes for OFRs. Similar to MFRs, we can define the change in scattering length as [51, 70, 8]

$$\tilde{\alpha} = a_s \left( 1 - \frac{w\delta}{\delta^2 + \gamma^2/4} + \frac{i}{2} \frac{w\gamma}{\delta^2 + \gamma^2/4} \right) \quad (3.27)$$

where  $\delta = \omega - \omega_0$  is the detuning from the chosen photoassociation resonance at  $\omega_0$  as shown in Fig. 3.3.3, and the width of the resonance is defined by  $w = -\ell_{opt}\gamma/a_s$ . Typically, the strength of OFRs are characterized by their optical length [51, 16] given by  $\ell_{opt} = a_s\Gamma_0/\gamma = \frac{\lambda_{OFR}^3 |\langle n|E\rangle|^2}{16\pi c k} I$ . Here  $c$  is the speed of light,  $\lambda_{OFR}$  is the wavelength of the coupling laser, and  $|\langle n|E\rangle|^2$  is the free-bound Frank-Condon factor between the bound state  $|n\rangle$  and scattering state  $|E\rangle$ . Additionally, it is useful to identify the

real and imaginary parts of Eq. 3.27 as defined in Eq. 3.25.

$$a_{OFR} = a_s + \ell_{opt}\gamma \frac{\delta}{\delta^2 + \gamma^2/4} \quad b_{OFR} = \frac{\ell_{opt}}{2} \frac{\gamma^2}{\delta^2 + \gamma^2/4} \quad (3.28)$$

Our previous work exploring the use of an optical Feshbach resonance took advantage of photoassociation transitions with large optical lengths to control the scattering length of an  $^{88}\text{Sr}$  BEC as described by Eq. 3.27. However, all studies of OFR to date have been limited by large atom loss rates [63, 65, 24, 8, 70] which can be modeled as a density evolution,  $\dot{n} = -K_{in}n^2$ , where  $K_{in}$  is the two-body inelastic loss rate constant. In the low energy limit,  $k \rightarrow 0$ , the inelastic loss rate is given by

$$K_{in} = \frac{8\pi\hbar}{\mu_r} b_{OFR} = \frac{4\pi\hbar}{\mu_r} \frac{\ell_{opt}\gamma^2}{\delta^2 + \gamma^2/4} \quad (3.29)$$

where  $\mu_r$  is the reduced mass,  $\delta$  is the laser detuning as shown in Fig. 3.3.3.

### 3.4 Modeling of photoassociation lineshapes

This section will concern the general theory used to describe photoassociative spectra. While a full quantum close-coupling calculation is the most complete and rigorous method for analyzing cold quantum scattering problems, useful approximations can be applied to realize relatively more "simple" closed analytic formulas describing photoassociation spectra.

This section will cover the theory of lineshapes in PAS.

Somewhere I read about three regimes of PAS as a comparison of relevant energy scales. Should explore that here

Pretty much have everything needed from our previous section. Relation of rate constant to cross sections is nice and simple Julianne 14 - slide 21 These fully coupled-channel models are not straightforward to evaluate. Can make assumption to simplify

### 3.4.1 One-photon excitation of free to bound transitions

Can recreate the type of model for MFR in a field dressed approach plot showing photon + potential

ANalytic forms for modeling compare all the forms of K the crazy one from BJ 99 the simple one with  $f(p)$  nicholson 42

show plot with all the terms defined

give loss rate (will need to have introduced before) define terms gammaStim as overlap gamma as molecular lifetime delta as detuning A as coupling strength

introduce reflection approximation evaluation of overlap reference BJ 99

give relative momentum distribution this results in an asymmetric profile give plot

Number equation vs. time

segue to narrow lines

#### 3.4.1.1 PAS near narrow intercombination transitions

quick note on the usage of the relative momentum distribution usually this is all we care about since the CoM part results in doppler shifts which would be negligible on the energy scales of broad dipole-allowed transitions using narrow intercombinations lines, the photon recoil energy is comparable to the bound state lifetime this means that individual lorentzians might be shifted (each by a different amount) in addition to the total line shape being asymmetric Integration over both degrees of freedom will be an important discussion in the next chapter as we fit spectra and determine the halo binding energy

ideas of limiting cases that can be explored with PAS [20]

### 3.4.2 Extension to two-color spectra

Pretty much the same things

Show new picture with all the couplings defined

Now that we have the theory of PAS covered.

$$N(t) = \frac{N_0 e^{-\Gamma t}}{1 + \frac{2N_0 \langle K \rangle V_2}{\Gamma V_1^2} (1 - e^{-\Gamma t})} \quad (3.30)$$

where  $N_0$  is the number at the beginning of the PAS interaction time, and  $\langle K \rangle$  indicates a spatial average of collision event rate constant  $K$  (Eq. 3.32). The one-body loss rate,  $\Gamma$ , is due to background collisions and off-resonant scattering from the PA lasers.

PA loss is described with a local equation for the evolution of the atomic density [Eq. (4.1)]. Integrating Eq. (4.1) over the trap volume yields the time evolution of the number of trapped atoms [Eq. (4.2)]. The effective volumes used throughout this analysis are defined by

$$V_q = \int_V d^3r e^{-\frac{qU(\mathbf{r})}{k_B T}}, \quad (3.31)$$

for trapping potential  $U(\mathbf{r})$ . The collision event rate constant can be expressed as a thermal average of the scattering probability for loss,  $|S(\epsilon, \omega_1, \omega_2, \dots, \mathbf{r})|^2$ , over the collision energy  $\epsilon$ . We also average over the trap volume to allow for the possibility that the scattering probability can vary with position in the trap due to inhomogeneity of laser intensity profiles and the density distribution [Eq. (3.32)].

$$\begin{aligned}\langle K \rangle &= \frac{1}{V_2} \int_V d^3r e^{-\frac{2U(r)}{k_B T}} \\ &\times \frac{1}{h Q_T} \int_0^{U_{max}-U(r)} d\epsilon |S|^2 e^{-\epsilon/k_B T}.\end{aligned}\quad (3.32)$$

where the partition function is  $Q_T = \left(\frac{2\pi k_B T \mu}{h^2}\right)^{3/2}$  for reduced mass  $\mu$ .

Bohn and Julienne [? ] provide an expression for  $|S(\epsilon, \omega_1, \omega_2, \dots)|^2$  for a collision on the open channel of two ground state atoms (g) with total energy  $\epsilon$  leading to loss-producing decay from the excited state  $b_1$  with rate  $\gamma_1$ . (See Fig. 4.1.) It yields

$$|S|^2 = \frac{(\Delta_2 + \epsilon/\hbar)^2 \gamma_1 \gamma_s}{\left[(\Delta_1 + \epsilon/\hbar)(\Delta_2 + \epsilon/\hbar) - \frac{\Omega_{12}^2}{4}\right]^2 + \left[\frac{\gamma_1 + \gamma_s}{2}\right]^2 (\Delta_2 + \epsilon/\hbar)^2}, \quad (3.33)$$

where all quantities are defined in the main text. For simplicity, we have omitted the light shift of  $b_1$  due to coupling to the scattering continuum [? ]. Equation (3.33) neglects all light shifts due to the trapping laser. Light shifts due to the photoassociation lasers coupling to states outside our model (Fig. 4.1) are also neglected. The thermal energy is much greater than the zero-point energy for trap motion,  $T \gg h\nu_{\text{trap}}/k_B$ , so confinement effects are negligible [? ].

and lights shifts of states 0 and 2 are approximately equal and will cancel in the determination of the binding energy of the halo state,  $E_2$  [? 53]. Neglecting

For the experiments reported here, we maintain significant intermediate-state detuning,  $|\Delta_1| \gg |\Omega_{12}|$ . Thus we are in a Raman configuration, and near two-photon resonance the expression for the scattering probability for a given initial scattering

energy Eq. (3.33) can be approximated as a Lorentzian

$$|S|^2 \approx \frac{A(\epsilon)}{\left(\Delta_2 + \epsilon/\hbar - \frac{\Omega_{12}^2}{4(\Delta_1 + \epsilon/\hbar)}\right)^2 + [\Gamma_L(\epsilon)/2]^2}, \quad (3.34)$$

where  $A$  and  $\Gamma_L$  are defined in Eqs. (4.8) and (4.9).

As discussed in the text, we analyze loss spectra using the effective expression, Eq. (4.10) to account for possible deviations from the single-channel theory [? ].

The total 689-nm intensity oscillates with 100% contrast according to  $I_{total} = I_1 + I_2 + 2\sqrt{I_1 I_2} \cos[(\omega_1 - \omega_2)t] = 2I \{1 + \cos[(\omega_1 - \omega_2)t]\}$ . Equation 4.16 The form of the AC Stark shift due to excitation lasers in Eq. 4.11 reflects the time average of the intensity and neglects the interference term. To confirm that this is the correct description, we numerically solved the time-evolution for a three-level system with similar optical couplings and oscillating optical intensity as present during halo photoassociation. The Hamiltonian is

$$H = \quad (3.35)$$

$$\begin{pmatrix} 0 & \Omega_{01} [\cos(\omega_1 t) + \cos(\omega_2 t)] & 0 \\ \cdot & E_{b1} & \Omega_{12} [\cos(\omega_1 t) + \cos(\omega_2 t)] \\ \cdot & \cdot & E_{b2} \end{pmatrix}$$

For  $\Omega_{01} \ll \Omega_{12} \ll \Delta_1 \equiv E_{b1}/\hbar - \omega_1$ , which is analogous to the experimental conditions used here

, the shift of the two-photon resonance condition follows  $\delta = \Omega_{12}^2/2\Delta_1$  in agreement with Eq. 4.16.

## Chapter 4

### Binding energy of the $^{86}\text{Sr}_2$ halo molecule

Here we study the least-bound vibrational level of the  $\text{X}^1\Sigma_g^+$  electronic ground state of the  $^{86}\text{Sr}_2$  dimer (Fig. 4.1), which is a naturally occurring halo molecule, meaning it exists in the absence of tuning with a magnetic Feshbach resonance. A well-known example of a naturally occurring halo molecule is the  $^4\text{He}_2$  dimer [42, 57, 38]. The least-bound vibrational level of the ground state of  $^{40}\text{Ca}_2$ , which was recently studied using similar methods [52], is also very close to this regime.

#### 4.1 Probing the ground state potential

Strontium is a nice atom to work with because of the various properties of all of its isotopes but access to such a variety of properties also comes with its share of complications. The most abundant isotope, 88, has a nearly vanishing scattering length but served as the workhorse for many of our previous studies and those of other labs. The known scattering properties of strontium are mass scaled from 88 is this somehow not as good for 86? Also, where are the most up to date scattering lengths for Sr from? - The '10 Fourier paper but by probing the 86 ground state potential directly we can obtain a more accurate measurement of the 86-86 scattering length.

Additionally, by utilizing the narrow intercombination potential we are able to

detune many linewidths from the intermediate state, thereby

### Two-photon photoassociation

As described in previous chapters, two-photon PAS can be used to directly populate low-lying molecular levels. Applying this technique to strontium 86 we can explore a similar regime

conclusion of chapter 4 is that we measured the binding energy more accurately which can be directly related to a more precious value of the scattering length for 86. Also there is a straightforward experiment available to use to attempt to measure the efimov paramter for strontium.

how did we determine the binding energy? how did we measure spectra?

Weakly bound ground-state dimers are of great interest in ultracold atomic and molecular physics. In the extreme case of a scattering resonance, the least-bound state represents an example of a quantum halo system [33] with spatial extent well into the classically forbidden region. Halo molecules show universality, meaning that molecular properties such as size and binding energy can be parameterized by a single quantity, the *s*-wave scattering length  $a$ , independent of other details of the atom-pair interaction [38, 12]. For potentials that asymptote to a van-der-Waals form, an additional parameter, the van der Waals length  $l_{\text{vdW}}$ , can be introduced for a more accurate description. Efimov trimers also exist in systems near a scattering resonance, influencing dimer and atomic scattering properties and introducing additional universal phenomena [13, 50]. Ultracold halo molecules are often associated with magnetic Feshbach resonances [? ], for which the scattering state and a bound molecular state can be brought near resonance by tuning a magnetic field.

There are important differences between halo molecules associated with magnetic

Feshbach resonances and the naturally occurring halo molecule in  $^{86}\text{Sr}$ . With magnetic Feshbach resonances, the relevant scattering and bound molecular states lie on different molecular potentials, and single-photon magnetic-dipole transitions can be used to measure molecular binding energies with RF or microwave spectroscopy [? 17? ]. Typically, this is done by first forming molecules through magneto-association and then driving bound-free or bound-bound transitions converting the halo molecule into a different state. Other methods include spectroscopy with an oscillating magnetic field [? ], a modulated optically controlled Feshbach resonance [21], and Ramsey-type measurements of atom-molecule oscillation frequencies [22]. It is also possible to efficiently populate halo states with a magnetic-field sweep [29] or evaporative cooling [34] near a magnetic Feshbach resonance [? ]. These are powerful techniques for manipulating quantum gases of alkali metals and other open-shell atoms, for which there are many magnetic Feshbach resonances. Strontium, however, due to its closed-shell electronic structure, lacks magnetic Feshbach resonances in the electronic ground state.

In this work, we probe the halo state in  $^{86}\text{Sr}$  using two-photon Raman photoassociation (PA) [? ], in which two laser fields couple colliding atoms to the least-bound state of the ground molecular potential. We tune near resonance with an intermediate state that is bound in the  $0_u$  potential corresponding to the  $^1S_0 + ^3P_1$  asymptote at long range [? ] (Fig. 4.1). We accurately determine the  $^{86}\text{Sr}_2$  binding energy, considering possible collisional frequency shifts and AC Stark shifts due to trapping and excitation lasers. Using the universal prediction for the binding energy, including corrections derived for a van der Waals potential [30, 26, 27], we derive a more accurate value of the *s*-wave scattering length for  $^{86}\text{Sr}$  atomic collisions [58? ].

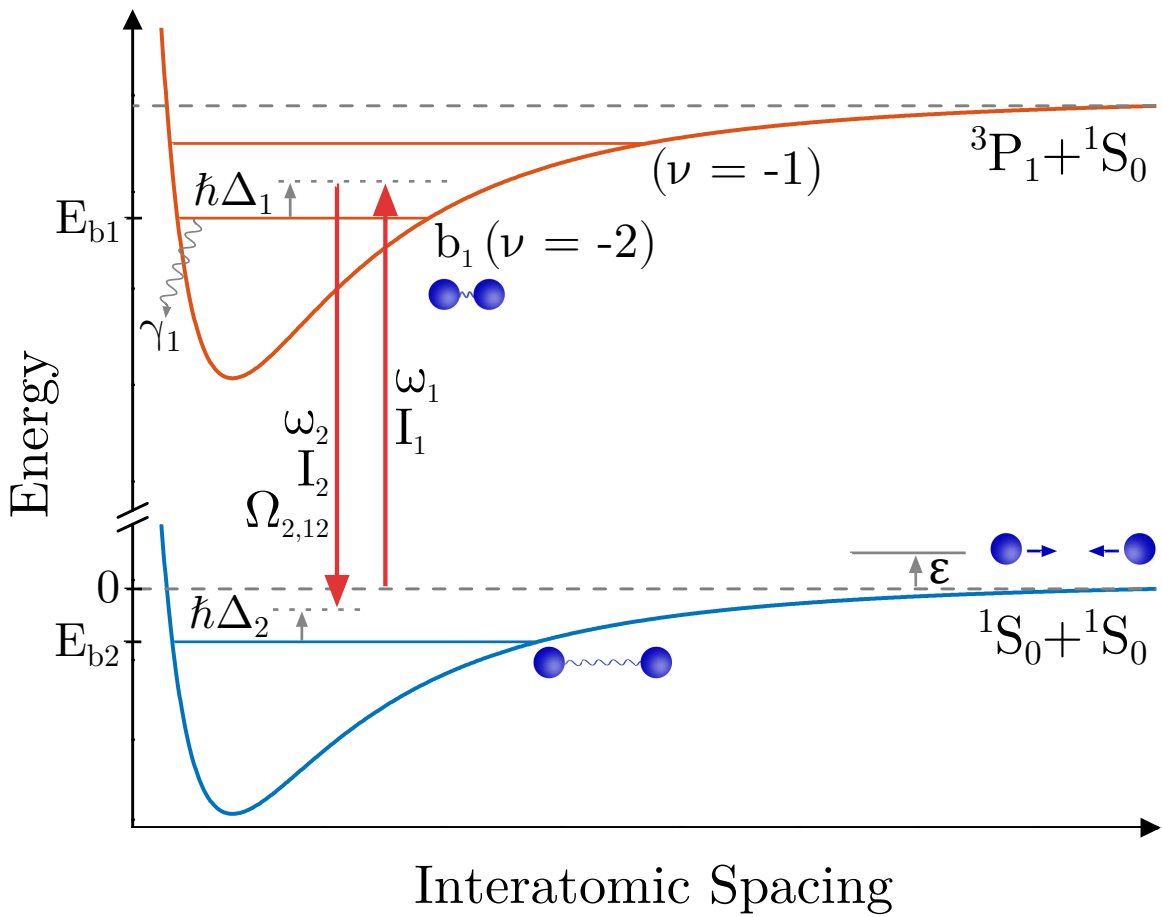


Figure 4.1 : Strontium PAS potential

Two-photon photoassociation diagram . The energy of two well-separated  ${}^1S_0$  atoms at rest is taken as zero.  $\epsilon$  is the kinetic energy of the colliding atom pair.  $E_{b1}$  is the unperturbed energy of the bound state of the excited molecular potential that is near resonance with the free-bound laser, which in these experiments is the second-least bound level of the excited molecular potential ( $\nu = -2$ ).  $E_{b2} (< 0)$  is the unperturbed energy of the least bound state of the ground molecular potential. The photon of energy  $\hbar\omega_1$  is detuned from  $E_{b1}$  by  $\hbar\Delta_1$  for  $\epsilon = 0$ , while the two-photon detuning from  $E_{b2}$  is  $\hbar\Delta_2$ . The decay rate of  $b_1$  is  $\gamma_1$ . Stark and collisional frequency shifts are neglected in this schematic.

## 4.2 Experimental setup

Experimental methods experiments in this chapter and the following are very similar. The biggest scientific difference is that we explored different regimes of intensity. Experiments in this chapter were done on rydberg apparatus nearly identical machine to ours sample prep is the same but they have different ODT configurations. Specifics of general trapping procedure and characteristics can be found in some location used the PA light from my apparatus coupled through a long fiber path generation talked about below. For the low E experiment the general parameters were such and such generic time-invariant diagram (denote where physics is different) generation of photoassociation light. Specifics of the low E experiment discuss optical setup propagation, polarization, B field? ODT configuration consideration of the trap depth during experiment we took a lot of data over a wide range of parameters and assumed we were in a deeply trapped regime. Took data all the way down at 30nK and thought it was normal to not have a BEC at this point because it is 86 determined trap frequencies after we did the experiment during analysis we found a problem with the model not agreeing. 30nK data did not fit well if we made the typical assumptions about a deep trap show plot of fit decided to model the trap numerically trap frequencies were measured at higher temps and extrapolated using model (reason to believe modeling) modeling found that the lowest point of the trap was an odd trajectory and was much lower than we naively thought show plot of fit hypothesized that the sample may not have been thermalized completely (non-ergodic) and thus was fooling us this is supported by the better fitting of 30 nK data over time Brings into questions the use of temperature, but will persist with that data where there is at least reasonable agreement Leads to a

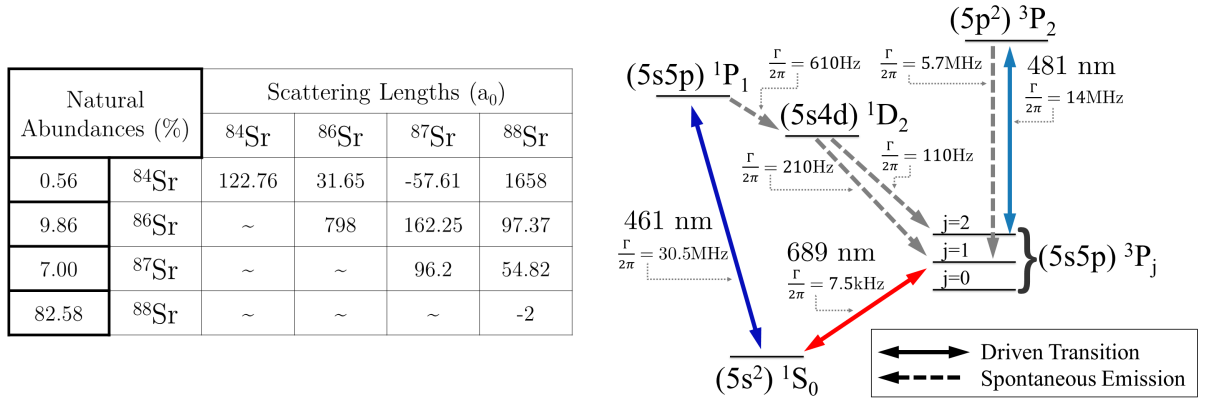


Figure 4.2 : Strontium two-photon photoassociation

fig 1 from the halo paper

strong modification of the momentum distribution and will effect the energy integral due to large variation in the available energy range

In this work, we probe the halo state in  $^{86}\text{Sr}$  using two-photon Raman photoassociation (PA) cite 16 from halo paper, in which two laser fields couple colliding atoms to the least-bound state of the ground molecular potential. We tune near resonance with an intermediate state that is bound in the 0u potential corresponding to the  $^1S_0 + ^3P_1$  asymptote at long range as shown in Fig.4.2.

Photoassociation experiments follow the same general presciption. We start by trapping through the normal sequence as outlined in some section. Then we evaporate down to the final trap depth. After evaporation

The two-photon PAS experiments described in the following chapters are performed under similar conditions but due to complications with the neutral vaccuum system we performed the binding energy experiemtns using the Rydberg apparatus. While non-ideal from a consistency point of view, this did allow us to replicate and

validate our previous findings which gives us great confidence in the robustness of this experimental approach.

The most significant difference between the two apparatus' is the trapping characteristics of the optical dipole traps and the beam parameters of the photoassociation beam. These differences are noted in the corresponding chapters but here we will outline the timing and generic characteristics that are shared between the two experiments.

Table [something](#) shows the relevant experimental parameters and typical values for our photoassociation experiments.

Specific details of the optical dipole traps, PA beam parameters, and using a completely different a

performed on ultracold Sr atoms in a single-beam optical dipole trap (ODT) generated from a 1064-nm laser propagating perpendicular to gravity. Typical atom numbers are several hundred thousand and peak densities are  $\approx n_0 = 1 \times 10^{12} \text{ cm}^{-3}$ . The number of atoms and sample temperature are measured using time-of-flight absorption imaging described in [some section](#). Trap oscillation frequencies are determined by measuring dipole and breathing collective mode frequencies, which allow determination of trap volume and sample density

For experiments done on our apparatus we generate the two photon source as shown in Fig $\text{??}$ . Light comes from an injection locked slave diode which follows the frequency stabilized 689 master laser described in [some section](#). This light is modulated via a single acousto-optic modulator (AOM) driven with two frequencies and coupled into a single-mode polarization maintaining optical fiber. This fiber output is launched near the science chamber and the light output level is continuously

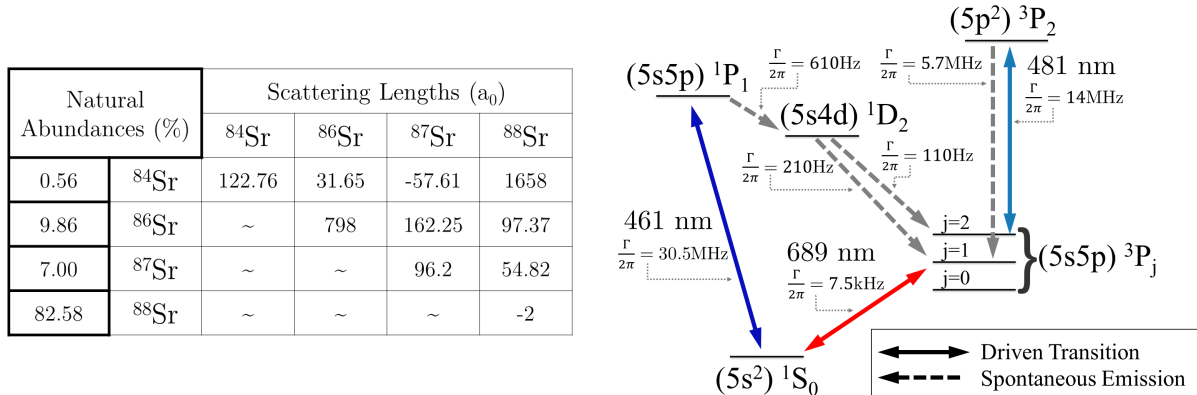


Figure 4.3 : Schematic of PAS light generation

Properties of strontium. Left: Natural abundances and s-wave scattering lengths for all mixtures of Sr. Right: Simplified energy level diagram of Sr showing the relevant states used for trapping and cooling of the atomic gas

monitored via a beam sampler and photodiode placed between the fiber output and the chamber.

Primary reasons why we can't scan large distances. There will be a slight misalignment of the beams into the fiber and the RF may start to fall off. For these experiments an AOM with a center frequency of 90 MHz was used.

This simple system has many advantages and a couple of drawbacks. Since both photons are aligned into the same fiber then they are guaranteed to have the same output wavevector and therefore the two photon process will be doppler free (since the absorption and emission processes will exactly cancel each other out).

This is a simple system for generating multiple frequencies which are guaranteed to share the same wavevector, phase coherence, and gross frequency stability. Use of the AOM provides highly accurate control of the difference frequency with RF

precision.

While versatile and simple, we are worried about the balance of the RF power onto the AOM. These devices are narrowband modulators (simple ones)

We see a reduction in contrast when the two drive frequencies differ by more than  $\approx 250$  kHz.

Since the modulator is a narrowband device, scan great care is taken to ensure the maximum amount of contrast is visible on the photodiode. This

As described in some section the slave laser is frequency stabilized at +42 MHz of the 86Sr  $^1S_0 \rightarrow ^3P_1$  atomic transition. The AOM then shifts the light the remaining  $\approx 86$  MHz to set the detuning around the  $\nu = -2$  bound state of the  $^1S_0 + ^3P_1$  potential. Setting of  $\Delta_1$  is done by removing one of the frequencies, peaking up the diffraction angle and alignment into the fiber.

During the course of our experiments we found that mild environmental perturbations (loud noises, air currents due to fans, etc.) to the fiber resulted in slow variation of the light coupling through the fiber. Such amplitude modulations are not uncommon in laser systems and can typically be compensated for by using a closed loop locking mechanism. However, after construction of such a power lock the components did not react quickly enough and there was a significant overshoot which resulted in an uncontrolled amount of light illuminating the atoms during short exposures. This led us to implement a digital based sample and hold mechanism for reduced intensity variability. This system is described in detail in some section. The sample and hold system in combination with the power lock provided intensity stability with a standard 5% standard deviation during a typical experiment. Fig shows a typical

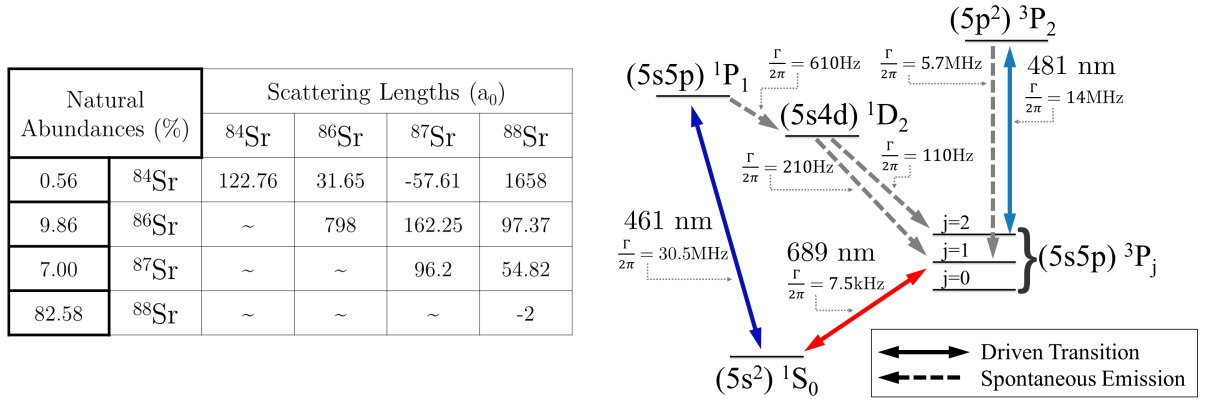


Figure 4.4 : Histogram of PAS beam intensity variation

One of the histograms from onenote. There are separate histograms for each experimental run (I should combine this so I don't have to discuss)

histogram of the recorded intensities.

Make sure to discuss how I scanned the rf frequencies since there is a difference to increasing the freq difference. Since we used the -1 order of the AOM, increasing the frequency of the drive relative to the gross actually lowered the amount of energy in the system, resulting in effectively scanning  $\Delta_1$  instead of keeping it fixed. This resulted in a slight variation of the AC stark shift from the intermediate state that can be seen in the strong coupling experiments that are discussed in some section.

The beat signal of the two light fields after the fiber is monitored on a photodiode and the rf powers are adjusted to ensure matched intensities for the two frequency components ( $I_1 = I_2 \equiv I$ ).

Regarding the general process

Using the  $^1S_0 + ^3P_1$  interatomic potential, we perform a raman process using the  $\nu = -2$  bound state which has a binding energy of  $E_b = -44 \text{ MHz}$  cite improved

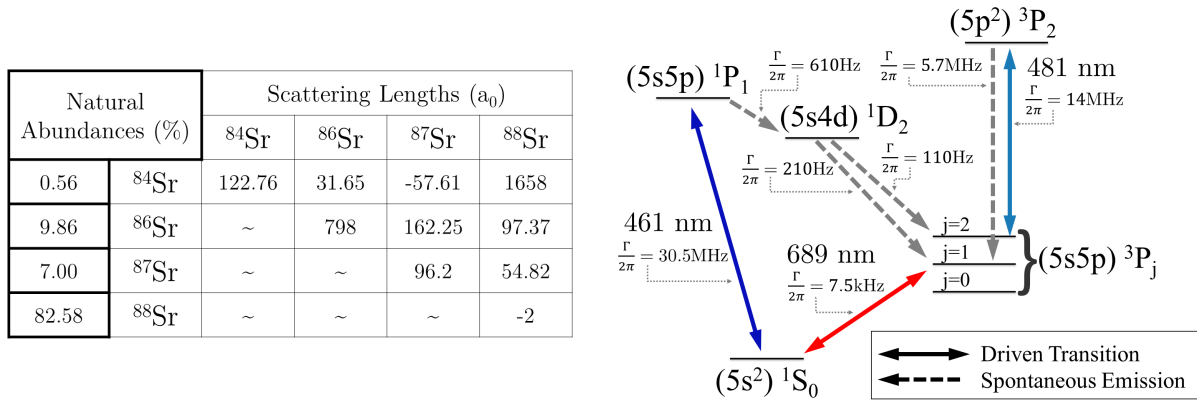


Figure 4.5 : Characteristic view of the PA beatnote

This is the picoscope plot of the beatnote

binding en. Sample pre

We used strontium 86 in a thermal gas at temperatures between 30 and 1000 nK.

Typical peak densities were around  $n_0 = 1 \times 10^{12} \text{ cm}^{-3}$ .

Raman process using the second bound state of the  $^1S_0 + ^3P_1$  interatomic potential

What atom do we use what is the sample conditions what trap do we use what are the dimensions of the trap what are the trap freq how do we determine

Two-photon spectroscopy is performed on ultracold  $^{86}\text{Sr}$  atoms in a single-beam optical dipole trap (ODT) generated from a 1064-nm laser propagating perpendicular to gravity with beam waists of  $260 \mu\text{m}$  and  $26 \mu\text{m}$  [? ? ]. The tight waist provides vertical confinement. The trap depth after an evaporative cooling stage determines the sample temperature, which is set between 30 – 1000 nK. Typical atom numbers are several hundred thousand and peak densities are as high as  $2 \times 10^{12} \text{ cm}^{-3}$ . The number of atoms and sample temperature are measured using time-of-flight absorption imaging operating on the  $^1S_0 - ^1P_1$  transition. Trap oscillation frequencies are

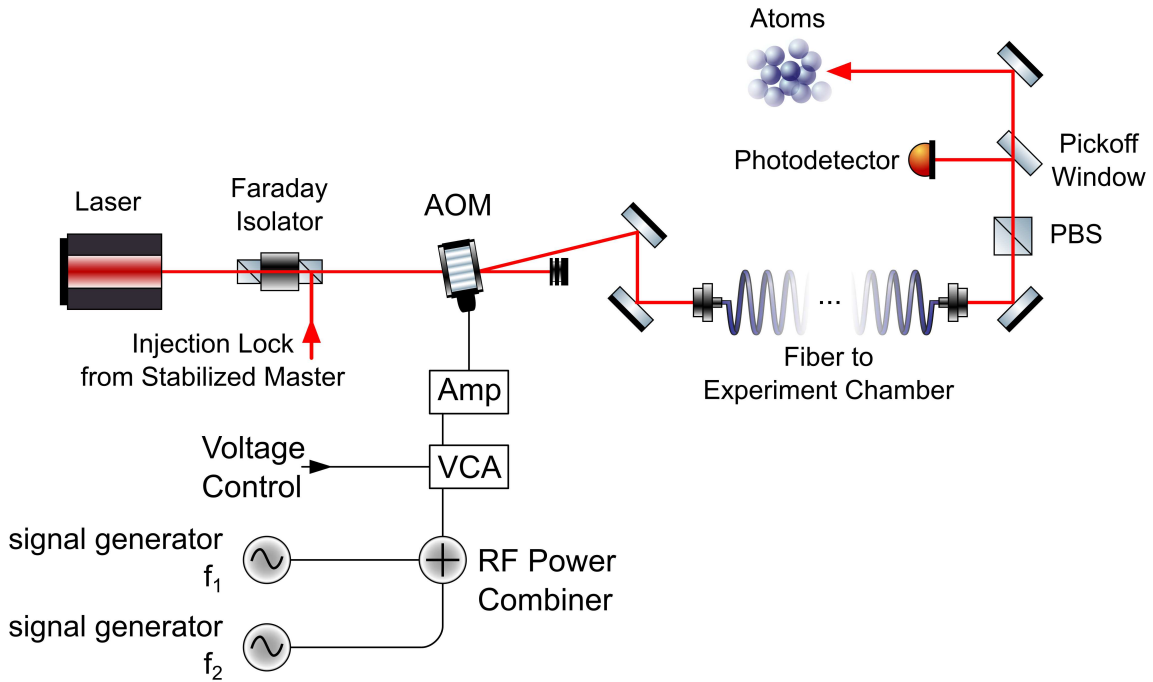


Figure 4.6 : PAS laser setup

Photoassociation laser schematic . A master laser is frequency-stabilized via saturated absorption spectroscopy to the  $^1S_0$ - $^3P_1$  atomic transition. After amplification with a diode slave laser, light at two controllable frequencies is generated with a single acousto-optic modulator (AOM) and delivered to the atoms with an optical fiber. The beat note between the two frequencies is monitored after the fiber.

determined by measuring dipole and breathing collective mode frequencies, which allow determination of trap volume and sample density.

#### 4.2.1 Photoassociation

After the atoms have equilibrated in the final ODT configuration, the PA lasers are applied (Fig. 4.1). A single acousto-optic modulator, driven with two RF frequencies,

is used to generate both PA beams. Light is derived from a frequency-stabilized master laser (Fig. 4.2) and coupled into a single-mode optical fiber with output optics that yield a  $320\ \mu\text{m}$  waist at the atoms, much larger than the size of the atom cloud. Both PA beams are linearly polarized along the same direction. The beat signal of the two light fields after the fiber is monitored on a photodiode and the RF powers are adjusted to ensure matched intensities for the two frequency components ( $I_1 = I_2 \equiv I$ ).

The sample temperature is low enough that collisions are entirely *s*-wave. The target state for the two-photon transition has total angular momentum  $J = 0$  and binding energy  $E_{b2}(< 0)$ .  $^{86}\text{Sr}$  has no nuclear spin and a  $^1S_0$  electronic ground state, leading to a single ground electronic molecular potential ( $\text{X}^1\Sigma_g^+$ ). The dominant intermediate state ( $b_1$ ) is the  $J = 1$  rotational state of the second least-bound ( $\nu = -2$ ) vibrational level on the  $0_u^+$  molecular potential, which asymptotically connects to the  $^1S_0$ - $^3P_1$  atomic transition at long range. This state is bound by  $44.246(10)$  MHz [? ]. We define  $\Delta_1 = \omega_1 - E_{b1}/\hbar$  and  $\Delta_2 = \omega_1 - \omega_2 - E_{b2}/\hbar$  as the one-photon detuning from state  $b_1$  and two-photon detuning from state  $b_2$  respectively for an initial scattering state with collision energy  $\epsilon = 0$ .  $\Omega_{2,12}$  is the Rabi frequency for coupling between states  $b_1$  and  $b_2$  due to the laser field at  $\omega_2$  with single-beam intensity  $I_2$ . Because the binding energy of the halo molecule is very small compared to  $\Delta_1$ , both laser frequencies are near resonance with the  $\nu = -2$  state. The transitions to the least-bound ( $\nu = -1$ )  $J = 1$  excited molecular state, bound by  $1.633(1)$  MHz, and the excited atomic state lie near enough in energy that they can effect our observations.

Photoassociation leads to loss of atoms from the trap through radiative decay from the intermediate, excited electronic state, and from collisions between molecules and background atoms. The PA spectrum is obtained by holding  $\omega_2$  fixed and varying  $\omega_1$ ,

which varies  $\Delta_2$  across resonance (Fig. 4.1).  $\Delta_1$  thus also varies slightly during a scan, but the spectra are so narrow compared to  $\Delta_1$  that we neglect this in our analysis. After an exposure time on the order of one hundred milliseconds, the number of ground-state atoms remaining and the sample temperature are measured with time-of-flight absorption imaging.

#### 4.2.2 Consideration of the trap depth

Show plots of the trap and how we determined what the trap depth was

Our previous discussion of the rate loss constant assumed we could describe the spatial distribution of the atomic density profile analytically. This is a valid superposition given two key assumptions, 1) the sample temperature remains constant during the PA exposure and 2) the trap is of sufficient depth that we can reasonably approximate it as a harmonic trap. [cite Mi's trap paper](#).

Analysis of the trapping conditions after acquisition of the data revealed that this second assumption was not maintained during our experiment. In some figure we can see that we only have an eta of 2. This is troublesome as it means we must numerically consider the density distribution over space when solving for the rate loss constant K.

In addition to the modified spatial distribution, we must also consider the effect of the trap depth on the energy profile of the trapped gas. In a typical high-eta trap, a typical Boltzmann profile is sufficient to describe the velocity distribution of the atoms and when we consider the distribution of relative energies that is important for PAS experiments, we recover a simple boltzmann weighting for the distribution of energy probabilities. This is shown in [sopme app](#).

However, the case of a low- $\eta$  trap we must define a local cutoff energy at each point in space within the trap as atoms that have an energy higher than the local  $\eta$  value are assumed to be lost from the trap. Derivation of this truncated relative energy probability distribution is given in [some app](#) and results in a stronger weighting of the coldest atoms near the bottom of the trap.

### 4.3 Theoretical description

This section develops the more groddy form of the BJ equation. Include the

In Ch. [somewhere](#) we discussed the usual situation for observing loss due to photoassocition. This experiment was similar to the 88 autler townes experiment.

PA loss is described with a local equation for the evolution of the atomic density

$$\dot{n} = -2Kn^2 - \Gamma n, \quad (4.1)$$

where the laser-frequency dependence of the collision-event rate constant,  $K$ , determines the spectrum of the PA loss. The one-body loss rate,  $\Gamma$ , is due to background collisions and off-resonant scattering from the PA lasers. By integrating this equation over the trap volume, we can obtain the evolution of the total number of trapped atoms

$$N(t) = \frac{N_0 e^{-\Gamma t}}{1 + \frac{2N_0 \langle K \rangle V_2}{\Gamma V_1^2} (1 - e^{-\Gamma t})} \quad (4.2)$$

where  $N_0$  is the number of trapped atoms at the beginning of the PAS interaction time. The effective trap volumes  $V_q$  are

$$V_q = \int_V d^3r e^{-\frac{qU(r)}{k_B T}}, \quad (4.3)$$

for trapping potential  $U(\mathbf{r})$ .  $\langle K \rangle$  is the trap-averaged collision event rate constant

$$\begin{aligned} \langle K \rangle &= \frac{1}{V_2} \int_V d^3 r e^{-\frac{2U(\mathbf{r})}{k_B T}} \\ &\times \frac{1}{h Q_T} \int_0^{\epsilon_{\max}(\mathbf{r})} d\epsilon |S|^2 e^{-\epsilon/k_B T}, \end{aligned} \quad (4.4)$$

which is itself a thermal average of the scattering probability for loss ( $|S(\epsilon, \omega_1, \omega_2, \dots, \mathbf{r})|^2$ ) over the collision energy  $\epsilon$ , with an energy cutoff  $\epsilon_{\max}$  to be discussed momentarily. The trapping potential is given by  $U(\mathbf{r}) = mgz + h\chi_{1064,g}I_{1064}(\mathbf{r}) - \tilde{U}_{\min}$ , where  $mgz$  is the gravitational potential at height  $z$ ,  $I_{1064}(\mathbf{r})$  is the intensity of the trapping light, and  $\chi_{1064,g} = 11 \text{ Hz}/(\text{W/cm}^2)$  [? ] is proportional to the polarizability of ground state atoms due to 1064 nm light.  $\tilde{U}_{\min}$  is subtracted to set the potential at the trap minimum to zero. The spatial integral is restricted to regions around the trapping local minimum with  $U(\mathbf{r})$  less than the trap depth [? ]. Downhill regions on the other side of the saddle point defining the trap depth are excluded. The laser intensity profile is measured independently, and the potential is found to be consistent with measured trap oscillation frequencies. The partition function is  $Q_T = \left(\frac{2\pi k_B T \mu}{h^2}\right)^{3/2}$  for reduced mass  $\mu = m/2$  and sample temperature  $T$ , for atoms of mass  $m$ .

Equation (3.32) provides the correct thermal average when the collision-energy distribution does not need to be truncated ( $\epsilon_{\max} \rightarrow \infty$ ). For our data, however, the ratio of sample temperature to trap depth is  $k_B T/U_{\text{depth}} \approx 3$  for samples with temperature above 100 nK and drops to unity for 30 nK samples, so truncation effects are important. If the single-particle kinetic-energy distribution function is a Boltzmann truncated at  $U_{\text{depth}} - U(\mathbf{r})$ , then the collision-energy distribution follows a Boltzmann distribution at low energies [ $\epsilon \ll U_{\text{depth}} - U(\mathbf{r})$ ] and falls off more quickly at larger energies, reaching zero at  $2[U_{\text{depth}} - U(\mathbf{r})]$ . We find that this treatment predicts a

narrower distribution on the red side of the spectral line than we observe in our data, suggesting the presence of atoms in non-ergodic orbits with energies above the saddle point of the trap. This is not surprising given the large collisional loss rate associated with near-resonant scattering in this isotope. Fortunately, the molecular binding energy is strongly determined by the sharp edge of the spectrum on the blue side of the line, which is relatively insensitive to the description of the red tail. Our data is fit well with a truncated Boltzmann distribution of collision energies [Eq. (3.32)]. To estimate the systematic uncertainty introduced by this treatment, we perform fits with  $\epsilon_{\max}$  equal to  $2[U_{\text{depth}} - U(\mathbf{r})]$  and  $U_{\text{depth}} - U(\mathbf{r})$  and take the mean of the two results as the best value for the binding energy and half the difference as a systematic uncertainty  $\sigma_{\epsilon_{\max}} \approx 100 \text{ Hz}$ . This procedure does not correctly represent the overall normalization of  $\langle K \rangle$ , but we are not concerned with overall signal amplitude in this study. Atom temperatures vary by no more than 20% during the interaction time, so assuming a constant sample temperature is reasonable.

Bohn and Julienne [? ] provide an expression for  $|S(\epsilon, \omega_1, \omega_2, \dots)|^2$  for a collision on the open channel of two ground state atoms (g) with total energy  $\epsilon$  leading to loss-producing decay from the excited state  $b_1$  with rate  $\gamma_1$  (Fig. 4.1),

$$|S|^2 = \frac{(\Delta_2 + \epsilon/\hbar)^2 \gamma_1 \gamma_s}{\left[ (\Delta_1 + \epsilon/\hbar)(\Delta_2 + \epsilon/\hbar) - \frac{\Omega_{12}^2}{4} \right]^2 + \left[ \frac{\gamma_1 + \gamma_s}{2} \right]^2 (\Delta_2 + \epsilon/\hbar)^2}. \quad (4.5)$$

For simplicity, we have omitted the light shift of  $b_1$  due to coupling to the scattering continuum [? ]. This approach was found to be sufficient for describing two-photon spectroscopy to a more deeply bound molecular level in  $^{88}\text{Sr}$  [? ]. Equation (3.33) neglects all light shifts due to the trapping laser. Light shifts due to the photoassociation

lasers coupling to states outside our model (Fig. 4.1) are also neglected. The thermal energy is much greater than the zero-point energy for trap motion,  $T \gg h\nu_{\text{trap}}/k_B$ , so confinement effects are negligible [? ].  $\gamma_1 = 2\gamma_{\text{atomic}}$ , where  $\gamma_{\text{atomic}} = 4.7 \times 10^4 \text{ s}^{-1}$  is the decay rate of the atomic  ${}^3P_1$  level.  $\gamma_s(\epsilon)$  is the stimulated width of  $b_1$  due to coupling to the initial scattering state by laser 1, which for low energy can be expressed as [18? , 52]

$$\gamma_s(\epsilon) = 2kl_{\text{opt}}\gamma_1, \quad (4.6)$$

where the optical length ( $l_{\text{opt}} \propto I_1$ ) is related to the overlap between the initial colliding state and  $b_1$ , and  $k = (2\mu\epsilon)^{1/2}/\hbar$ . We take the intermediate state  $b_1$  as the  $\nu = -2$  state, for which  $l_{\text{opt}}/I = (1.5 \pm 0.3) \times 10^4 a_0/(\text{W/cm}^2)$  [? ], where  $a_0 = 5.29 \times 10^{-11} \text{ m}$  is the Bohr radius.

For the experiments reported here, we maintain significant intermediate-state detuning,  $\Delta_1$ , for which  $|\Delta_1| \gg |\Omega_{2,12}|$ . Thus we are in a Raman configuration, and not in the Autler-Townes regime [? ]. In the Raman regime, Eq. 3.33 shows a maximum near two-photon resonance at  $\Delta_2 + \epsilon/\hbar = \Omega_{2,12}^2/4\Delta_1$ . Following a treatment discussed recently for a similar experiment in calcium [52], if the detuning is restricted to near two-photon resonance then  $|S|^2$  can be approximated as a Lorentzian

$$|S|^2 \approx \frac{A(\epsilon)}{\left(\Delta_2 + \epsilon/\hbar - \frac{\Omega_{2,12}^2}{4(\Delta_1 + \epsilon/\hbar)}\right)^2 + [\Gamma_L(\epsilon)/2]^2}, \quad (4.7)$$

where

$$A(\epsilon) = \frac{\Omega_{2,12}^4 \gamma_1 \gamma_s(\epsilon)}{16(\Delta_1 + \epsilon/\hbar)^4} \quad (4.8)$$

$$\Gamma_L(\epsilon) = \frac{\Omega_{2,12}^2 [\gamma_1 + \gamma_s(\epsilon)]}{4(\Delta_1 + \epsilon/\hbar)^2}. \quad (4.9)$$

In practice, the variation of collision energy is negligible compared to the one-photon detuning  $\Delta_1$ .

There are several concerns regarding the rigorous application of the Bohr and Julianne theory [? ] to our experiment. The obvious one is that it assumes an isolated intermediate state, which is not always a good approximation because of the proximity of state  $b_1$  to the  ${}^1S_0 + {}^3P_1$  asymptote and to the  $\nu = -1$  state. Because of the small decay rate  $\gamma_1$  of the intermediate molecular state associated with metastable  ${}^3P_1$  atomic state, we also expect that loss from the ground molecular state cannot be neglected.

The more subtle issue is that Eq. (3.34) is derived assuming only a single laser beam is near resonant with each leg of the two-photon transition, which is not a good approximation for two-photon spectroscopy of a halo state and the resulting small laser-frequency difference  $\omega_1 - \omega_2 \approx -E_{b2} \ll |\Delta_1|$ . We can expect that coupling between pairs of states due to both photoassociation lasers will contribute to the transition strength and light shifts of the levels induced by the photassociation lasers [? ? ].

In the absence of a more complete theory treating these effects, we analyze loss spectra using the effective expression given by Eq. (4.10), where the observed molecular binding energy ( $E'_{b2}$ ) includes any perturbations due to AC Stark or collisional

$$|S|^2 = \frac{\Gamma_L(\epsilon) + \gamma_{\text{eff}}}{\Gamma_L(\epsilon)} \times \frac{\eta A(\epsilon)}{(\omega_1 - \omega_2 + \epsilon/\hbar - E'_{b2}/\hbar)^2 + \left[ \frac{\Gamma_L(\epsilon) + \gamma_{\text{eff}}}{2} \right]^2}, \quad (4.10)$$

shifts.

Parameters have been added in Eq. (4.10) to account for deviations of the signal strength ( $\eta$ ) and width ( $\gamma_{\text{eff}}$ ) from the predictions of [? ]. If deviations from Eq. (3.34) are small, we expect  $\eta \sim 1$ ,  $\gamma_{\text{eff}} \sim 0$ , and  $E'_{b2} \sim E_{b2} + \Omega_{2,12}^2/4(\Delta_1 + \epsilon/\hbar)$ .

Light shifts (AC Stark shifts) due to the trapping lasers and collisions with ground-state atoms (density  $n$ ) should contribute to shifts of molecular resonance. Similar effects were taken into account in a recent, high-precision study of weakly bound molecular states of ultracold ytterbium atoms [10]. In addition, we expect that both 689-nm excitation lasers will shift the line, not just  $I_2 \propto \Omega_{2,12}^2$ . We model the relationship between the measured resonance positions and the unperturbed binding energy  $E_{b2}$  as

$$E'_{b2} = E_{b2} + h\chi_{689}I_{689} + h\chi_{1064}I_{1064}(\mathbf{r}) + h\chi_n n(\mathbf{r}). \quad (4.11)$$

The susceptibilities, in Hz per unit intensity or density, will be determined from experimental data or theoretical considerations. The variation with position of the trapping laser intensity ( $I_{1064}$ ) and the density give rise to the spatial dependence of  $|S|^2$  and the need for a spatial average in Eq. (3.32). We take  $I_{689}$  as twice the single-beam intensity  $I_{689} = 2I$ . The 689-nm excitation beam is large enough compared to the atom sample to neglect spatial variation. The functional form for the AC Stark shift due to the excitation lasers is discussed in Sec. ??.

#### 4.4 Spectral fitting and determination of energy shifts

Figure 4.3 shows a series of spectra for different final trap depths and sample temperatures. The characteristic asymmetric lineshape for excitation of a thermal sample is evident, with width decreasing as sample temperature decreases. The molecular

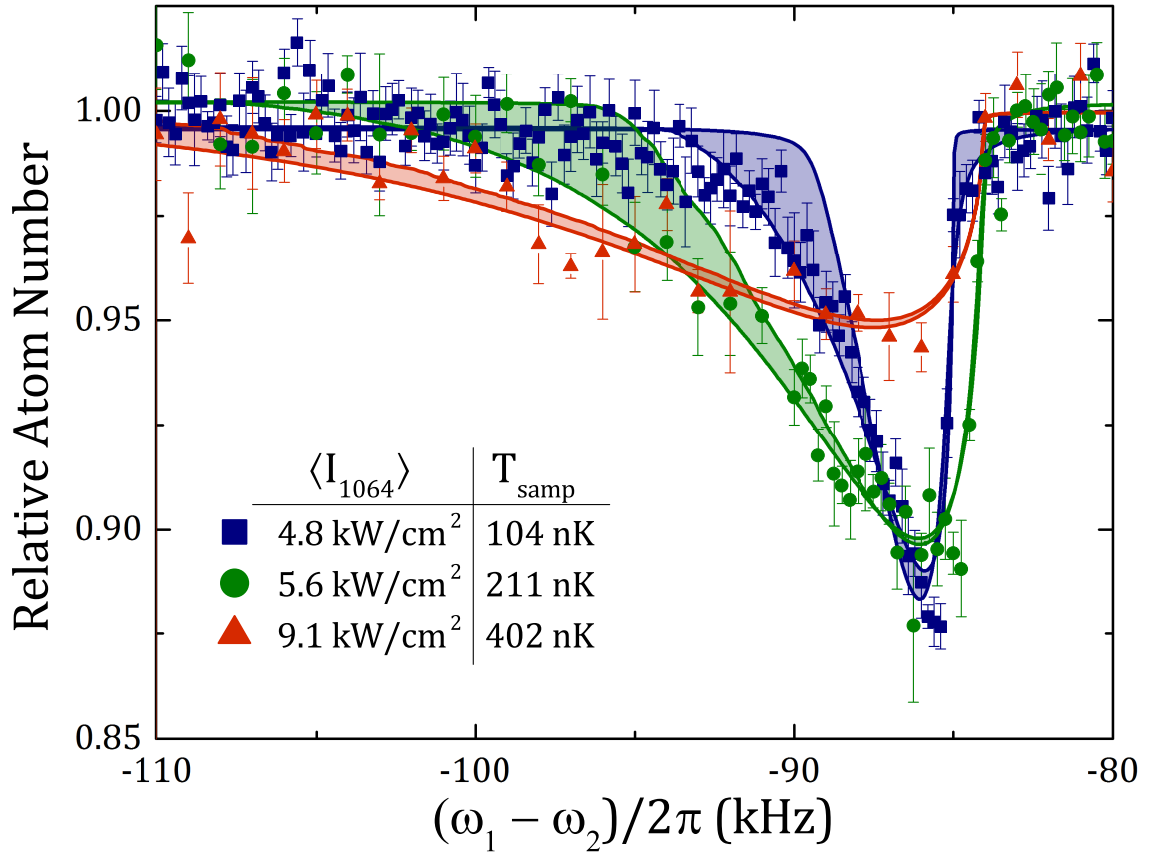


Figure 4.7 : Variation of 1064 nm trap depth

Atom-loss spectra as a function of two-photon difference frequency  $(\omega_1 - \omega_2)/2\pi$  for intermediate detuning  $\Delta_1/2\pi = -9 \text{ MHz}$ . Sample temperature and average trapping laser intensity are indicated in the legend. The single-beam excitation laser intensity is  $I = 25 \text{ mW}/\text{cm}^2$  for the 104 nK spectrum and  $I = 48 \text{ mW}/\text{cm}^2$  for the 211 nK and 402 nK spectra. Fits are described in the text, with the two boundaries of each band given by the fits with collision-energy truncation  $\epsilon_{\max}$  equal to  $2[U_{\text{depth}} - U(\mathbf{r})]$  and  $U_{\text{depth}} - U(\mathbf{r})$ .

binding energy is close to the sharp edge on the blue side of each spectrum.

We fit atom-loss spectra with Eq. (4.2) for the evolution of atom number with time, using the phenomenological expression Eq. (4.10) for the scattering probability and Eq. (3.32) for the average of the collision event rate constant over the trap volume and collision energy. The sample temperature, perturbed resonance frequency  $E'_{b2}$ ,  $\eta$ , and  $\gamma_{\text{eff}}$  are taken as fit parameters. In the final analysis, temperatures are set to values determined from time-of-flight imaging of the atoms, but when they are allowed to vary, the fit values differ by no more than 10%. Approximately 10 spectra are recorded for each set of experimental parameters, and the spread of resulting fit values are used to determine best values and uncertainties.

#### 4.4.1 AC Stark shift due to excitation lasers

The most significant perturbation to the resonance position is the AC Stark shift due to the excitation laser intensity, as shown in Fig. 4.4.1. For this data, the trap parameters, temperature ( $T = 30 \text{ nK}$ ), and initial peak sample density ( $n_0 = 2 \times 10^{12} \text{ cm}^{-3}$ ) are held constant. We vary the single-beam excitation intensity from  $I = 0.02 - 0.06 \text{ mW/cm}^{-2}$ , and the excitation time is 50 ms. The observed shifts are comparable to the thermal width of the spectrum, allowing a precise determination of  $\chi_{689} = -21(1)(2) \text{ kHz/(W/cm}^2)$  from a linear fit to the resonance positions,  $E'_{b2} \propto h\chi_{689}I_{689}$  (Fig. 4.9). The first quoted uncertainty is statistical and it arises from variations in parameters and fluctuations in the measured intensity during the scans. The second value is systematic, reflecting uncertainty in laser-beam size and intensity profile at the atoms. All parameters beside the 689-nm laser intensity are held fixed for this data set, and the AC Stark shift is not correlated with any other variable,

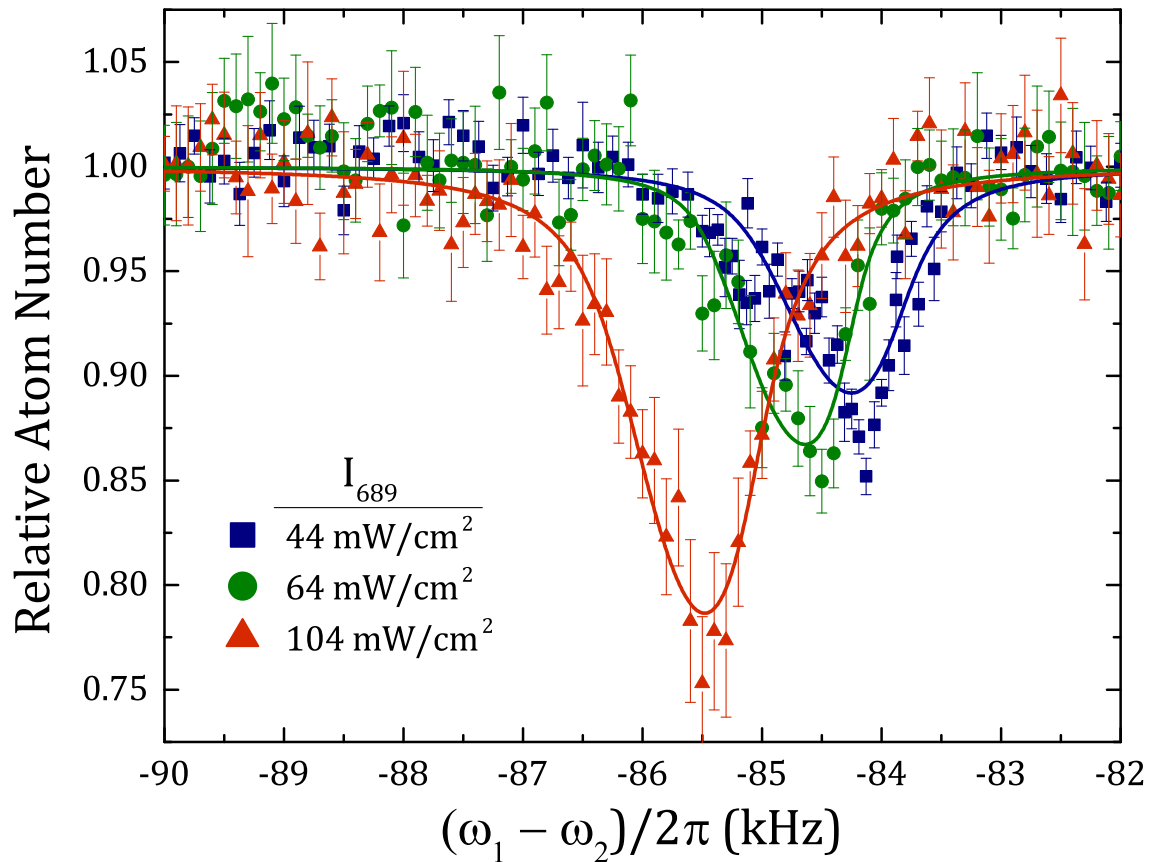


Figure 4.8 : Variation of 689 nm excitation

Atom-loss spectra as a function of two-photon difference frequency  $(\omega_1 - \omega_2)/2\pi$  for intermediate detuning  $\Delta_1/2\pi = -9 \text{ MHz}$  and various 689-nm excitation laser intensities . Twice the single-beam intensity  $I_{689} = 2I$  is indicated in the legend.

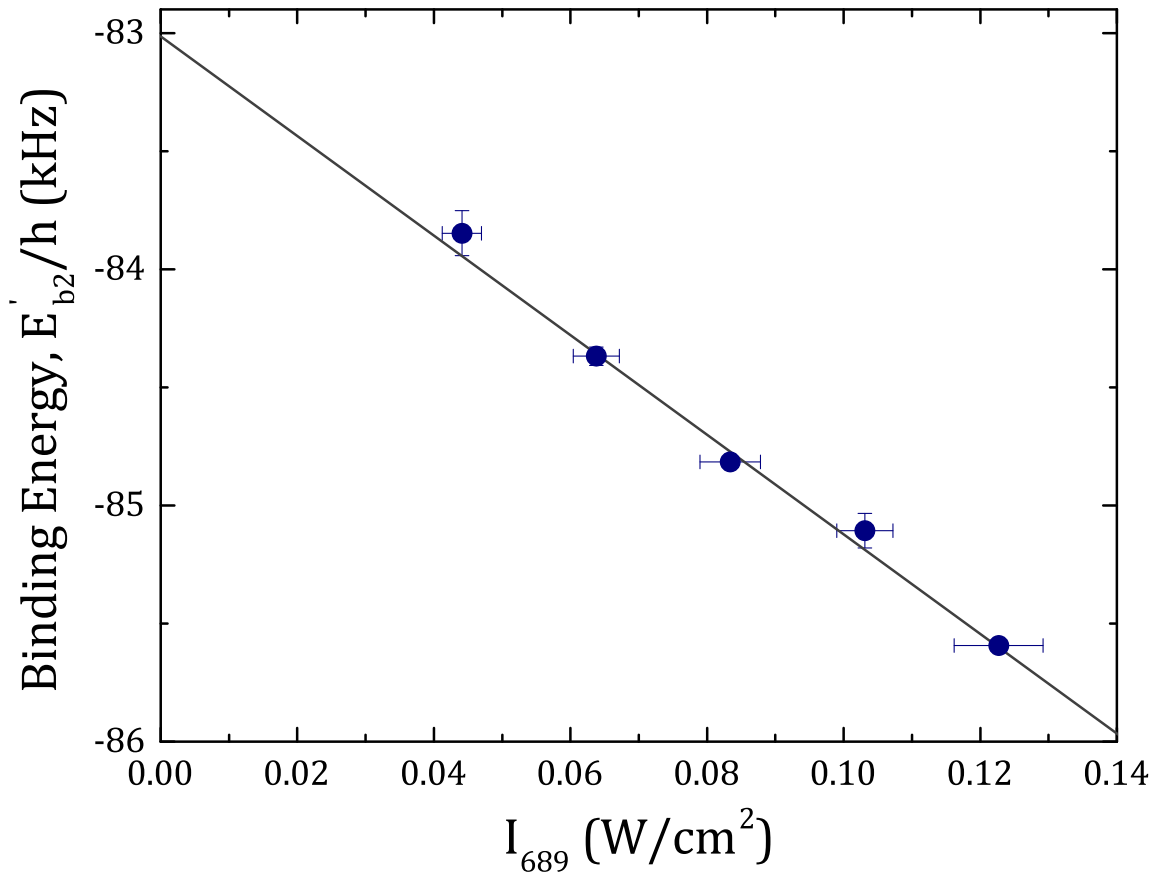


Figure 4.9 : Fit of 689 nm AC Stark shift

Measured resonance position  $E'_{b2}$  plotted versus twice the single-beam intensity  $I_{689} = 2I$ . The linear fit provides the AC Stark shift parameter  $\chi_{689}$ .

such as density or trap intensity. We thus obtain an accurate measure of  $\chi_{689}$  without attempting to account for other systematic shifts of  $E'_{b2}$  in this data. A study of the dependence of  $\chi_{689}$  on detuning from the excited molecular state will be discussed in Sec. ??.

Broadening to the red of the spectrum reflects the distribution of atom-atom collision energies, while broadening to the blue is most sensitive to decay of the intermediate state ( $\Gamma_L$ ) and the phenomenological broadening term  $\gamma_{\text{eff}}$  [Eqs. (4.9) and (4.10)]. The long lifetime of the excited state and the significant detuning  $\Delta_1$  result in a width  $\Gamma_L(\epsilon)$  less than 5 Hz for all conditions. This is extremely small compared to observed width, which yields values of  $\gamma_{\text{eff}}$  on the order of 300 Hz. We hypothesize that this width reflects decay of molecules in the electronic ground-state due to collisions with background atoms.

#### 4.4.2 Density-dependent frequency shift

A shift of the two-photon resonance position is possible due to differing mean-field shifts of initial atomic and final molecular states arising from interaction with the background of ground-state atoms. Such a shift would be proportional to the atom density and depend upon the *s*-wave scattering lengths for atom-atom and atom-dimer collisions,  $a_{86}$  and  $a_{\text{ad}}$  respectively. This was observed in a Rb Bose-Einstein condensate (BEC) in [68]. For a non-degenerate gas, this effect yields  $\chi_n = \hbar(\frac{a_{\text{ad}}}{\mu_{\text{ad}}} - 4\frac{a_{86}}{\mu_{\text{aa}}}) = \frac{\hbar}{m}(\frac{3}{2}a_{\text{ad}} - 8a_{86})$ , where  $\mu_{\text{ad}}$  and  $\mu_{\text{aa}}$  are the reduced masses for molecule-atom and atom-atom collisions respectively. Note that the shift would vanish for  $a_{\text{ad}} = (16/3)a_{86}$ .

The largest density used in our experiment ( $\sim 1 \times 10^{12} \text{ cm}^{-3}$ ) is relatively low

compared to typical BEC densities, and at this time we are unable to accurately measure a variation of resonance position with density. However, the atom-atom scattering is close to resonance and thus Efimov physics can provide information on  $a_{\text{ad}}$  [13, 50] and an estimate of the systematic error introduced by any residual density-dependent frequency shifts. For a zero-range interaction, the atom-dimer scattering length is related to the atom-atom scattering length through the three-body Efimov parameter  $\kappa_*$  according to [13]

$$a_{\text{ad}} = a_{86} \{1.46 + 2.15 \cot[s_0 \ln(14.1 \kappa_* a_{86})]\} \quad (4.12)$$

where  $s_0 = 1.006$ <sup>\*</sup>.

In principle, the atom-dimer scattering length can take any value. However, for a deep atom-atom potential, such as for the ground-state strontium dimer [58], there is a universality of the three-body physics that sets  $\kappa_* = 0.226(2)/l_{\text{vdW}}$  [66]. Here,  $l_{\text{vdW}} = (2\mu C_6/\hbar^2)^{1/4}/2 = 74.6 a_0$  is the van der Waals length associated with the  $C_6$  coefficient of the long-range  $\text{Sr}_2$  ground-state potential. We use  $C_6 = 3.03(1) \times 10^{-76} \text{ J m}^6$  found from a fit of potential parameters to spectroscopic data [58], which is consistent with a recent *ab initio* calculation [71]. This yields  $\kappa_* = 5.72 \times 10^7 \text{ m}^{-1} = (330 a_0)^{-1}$ . Equation (4.12) then predicts  $a_{\text{ad}} = 6.4 a_{86}$ , which leads to a small density-dependent frequency shift parameter of  $\chi_n = 50 \text{ Hz}/(10^{12} \text{ cm}^{-3})$ . A numerical calculation including a finite-range correction for the atom-atom interaction [45] results in  $a_{\text{ad}} = 3.5 a_{86}$  and  $\chi_n = -90 \text{ Hz}/(10^{12} \text{ cm}^{-3})$ . Thus, a very small shift is expected for the densities used here. We incorporate  $\chi_n = 0 \pm 90 \text{ Hz}/(10^{12} \text{ cm}^{-3})$  as a set parameter in our

---

<sup>\*</sup>The Efimov parameter is related to  $E_{3b}^0$  through  $\kappa_* = (m|E_{3b}^0|/\hbar^2)^{1/2}$ , where  $E_{3b}^0$  is the binding energy the lowest Efimov trimer would have in the case of resonant atom-atom interactions.

model of the spectrum, where we set the systematic uncertainty to reflect the spread of theory predictions. This uncertainty will be significant for our determination of the unperturbed halo binding energy.

#### 4.4.3 AC Stark Shift due to Trapping Lasers

With an accurate determination of  $\chi_{689}$  and a value for  $\chi_n$ , we use the data shown in Fig. 4.3 to determine the susceptibility for the AC Stark shift from the trapping laser,  $\chi_{1064}$ , and the unperturbed halo binding energy  $E_{b2}$ . Figure 4.4.3 shows a plot of  $E'_{b2} - \chi_{689}I_{689} - \chi_n\langle n \rangle$  versus  $\langle I_{1064} \rangle$ , where  $E'_{b2}$  is the resonance position from each fit and  $\langle \dots \rangle$  indicates a weighted average of the quantity over the trapped sample, with a weighting given by the square of atom density. This weighting reflects the contribution to photoassociative loss, a two-body process. The plotted uncertainties in  $E'_{b2} - \chi_{689}I_{689} - \chi_n\langle n \rangle$  are from statistical variation in the fit parameters. The typical average density is  $\langle n \rangle \approx 1 \times 10^{12} \text{ cm}^{-3}$ . The linear fit function is to  $E_{b2} + \chi_{1064}\langle I_{1064} \rangle$ . In addition to statistical uncertainty, we have systematic uncertainty from  $\chi_n$  and treatment of the truncation of the collision-energy integral [Eq. (3.32)]. The dashed lines shown in Fig. 4.4.3 are resulting fits when the values of  $E'_{b2} - \chi_{689}I_{689} - \chi_n\langle n \rangle$  are shifted by the sum of these systematic uncertainties. The resulting value for the unperturbed binding energy is  $E_{b2}/h = -83.00(7)(20) \text{ kHz}$ , where the first uncertainty is statistical, and the second is systematic. We observe a susceptibility to  $I_{1064}$  of  $\chi_{1064} = 0 \pm 10 \text{ Hz/(kW/cm}^2)$ .

For two-photon spectroscopy to a weakly bound dimer, it is typical to neglect any potential AC Stark shift due to far-off-resonant trapping lasers because the atoms contribute to the overall polarizability approximately as free atoms. But the high

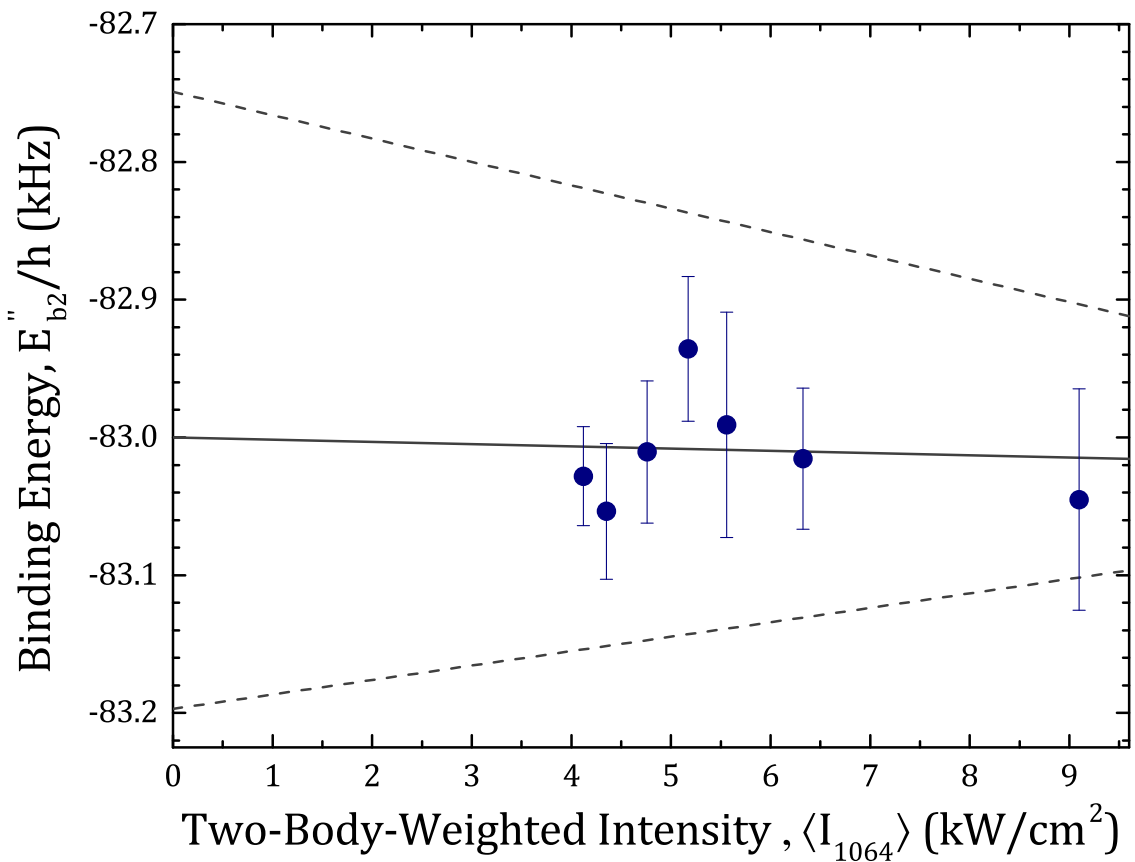


Figure 4.10 : Measurement of halo state susceptibility,  $\chi_{1064}$

Measured resonance positions corrected for excitation-laser AC Stark shift and collisional frequency shift,  $E'_{b2} - \chi_{689} I_{689} - \chi_n \langle n \rangle$ , as a function of average trap laser intensity  $\langle I_{1064} \rangle$  for the data such as in Fig. 4.3 . The trend line and confidence intervals are described in the text.

precision of our measurement allows us to detect a small shift. This corresponds to a relative differential polarizability of  $\chi_{1064}/2\chi_{1064,g}g = (\chi_{1064,b2} - 2\chi_{1064,g}g)/2\chi_{1064,g}g \approx xx$ .

## 4.5 Unperturbed halo binding energy

In the limit of extremely small binding energy, and thus resonant atom-atom interactions, the binding energy of a halo molecule is approximately given by [38]

$$E_b = -\hbar^2/2\mu a^2. \quad (4.13)$$

For interactions described at long-range by the van-der-Waals form,  $V(r) = -C_6/r^6$ , as with ultracold atoms, a convenient figure of merit for quantifying how accurate this simple expression should be is given by the ratio of the *s*-wave scattering length to the mean scattering length or interaction range, closely related to the van der Waals length through [30, 17]

$$\bar{a} = l_{\text{vdW}} \frac{\Gamma(\frac{3}{4})}{\sqrt{2}\Gamma(\frac{5}{4})}. \quad (4.14)$$

Slightly away from resonance, corrections to the binding energy for the van der Waals potential were worked out in [26, 27], yielding

$$E_{b2} = -\frac{\hbar^2}{2\mu(a - \bar{a})^2} \left[ 1 + \frac{g_1 \bar{a}}{a - \bar{a}} + \frac{g_2 \bar{a}^2}{(a - \bar{a})^2} + \dots \right], \quad (4.15)$$

where  $g_1 = \Gamma(1/4)^4/6\pi^2 - 2 = 0.918\dots$  and  $g_2 = (5/4)g_1^2 - 2 = -0.947\dots$ . The range of validity of this expression is  $a \gtrsim 2\bar{a}$ . The accuracy of the first term in this expansion has been experimentally confirmed for various systems such as  $^{85}\text{Rb}$  [22, 36],  $^{40}\text{K}$  [54, 47] and  $^6\text{Li}$  [3]. This derivation of Eq. (4.15) assumes that the influence of short-range physics, which can be expressed through a quantum defect, varies negligibly

from threshold to the molecular binding energy. We expect this to be an excellent approximation, since, as shown in Ref. [26] the corrections are typically less than about 1% even for GHz binding energies.

For ground-state  $^{86}\text{Sr}$  atoms,  $\bar{a} = 71.3 a_0$ . The most accurate value available for the s-wave scattering length is  $a = 798(12) a_0$  [58], satisfying the requirement of  $a \gg \bar{a}$  for the least-bound state on the ground molecular potential to be a halo molecule. Nonetheless,  $\bar{a}/(a - \bar{a}) = .10$ , and the corrections given by Eq. (4.15) are significant. Figure 4.5 shows the importance of the correction terms.

Equation (4.15) and the previous best value of the scattering length [58] predict a binding energy of  $E_{b2} = -86(3)$  kHz. This agrees with our measurement, but by inverting Eq. (4.15), we can use our increased accuracy in  $E_{b2}$  to extract an improved value of the scattering length of  $a = 810.6(3)(9) a_0$ , where uncertainties reflect statistical and systematic uncertainties in  $E_{b2}$  respectively. The next higher-order term in  $x_0 = \bar{a}/(a - \bar{a})$  is likely to introduce a correction on the order of 100 Hz in Eq. (4.15), creating a systematic uncertainty in  $a$  that is about one third of the uncertainty from our measurement.

## 4.6 Calculating the bound-bound Frank-Condon factor

The proximity of  $^{86}\text{Sr}$  to a scattering resonance and the susceptibility of the halo binding energy to the intensity of the excitation light suggests using light to tune the binding energy and scattering length as was done with optically assisted magnetic Feshbach resonances [4, 21], which is closely related to the use of optical Feshbach resonances [? 65, 69, 8, 70]. Understanding the frequency-dependence of  $\chi_{689}$  is

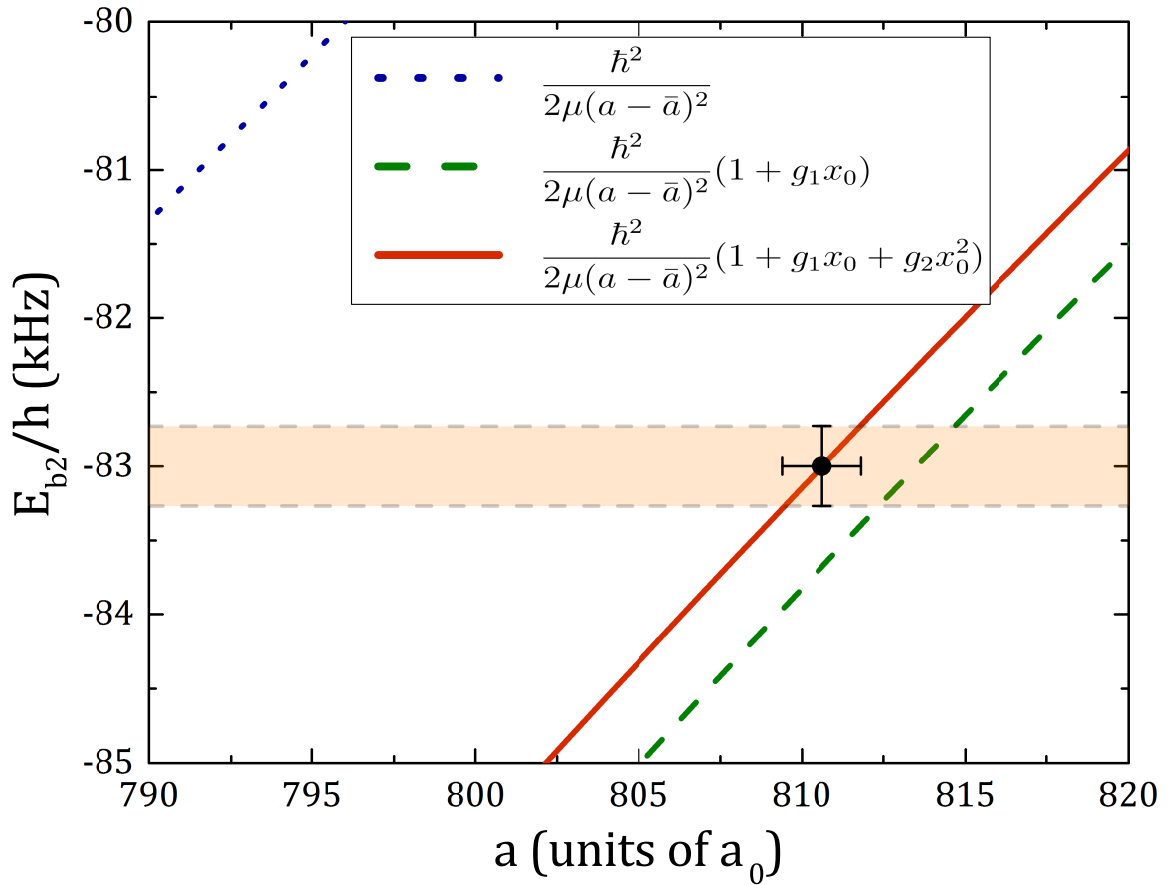


Figure 4.11 : Determination of  $^{86}\text{Sr}$  scattering length

Halo binding energy versus  $s$ -wave atom-atom scattering length for  $^{86}\text{Sr}$ . The shaded region indicates our experimental measurement. The lines are predictions of Eq. 4.15 retaining up to the first, second, and third terms as indicated in the legend [ $x_0 = \bar{a}/(a - \bar{a})$ ]. The data point is the prediction of Eq. (4.15) for the recommended value of the measured binding energy.

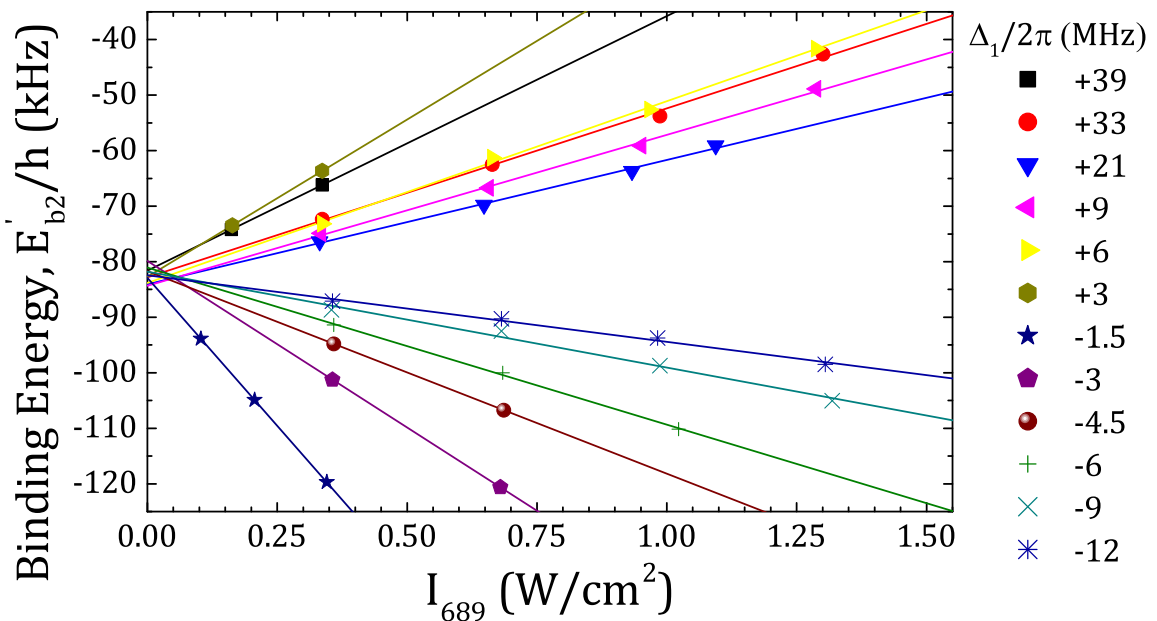


Figure 4.12 : Variation of halo susceptibility as a function of  $\Delta_1$

Two-photon PA resonance positions as a function of twice the single-beam excitation intensity,  $2I = I_{689}$  for various intermediate state detunings,  $\Delta_1$  .

important for investigating this possibility, so we extracted this parameter from spectra at a wide range of 689-nm laser intensities and detuning from the intermediate resonance ( $\Delta_1$ ).

Figure 4.5 shows the resulting resonance positions,  $E'_{b2}$ , versus twice the single-beam intensity,  $2I = I_{689}$ . The shift in molecular binding energy is linear with intensity over the explored range, but varies greatly in magnitude and sign. From linear fits, we extract the AC Stark shift parameter  $\chi_{689}(\Delta_1)$  through  $E'_{b2} \equiv E_{b2} + h\chi_{689}(\Delta_1)I_{689}$  (Fig. 4.6).

In the experiment, the total 689-nm intensity oscillates with 100% contrast according to  $I_{\text{total}} = I_1 + I_2 + 2\sqrt{I_1 I_2} \cos[(\omega_1 - \omega_2)t] = 2I \{1 + \cos[(\omega_1 - \omega_2)t]\}$ . The functional form we use to fit the AC Stark shift reflects the time average of the intensity and neglects the interference term. To confirm that this is the correct description, we numerically solved the time-evolution for a three-level system with similar optical couplings and oscillating optical intensity as present during two-photon PA of a halo state. The Hamiltonian is

$$H = \begin{pmatrix} 0 & \Omega_{01} [\cos(\omega_1 t) + \cos(\omega_2 t)] & 0 \\ \Omega_{01} [\cos(\omega_1 t) + \cos(\omega_2 t)] & E_{b1} & \Omega_{12} [\cos(\omega_1 t) + \cos(\omega_2 t)] \\ 0 & \Omega_{12} [\cos(\omega_1 t) + \cos(\omega_2 t)] & E_{b2} \end{pmatrix}$$

For  $\Omega_{01} \ll \Omega_{12} \ll |\Delta_1| \equiv |\omega_1 - E_{b1}/\hbar|$ , which is analogous to the experimental conditions used here, we find that the two-photon resonance is shifted by

$$\frac{\hbar\Omega_{12}^2}{4\Delta_1} + \frac{\hbar\Omega_{12}^2}{4(\Delta_1 - E_{b2}/h)} \approx \frac{\hbar\Omega_{12}^2}{2\Delta_1}. \quad (4.16)$$

This agrees with our observation of a shift that is linear with intensity, and implies that the susceptibility is related to the Rabi frequency for a single-beam intensity  $I$

through  $\chi_{689} \approx (\Omega_{12}/\sqrt{I})^2/(8\pi\Delta_1)$ .

This single-resonance model [Eq. (4.16)] describes the observed shifts well for detuning close to the  $\nu = -2$  state of the  $0_u^+$  molecular potential (small  $\Delta_1$ ). For large positive  $\Delta_1$ , however, at which  $\omega_1$  and  $\omega_2$  approach atomic resonance, deviations indicate coupling to one or more other states (Fig. 4.6). The most likely suspects are the  $\nu = -1, J = 1$  excited molecular state, bound by 1.633(1) MHz, and the  ${}^1S_0 + {}^3P_1$  continuum. The sign of the deviation indicates that AC Stark shift of colliding  ${}^1S_0$  atoms due to coupling to the  ${}^3P_1$  state is dominant in this regime. We have neglected shifts due to collisions and the trapping laser, which are small at the large excitation-laser intensities used here.

A fit of the single-resonance model as shown in Fig. 4.6 yields  $\Omega_{2,12}/2\pi \equiv \Omega_{12}/2\pi = 800$  kHz for  $I = 1$  W/cm<sup>2</sup>. Note that  $\Omega_{2,12}$  as defined here would be the splitting of the Autler-Townes doublet [52], which differs from the Bohn-Julienne definition of the molecular Rabi coupling [? ]. From the measured  $\Omega_{2,12}$ , one can extract the Franck-Condon factor,  $f_{FCF}$ , reflecting the overlap of the ground and intermediate molecular states through

$$\Omega_{2,12} = \sqrt{f_{ROT}} \sqrt{f_{FCF}} \gamma_{atomic} \sqrt{\frac{I}{2I_{sat,atom}}} \quad (4.17)$$

where  $I_{sat,atom} = 2\pi^2\hbar c\gamma_{atomic}/(3\lambda^3) = 3$   $\mu$ W/cm<sup>2</sup> is the atomic saturation intensity for the  ${}^1S_0 - {}^3P_1$  transition and  $I = I_{689}/2$  is the single-beam intensity. The rotational factor  $f_{ROT}$  accounts for the change in dipole moment from atom to molecule due to symmetry of the wave function and projection on a rotating molecular axis. Following the formalism described in [52],  $f_{ROT} = 2$  for the  $J = 1 \rightarrow 0$  bound-bound molecular transition studied here. This yields  $f_{FCF} = 0.03$ .

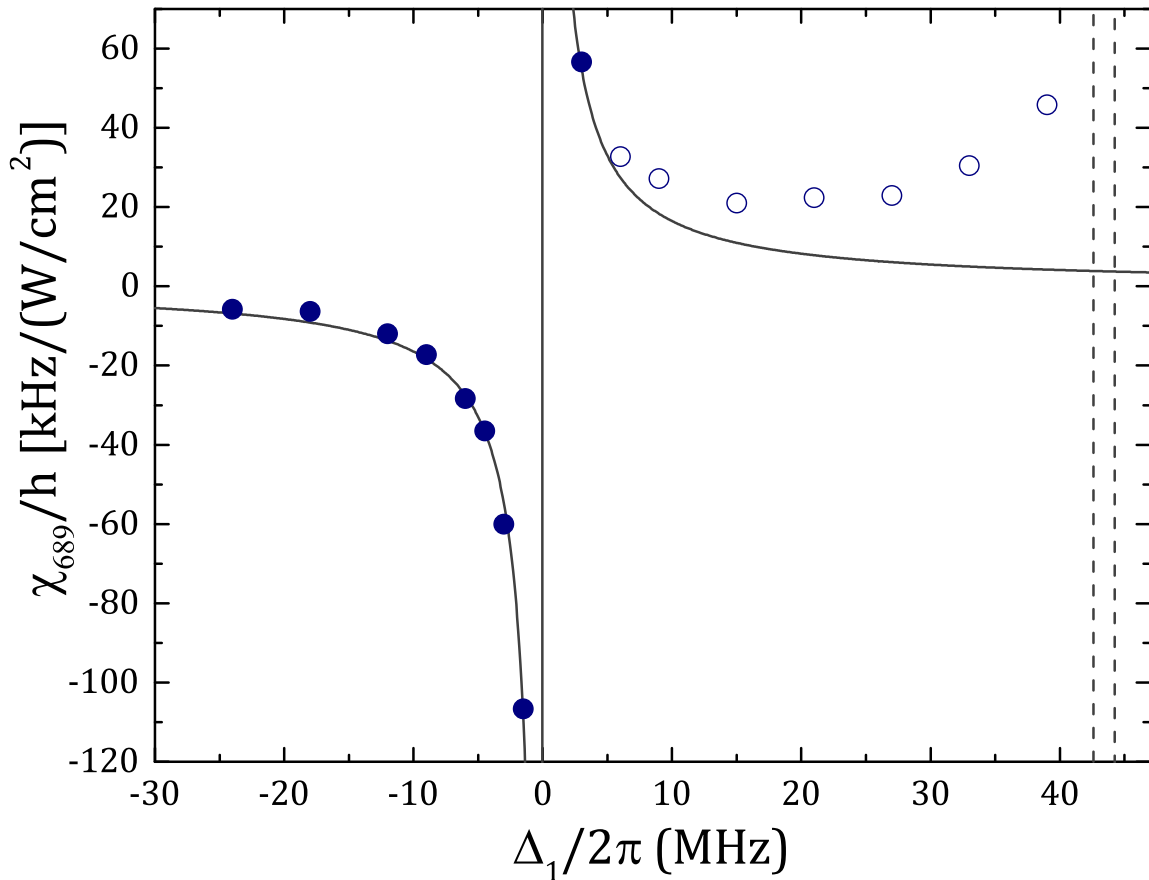


Figure 4.13 : Estimate of bound-bound coupling via isolated resonance model

AC Stark shift susceptibility,  $\chi_{689}$ . Dashed lines indicate the positions of the  $\nu = -1$ ,  $J = 1$  excited molecular state, bound by 1.633(1) MHz, and the  ${}^1S_0 + {}^3P_1$  continuum. Solid and open symbols show experimental measurements of the susceptibility. Using only the solid symbols, we fit a single resonance model of the form  $\chi_{689} \approx (\Omega_{12}/\sqrt{I})^2/(8\pi\Delta_1)$  and show this fit result as a solid line.

From the formula for the line shape we can see that it depends on the spatial distribution of the atoms. The standard approximation made when measuring these types of systems is to ensure loss does not cause heating of the atoms during photoassociation. Heating results in re-equilibration of the atomic density distribution, which in turn effects the rate of loss creation. Without independent controls to keep the system in thermal (and therefore spatial density) equilibrium.

What are the things the rate equation deals with?

We need the density distribution.

In a harmonic trap, there is a simple analytic form to the density distribution of a thermal gas. From Mi's work (and others) we know that this is only an approximation that is valid when  $\eta$  is approx greater than 4. When greater than 4 we can apply the high- $\eta$  approx and the trap frequencies along a particular direction reduce to  $\omega_{\text{eq}}$ .

However, the trap we did this experiment in were at  $\eta$ 's of 1 or less so we don't have an analytic solution to the spatial distribution. Since this could be a problem we need to know what the trap looks like.

We measure trap oscillation freq. at several different powers and model the trap using the utility outlined somewhere else.

From the numeric model, we can define a spatially dependent  $\eta$  which is determined by the local trap depth which is simply the difference between the local potential energy and the global depth. This is illustrated in fig something.

The spatial information is not only important for the density determination, but also for the range of available thermal energies. Consider two atoms near the local bottom of the trap. By definition, in equilibrium, a single atom may only have up

to the trap depths worth of energy since any additional energy would result in its expulsion from the trap. In this case, in a relative momentum frame, the allowed collision energies range from zero to two times the trap depth. Similarly, as we move towards the edge of the trap the range of accessible collision energies shrinks. This additional weighting factor may be viewed as having a local truncated Boltzmann distribution at every point in space.

Normally the BZ dist goes to infinity but here we have a cutoff at 2 trap depth. The most naive approx would be to simply consider the BZ and harshly truncate at 2 trap depth. We tried this

We know this is unphysical since we should expect that the probability of observing a certain momenta at a certain point in space, should smoothly tend zero towards as we approach the edge of the trap. To see what this looks like we (and determine how important the effect is) we rederive the relative momentum distribution.

{Some stuff about center of mass and relative}

What were all the cases and conclusions of having done this? Remember to consider what the different cases are. If the total relative energy can be X then how does that get split up? Use the plots to show this limiting behavior. Like if particle 1 has all the energy then there is only one possible value for particle 2 (and vice versa).

DERIVATION for truncated trap below

Need to lookup references for this molecular chaos assumption. What about ergodicity? How to discuss that we may not be completely ergodic?

What does my potential look like? Can I make it a piecewise function? How should I introduce this part?

Where does the f equation come from? I believe this is just the normalized boltz-

mann factor for probability to occupy a particlar state.

We can truncate this single particle distribution by

$$f_{\mathbf{r}}(\mathbf{p}) = A \left( \frac{1}{2\pi k_B T} \right)^{3/2} e^{\left( \frac{-p^2}{2mk_B T} \right)} \Theta \left( \epsilon_{max} - U(\mathbf{r}) - \frac{p^2}{2m} \right) \quad (4.18)$$

where A is a normalization constant which ensures  $\int_0^\infty f_{\mathbf{r}}(\mathbf{p}) d\mathbf{p} = 1$  and  $\Theta(x)$  is the Heaviside function defined by

$$\Theta(x) = \begin{cases} 1 & \text{if } x \geq 0, \\ 0 & \text{if } x < 0 \end{cases} \quad (4.19)$$

We got a certain answer with the way shown in the paper.

We can also use a completely different method that ignores all the consdierations of the last few sections. As was done in the calcium paper, we could simply fit the blue edge of the feature using a model function which can capture the high level features of the lineshape. Get the same answer. SHOW PLOTS TO THIS AFFECT AND COMPARE

Maybe go a little into the isolated resonance model (or at least recall), then tie into how we can measure the susceptibility across several different detunings which can give us the coupling to intermediate level. The first order analysis of this data suggest a bound-bound rabi freuqnecy of **BLAH**.

Point out the curling up at the end and say how the simple isolated resonacne model cannot predict. A full coupled channel calculation probably could but in the spirit of the Bohn and Julienne semi-classical approach, we set out to derive an approximate analytic expression to determine the binding energies. THis is presented in the next chapter.

Lastly, we note that in the context of photoassociation, the center-of-mass component of Eq.A.3 is not typically considered as typical PAS experiments are performed utilizing broad dipole allowed transitions which have linewidths much greater than the doppler width thus only the relative momentum between particles is important for determining the loss rate coefficient K discussed in [somewhere].

The case of PA using narrow intercombination line transitions found in alkaline-earth-metal atoms

In general K is considered as a boltzmann average over a single loss rate constant This can be seen in [20] Eq. 1 where the loss rate constant is given by

$$\begin{aligned} K(\Delta, T) &= \langle \mathcal{K}(\Delta, \mathbf{P}_c, \mathbf{p}_r) \rangle \\ &= \int d^3 \mathbf{P}_c f_M(\mathbf{P}_c) \int d^3 \mathbf{p}_r f_\mu(\mathbf{p}_r) \mathcal{K}(\Delta, \mathbf{P}_c, \mathbf{p}_r) \end{aligned} \quad (4.20)$$

To this end we can integrate out the center of mass component to obtain the distribution most typically relevant to photoassociation.

By the time I've gotten to this I have already introduced K and that is not what I wanted to do.

conclusion here is the modified version of K we need for a trap that has a truncated energy distribution

to get there normal version of K is given in ch3 this K can be given in terms of f? this ver4sion of f is given in the appendix why do I integrate out the com component? typical PAS experiments utilize dipole allowed transitions which have linewidths many times larger than the

We now perform a change of variables using Eq. and Eq.A.2 can be rewritten as

Need to make a connection between dipole matrix element, wigner threshold, and infinite squarer step potential. This infinite square step can be viewed as a dilute ideal gas.

To prove this assumption I want to show that using the square step I can get the same equations like in Eq. 1 of the 99 paper. Then once we know the infinite energy behavior (valid for only a particular portion of energy due to s-wave constraint) then we can ask what happens if  $f(p)$  is truncated.

In the s-wave limit I need to write  $K$  as a function of  $f(p)$  (should do this in the appendix proof and reference in body). Given the form of the loss rate constant  $K$ , our problem reduces to determining the form of  $f(p)$  when  $\eta$  is finite.

Ok, so need to reference [20] to motivate usage of center of mass. Then use [51] Eq. 43 to reference the particular form

what is the throughline I want to make? Develop  $K_{in} \rightarrow$  recast in terms of  $P$  distribution  $\rightarrow$  show how we can replace the normal dist with a truncated dist  $\rightarrow$  explore the effects of that truncation

## Chapter 5

### Strongly coupled PAS of a weakly bound molecule

#### 5.1 Introduction

”Lorem ipsum dolor sit amet, consectetur adipiscing elit, sed do eiusmod tempor incididunt ut labore et dolore magna aliqua. Ut enim ad minim veniam, quis nostrud exercitation ullamco laboris nisi ut aliquip ex ea commodo consequat. Duis aute irure dolor in reprehenderit in voluptate velit esse cillum dolore eu fugiat nulla pariatur. Excepteur sint occaecat cupidatat non proident, sunt in culpa qui officia deserunt mollit anim id est laborum.”

#### 5.2 Experimental methods

”Lorem ipsum dolor sit amet, consectetur adipiscing elit, sed do eiusmod tempor incididunt ut labore et dolore magna aliqua. Ut enim ad minim veniam, quis nostrud exercitation ullamco laboris nisi ut aliquip ex ea commodo consequat. Duis aute irure dolor in reprehenderit in voluptate velit esse cillum dolore eu fugiat nulla pariatur. Excepteur sint occaecat cupidatat non proident, sunt in culpa qui officia deserunt mollit anim id est laborum.”

### 5.3 Three level model

”Lorem ipsum dolor sit amet, consectetur adipiscing elit, sed do eiusmod tempor incididunt ut labore et dolore magna aliqua. Ut enim ad minim veniam, quis nostrud exercitation ullamco laboris nisi ut aliquip ex ea commodo consequat. Duis aute irure dolor in reprehenderit in voluptate velit esse cillum dolore eu fugiat nulla pariatur. Excepteur sint occaecat cupidatat non proident, sunt in culpa qui officia deserunt mollit anim id est laborum.”

### 5.4 Resonance positions

”Lorem ipsum dolor sit amet, consectetur adipiscing elit, sed do eiusmod tempor incididunt ut labore et dolore magna aliqua. Ut enim ad minim veniam, quis nostrud exercitation ullamco laboris nisi ut aliquip ex ea commodo consequat. Duis aute irure dolor in reprehenderit in voluptate velit esse cillum dolore eu fugiat nulla pariatur. Excepteur sint occaecat cupidatat non proident, sunt in culpa qui officia deserunt mollit anim id est laborum.”

### 5.5 Lineshape

”Lorem ipsum dolor sit amet, consectetur adipiscing elit, sed do eiusmod tempor incididunt ut labore et dolore magna aliqua. Ut enim ad minim veniam, quis nostrud exercitation ullamco laboris nisi ut aliquip ex ea commodo consequat. Duis aute irure dolor in reprehenderit in voluptate velit esse cillum dolore eu fugiat nulla pariatur. Excepteur sint occaecat cupidatat non proident, sunt in culpa qui officia deserunt mollit anim id est laborum.”

## 5.6 Emergence of multi-photon Raman coupling

”Lorem ipsum dolor sit amet, consectetur adipiscing elit, sed do eiusmod tempor incididunt ut labore et dolore magna aliqua. Ut enim ad minim veniam, quis nostrud exercitation ullamco laboris nisi ut aliquip ex ea commodo consequat. Duis aute irure dolor in reprehenderit in voluptate velit esse cillum dolore eu fugiat nulla pariatur. Excepteur sint occaecat cupidatat non proident, sunt in culpa qui officia deserunt mollit anim id est laborum.”

## Chapter 6

### Progress towards studies of quantum magnetism

A straightforward extension of the work presented in this thesis would be to control interparticle spacing via an optical lattice. For these and additional experiments using quantum degenerate fermionic strontium we purchased and installed an optical lattice system. Our lattice is implemented using a Coherent Verdi V-18 which is shaped and propagated to our science chamber in free space. Fig shows the optical path for each arm of our cubic lattice.

Unfortunately, complications due to heating when loading the lattice has limited our success in this optical trap. I want to go over what we have been able to do so far with the lattice.

How did we characterize? Kaptiza-dirac extension  
 What convinced us we were having problems?  
 What are some ideas we could do in the lattice? Zeno faster cooling via stimulated raman potentially? (can I model this somehow?) repulsively bound molecules? use interaction control in lattice with the zeno thing

#### 6.1 532 nm optical lattice: installation and characterization

Optical lattices are formed by a standing wave of light which creates a defect free periodic potential. These traps are extremely versatile and have enabled the observa-

tion of the superfluid - Mott insulator transition [28], artificial gauge fields for neutral atoms [40], quantum microscopy with single-site resolution [? ], and investigations of quantum magnetism [? ? ]. They are among the most well-established techniques for controlling a quantum state and have proven to be great tools for exploring the connection between few- and many-body systems [? ].

### 6.1.1 Background

This section should cover band structure and refer to the types of wavefunctions that are possible. Perhaps through some stuff in here from the quantum magnetism proposal from the NSF

Until recently, experiments on the Neutral apparatus were confined to work with bulk gases in an optical dipole trap. While optical dipole traps are useful for efficient evaporation and thermalization of an ultracold gas, experiments with Feshbach molecules in ODTs suffer from a high rate of inelastic collisions. [37]. The association of these molecules in an optical lattice has been shown to slow these processes since atoms must tunnel from site to site and can be pinned in sufficiently deep potentials [64? ]. In order to gain a quantitative understanding of these processes we will briefly outline the relevant lattice physics for ultracold bosons in an optical lattice.

An optical lattice is created by counterpropagating two laser beams to form a standing wave pattern, which for two plane waves in one dimension results in a periodic potential given by

$$V(x) = V_{lat} \sin^2(k_L x) \tag{6.1}$$

where  $V_{lat}$  is the lattice depth determined by the polarizability of the atom for a

given trapping wavelength  $\lambda$  and laser intensity  $I$ , and  $k_L$  is the lattice wavevector . This potential can be readily extended to three dimensions using two additional pairs of counterpropagating laser beams along the  $y$  and  $z$  directions which results in a 3D cubic lattice. Depth of the trapping potential,  $V_{lat}$ , is controlled by varying the intensity of the lattice beams. Clever arrangements of laser beam propagation, in addition to phase and polarization control of the trapping fields, can extend these standing wave potentials to a number of non-trivial geometries such as triangular, checkerboard, and dimerized lattices [2].

Periodic potentials are powerful because they break the translational invariance of space which results in the formation of band structure and the opening of bandgaps or disallowed particle energies [6]. Because of the broken invariance,  $p$  is no longer a good quantum number and instead must be replaced by two new quantum numbers: the band index,  $n$ , and the quasimomentum,  $q$ . In one dimension, quasimomentum is specified by  $q = p - nG$ , where  $G = 2\pi/a$  is a reciprocal lattice vector, and  $a$  is the real space lattice constant. Fig. 6.1.1 shows how the band structure varies as the lattice depth is increased. Optical lattices have a lattice spacing  $a = \lambda/2$  which determines the reciprocal lattice vector  $G = 4\pi/\lambda = 2\hbar k_L$  and the natural energy scale  $E_r = \frac{\hbar^2 k_L^2}{2m}$  where  $m$  is the atomic mass and  $k_L$  is the lattice wavevector,  $k_L = 2\pi/\lambda$ . From the band structure, we see that the bandwidth of each band, given by  $\Delta E = E_{q=\hbar k_L} - E_{q=0}$ , decreases as the lattice depth is increased. In the limit that  $V_{lat} \rightarrow \infty$  the band structure reduces to a ladder of harmonic oscillator levels spaced by  $\hbar\omega_{ho} = \sqrt{4V_{lat}E_r}$ . Although, for moderately deep lattices,  $V_{lat} \gtrsim 5 E_r$ , this approximation is valid near the center of the Brillouin zone,  $q = 0$ , and provides a simple form to estimate the energy gaps between bands [? 32].

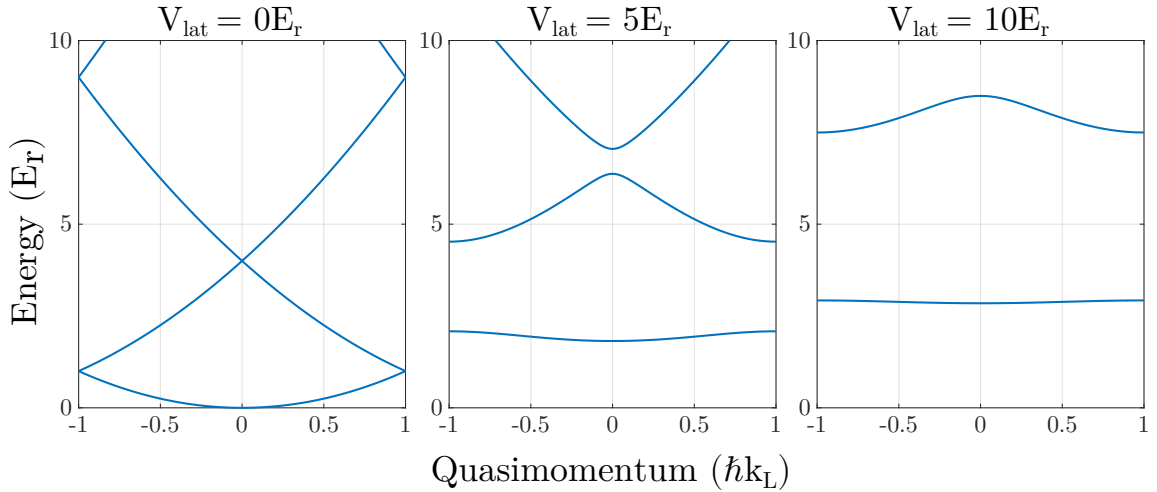


Figure 6.1 : 1D band structure as a function of lattice depth

One dimensional band structure for an optical lattice as the lattice depth is increased. The band energies are found by solving the Schrödinger equation using the Bloch functions of Eq. 6.2.

Solutions to the Schrödinger equation in a periodic potential are given by the Bloch functions [6]

$$\phi_q^{(n)}(x) = e^{iqx/\hbar} u_q^{(n)}(x) \quad (6.2)$$

These eigenstate wavefunctions are specified for a given quasimomentum  $q$ , and band index  $n$ . Their corresponding energy eigenvalues define the band structure of the lattice shown in Fig. 6.1.1. From Eq. 6.2 we see that the Bloch functions are the product of plane waves modulated by a function  $u_q^{(n)}(x)$ , which shares the periodicity of the underlying lattice potential [6]. For an optical lattice this modulating function can be expanded in a basis of plane waves through a Fourier decomposition of the

lattice potential in Eq. 1.1, which gives [2],

$$u_q^{(n)}(x) = \sum_l c_l^{(n,q)} e^{i2lk_L x} \quad (6.3)$$

Here  $c_l^{(n,q)}$  are the coefficients for each plane wave in the basis expansion that are found by diagonalizing the lattice Hamiltonian [2].

Often, we are interested in the dynamics of particles on a particular lattice site, but since Bloch functions are delocalized over the entire lattice, it is useful to instead use the Wannier functions. These functions provide an orthogonal and normalized set of wavefunctions that are maximally localized to a specific lattice site. The Wannier function for a localized particle in the  $n^{th}$  band of a lattice site located at position  $x_i$  is given by [32]

$$w_n(x - x_i) = \mathcal{N}^{-1/2} \sum_q e^{iqx_i/\hbar} \phi_q^{(n)}(x) \quad (6.4)$$

where  $\mathcal{N}$  is a normalization constant and  $\phi_q^{(n)}(x)$  are the Bloch functions of Eq. 6.2. This localized description of particles allows us to calculate important physical quantities which govern dynamical properties of the lattice such as the tunneling rate,  $J/\hbar$ , and on-site interaction energy,  $U$ . As  $V_{lat} \rightarrow \infty$ , the Wannier functions approach the eigenfunctions of the harmonic oscillator, which allows us to estimate the spatial extent of an atomic wavefunction by  $a_{ho} = \sqrt{\frac{\hbar}{m\omega_{ho}}}$  [32].

When bosons are confined to the lowest energy band of a lattice, a particularly simple model known as the Bose-Hubbard Hamiltonian is used to describe the lattice system [? ].

$$H_{BH} = -J \sum_{\langle i,j \rangle} (\hat{b}_i^\dagger \hat{b}_j + \hat{b}_j^\dagger \hat{b}_i) + \frac{U}{2} \sum_i \hat{n}_i(\hat{n}_i - 1) \quad (6.5)$$

Where  $\langle i,j \rangle$  denotes a sum over nearest-neighbors. This model is the simplest example of a non-trivial interacting many-body system for dynamics in a lattice. The first

term describes hopping of bosons from site to site at a rate  $J/\hbar$ . The second term describes an interaction energy which is related to the s-wave contact interaction term,  $g = 4\pi\hbar^2 a_s/m$ , where  $a_s$ , is the s-wave scattering length of the particles.  $J$  and  $U$  can be calculated directly using the Wannier functions of Eq. 6.4 and are given by

[32]

$$\begin{aligned} J_{ij} &= - \int d^3x w_0(x - x_i) \left( \frac{p^2}{2m} + V(x) \right) w_0(x - x_j) \\ U &= \frac{4\pi\hbar^2 a_s}{m} \int d^3x |w_0(x - x_i)|^4 \end{aligned} \quad (6.6)$$

Using Eq. 6.6 we have calculated the expected tunneling rates and interaction energies for atomic strontium and plot the results in Fig. 6.1.1 for homonuclear samples of strontium as a function of lattice depth. This single band calculation is valid under the assumption that the interaction energy of a site is smaller than the bandgap between the  $n = 0$  and 1 bands, namely  $UN \lesssim \hbar\omega_{ho}$  where  $N$  is the mean number of particles per site and  $\hbar\omega_{ho}$  is the approximate energy spacing between bands [55].

Alternatively, Eq. 6.6 can be simplified through considering appropriate limits to the Bose-Hubbard model. In the limit that  $U \rightarrow 0$ , the Bose-Hubbard model becomes exactly solvable and the energy of the  $n = 0$  band is given by  $E_q^{(0)} = -2J \cos(qa)$  [32]. Thus, the tunneling rate,  $J$ , can be related to the bandwidth of the lowest band as expressed in Eq. 6.7. Under a separate limit,  $V_{lat} \rightarrow \infty$ , then the tunneling rate goes to zero and the localized wavefunctions can be approximated by a Gaussian wavefunction which yields the form for the on-site interaction  $U$  given in Eq. 6.7 [55].

$$\begin{aligned} J &= \frac{E_{q=\hbar k_L} - E_{q=0}}{4} \\ U &= \frac{\hbar a_s}{\sqrt{2\pi}} \frac{\bar{\omega}_{ho}}{\bar{a}_{ho}} \end{aligned} \quad (6.7)$$

Here  $\bar{a}_{ho}$  and  $\bar{\omega}_{ho}$  are the geometric means of the one-dimensional harmonic oscillator

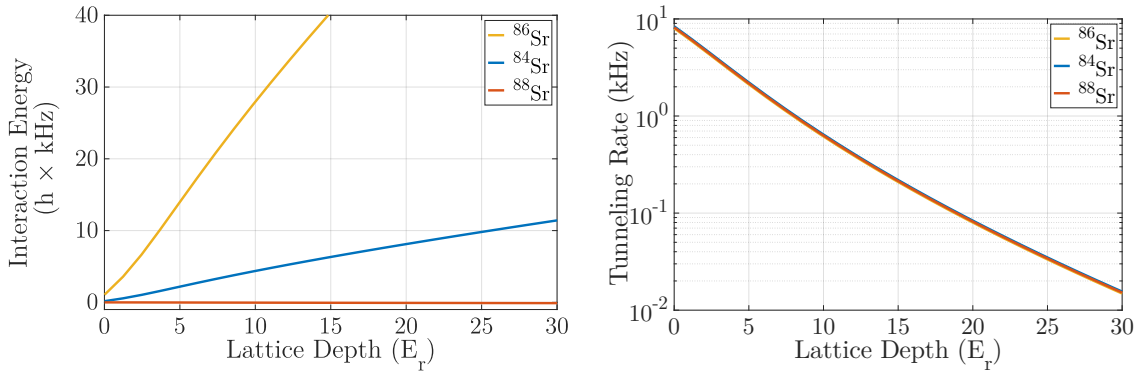


Figure 6.2 : Calculated interaction energies and tunneling rates for each isotope of strontium

The interaction energy shows a large variation because of its dependence on the s-wave scattering length. However, the tunneling rate is approximately the same for all isotopes since the change in mass is negligible between isotopes.

length and frequency given previously.

Competition between  $J$  and  $U$  results in a phase transition known as the superfluid - Mott insulator transition [25, 28]. When  $J/U \gg 1$  atoms are free to delocalize over the lattice and the many-body ground state is a superfluid. In the opposite limit that  $J/U \ll 1$ , particle fluctuations between sites are no longer energetically accessible and the system transitions into an interaction induced insulating state known as a Mott insulator. This state is characterized by fixed particle number per site and in a 3D cubic lattice near unit filling, this phase transition occurs at  $J/U \approx 35$  which, for <sup>84</sup>Sr, corresponds to a lattice depth of  $V_{lat} \approx 13E_r$  [25].

The tunability of an optical lattice potential is useful for studying feshbach molecules. By controlling the lattice depth and/or atomic density, we can efficiently create molecules when there are two or more atoms per site. Using the volume of a unit cell

we can estimate the densities needed to reach average on-site occupancy of 2, which is ideal for forming isolated molecules. For a lattice wavelength of 532 nm in a simple cubic configuration, the volume for each lattice site is  $1.9 \times 10^{-14} \text{ cm}^3$ , so we must achieve densities on the order of  $4 \times 10^{14} \text{ cm}^{-3}$  to expect significant conversion. A more detailed approach to estimate our conversion efficiency would entail: 1) calculating the variation in chemical potential across the trap due to the inhomogeneous confinement of the trapping potential, 2) finding the average particle number per site as a function of  $J/U$  to estimate the distribution of  $\mu/U$  on the superfluid - Mott insulating phase diagram [25], and 3) integrating the density distribution from the center of the trap to a limiting value of  $\mu/U$ , where the local density is too dilute for efficient molecule conversion. Though such a calculation is beyond the scope of this proposal, it is worth noting that the shell structure found near the Mott insulating regime inhibits complete molecular conversion of the atomic gas. Therefore, molecules are accompanied by a large number of unconverted remnant atoms. Previous investigators have shown that it is beneficial to clear non-molecule atoms out of the lattice through a sequence of light and/or microwave pulses. Such a cleaning sequence will need to be investigated in our system since tunneling from single atoms can lead to a reduction of the molecular lifetime [37, 64].

### 6.1.2 Setup

This section should cover all the specifics regarding the lattice

Our optical lattice operates at  $\lambda = 532 \text{ nm}$  and is derived from a Coherent Verdi V-18 single mode laser which is sent through separate AOMs for intensity control of each arm before propagating in free space to the atoms. The horizontal arms of the

lattice ( $x$  and  $y$ ) have  $1/e^2$  waists of  $200\text{ }\mu\text{m} \times 200\text{ }\mu\text{m}$  and their polarization is linear and aligned along the  $z$  direction, parallel to gravity. The vertically propagating beam has a  $1/e^2$  waist size of  $300\text{ }\mu\text{m} \times 300\text{ }\mu\text{m}$  and polarization aligned orthogonal to the polarization of the horizontal beams. With this configuration we have measured a maximum depth of  $9E_r$  in an isotropic lattice. As this is our first implementation of an optical lattice, we have spent a significant amount of time characterizing our system as detailed below.

### 6.1.3 Measurement and results

What are all the types of experiments we did in the lattice?

Cover sideband cooling and Bloch oscillations Results, look into why its not necessarily so easy from end of red MOT, thoughts on how it could become useful

#### 6.1.3.1 Kaptiza-Dirac Scattering

Brief intro to theory and some plots showing fits.

Fig. 6.1.3.1 shows a typical Kapitza-Dirac oscillation pattern which we use to maximize beam overlap near the atoms and calibrate our achievable lattice depths. Kapitza-Dirac is useful as an alignment tool since measurement of the population oscillation frequency can be highly accurate and directly relates to the bandgap energy in the lattice, shown in Fig. 6.1.1.

Kapitza-Dirac diffraction can be viewed as a diabatic projection from an initial eigenstate to a new set of eigenstates which results in an oscillation of the wavefunctions probability amplitudes over the new eigenstates of the system [23]. As was discussed in Sec. 6.1, the free space eigenstates are not the eigenstates of the lattice

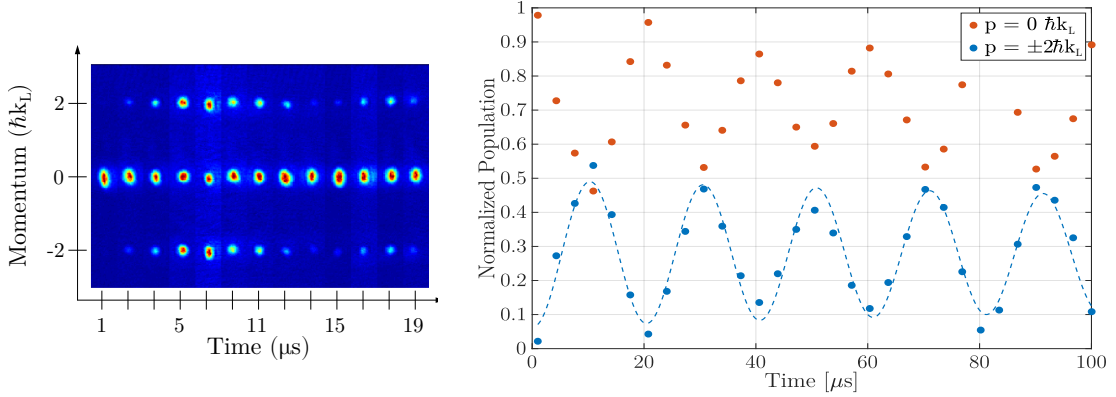


Figure 6.3 : Evolution of plane wave population using Kapitza-Dirac

Left: Time of flight slices for several realizations of Kapitza-Dirac with varying hold time in the lattice. Right: Normalized population from fits of time-of-flight images. Oscillations are fit with a decaying sinusoidal and the best-fit frequency is used to determine the lattice depth.

Hamiltonian. Thus a pure  $p = 0$  plane wave,  $|\phi_{p=0}\rangle$ , suddenly loaded into an optical lattice can be written as a superposition of the Bloch states given by Eq. 6.2, here denoted by  $|n, q\rangle$ .

$$|\Psi(t=0)\rangle = \sum_{n=0}^{\infty} |n, q\rangle \langle n, q| \phi_{p=0} \rangle \quad (6.8)$$

The time evolution of this state is then given by

$$|\Psi(t)\rangle = \sum_{n=0}^{\infty} |n, q\rangle \langle n, q| \phi_{p=0} \rangle \exp\left(\frac{-iE_n(q)t}{\hbar}\right) \quad (6.9)$$

where  $E_n(q)$  is the energy of the Bloch state at a specified  $q$  and  $n$  shown in Fig. 6.1.1. The exponential factor of Eq. 6.9 introduces oscillations among Bloch states and after a second diabatic projection back to the plane wave basis, we can relate evolution of plane wave population to the bandgap energy. From this analysis we find that

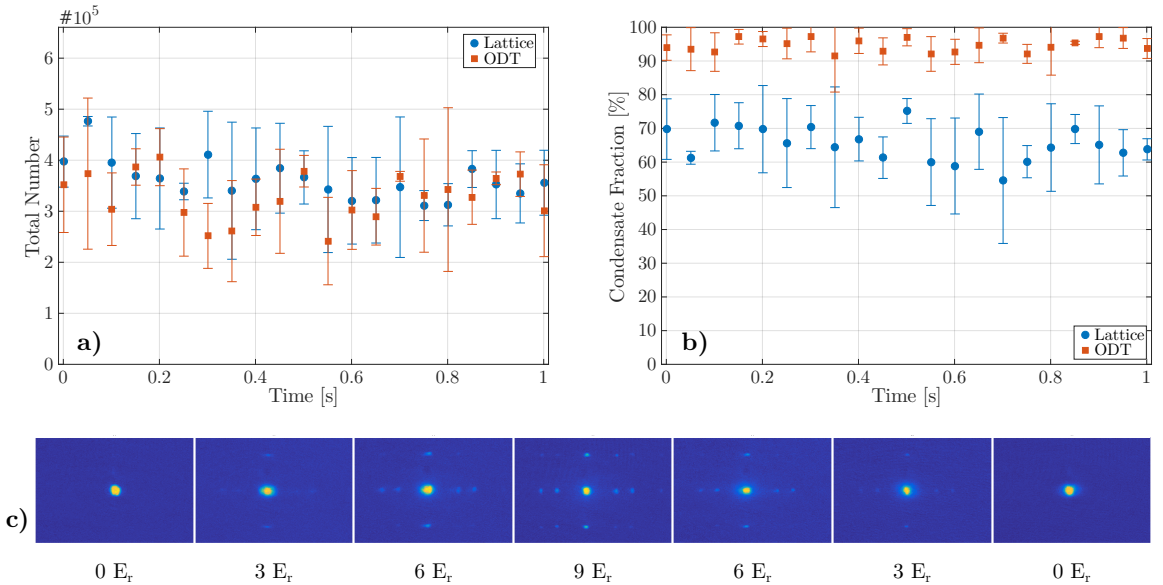


Figure 6.4 : Evolution of condensate fraction over time after adiabatically ramping on the lattice to  $9 E_r$ . a,b) Comparison of total number and condensate fraction for a sample held in the optical dipole trap (red squares) or in a deep lattice (blue circles). c) Time of flight images after ramping on the lattice and diabatically projecting back to plane wave states.

for relatively weak lattices,  $V_{lat} \lesssim 10E_r$ , the plane wave population will vary as  $\omega_{osc} = (E_2 - E_0)/\hbar$ . Where  $E_i$  is the band energy of the  $i^{th}$  band with  $q = 0$  as is the case when performing Kapitza-Dirac with a Bose-Einstein condensate.

### 6.1.3.2 Heating of a quantum degenerate gas

Creation of a Mott insulator and the results showing unacceptable heating rates

While Kapitza-Dirac diffraction is useful as a characterization tool, we typically wish to maintain equilibrium when loading condensates into the lattice. Thus slowly ramping up the lattice laser intensity will adiabatically transform a plane wave ground state into the ground Bloch state of the lattice [56]. Strictly speaking, in order to adiabatically connect the free space eigenstates and the lattice eigenstates, the

lattice must be turned on infinitely slowly due to the infinitesimal bandgaps which open near the band edges. Although near the band center,  $q = 0$ , the adiabaticity requirement relaxes to  $dV_{lat}/dt \ll 16E_r^2/\hbar$ , [23] which for strontium in a 532 nm lattice is  $\approx 5\ \mu\text{s}/E_r$ . However, in practice we find that our condensate fraction is reduced during fast ramps into the lattice. Instead, we exponentially ramp on the lattice over 100 ms which reduces heating caused by the ramp. As shown in Fig. 6.1.3.1, we observe a large condensate fraction after similarly ramping the lattice back down. Additionally, by holding in a deep lattice after an adiabatic ramp, we can measure the effects of off-resonant scatter of lattice photons as a reduction of atom population over time. For our red detuned optical lattice we expect the off-resonant scattering rate to be well approximated by a simple two level approach. In this model, the effective scattering rate is given by [32]

$$\Gamma_{eff} \approx \frac{\Gamma V_{lat}}{\hbar \delta_{lat}} \quad (6.10)$$

where  $\Gamma$  is linewidth of the dipole transition between the two states,  $V_{lat}$  is the lattice depth, and  $\delta_{lat}$  is the detuning of the optical lattice from the two level transition frequency. In strontium, the  ${}^1S_0 \rightarrow {}^1P_1$  transition strongly dominates the polarizability of the ground state and therefore can be used to estimate the effective off-resonant scattering rate. For this transition  $\Gamma = 2\pi \times 30.5\ \text{MHz}$  and a 532 nm lattice is detuned by  $\delta_{lat} \approx 2\pi \times 87\ \text{THz}$ . With a lattice depth of  $V_{lat} = 10\ E_r$  we expect a scattering rate of  $\Gamma_{eff} \approx 2 \times 10^{-1}\ \text{s}^{-1}$ , which is negligible for the timescales of our proposed experiments. From Fig. 6.1.3.1, we see that there is not an appreciable loss of atoms over a one second timescale, supporting our estimate that off-resonant scattering is unimportant on these timescales.

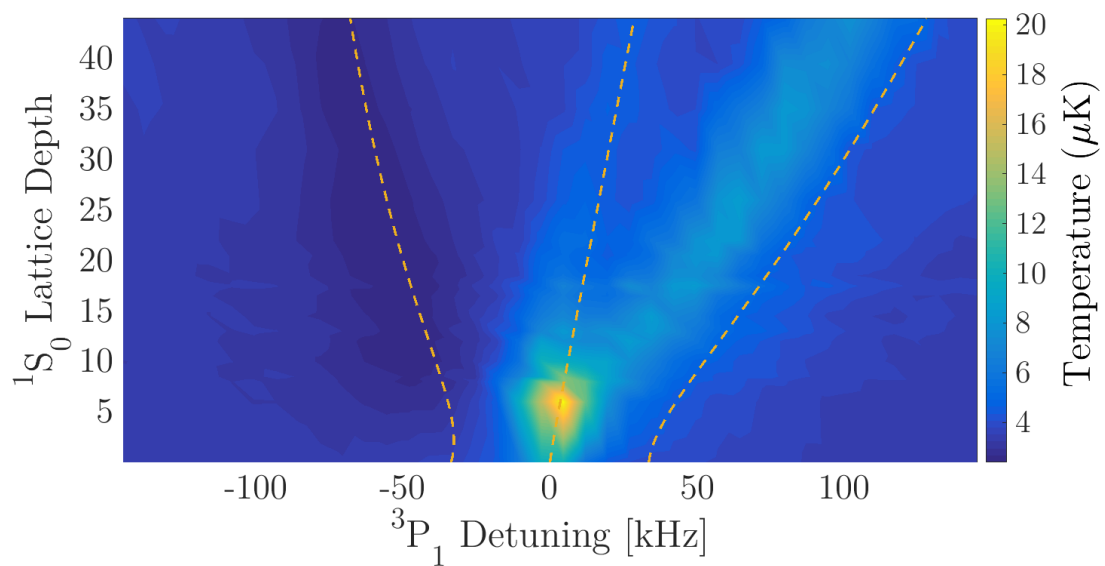


Figure 6.5 : Observation of driven sideband transitions

Driven sidebands in a 1D lattice as a function of lattice depth using an ultracold gas with an initial temperature of  $\approx 200$  nK. Dashed lines are the expected band positions using a 1D model of the lattice as shown in Fig. 6.1.1.

## 6.2 Spin manipulation of $^{87}\text{Sr}$

Here is where I need to introduce and characterize the LCR

Averaging images together (how to use this code specifically)

## 6.3 Search for narrowline PA molecules using various spin mixtures

”Lorem ipsum dolor sit amet, consectetur adipiscing elit, sed do eiusmod tempor incididunt ut labore et dolore magna aliqua. Ut enim ad minim veniam, quis nostrud exercitation ullamco laboris nisi ut aliquip ex ea commodo consequat. Duis aute irure dolor in reprehenderit in voluptate velit esse cillum dolore eu fugiat nulla pariatur. Excepteur sint occaecat cupidatat non proident, sunt in culpa qui officia deserunt mollit anim id est laborum.”

## Chapter 7

### Conclusion

We have measured the binding energy of the least-bound vibrational level of the ground electronic state of the  $^{86}\text{Sr}_2$  molecule with two-photon photoassociative spectroscopy. Using the universal prediction for the binding energy of a halo state including corrections derived for a van der Waals potential [Eq. (4.15)] [30, 26, 27], we extract an improved value of the *s*-wave scattering length.

We also characterized the AC Stark shift of the halo-state binding energy due to light near resonant with the single-photon photoassociation transition. A model only accounting for a single excited-state channel [? ] cannot explain the observed frequency dependence of the AC Stark shift, which can be attributed to the proximity of other excited states.

Large AC Stark shifts of the halo state point to the possibility of optically tuning the  $^{86}\text{Sr}$  scattering length, similar to recent demonstrations of optical tuning of magnetic Feshbach resonances [4, 21]. This is attractive because ground-state strontium lacks magnetic Feshbach resonances. With improved measurement of the photoassociation resonance frequency and its dependence on background atom density, perhaps combined with optical manipulation of the scattering length, it may also be possible to study the landscape of Efimov trimers associated with this naturally occurring scattering resonance. This work also points to the need for improved theory, such as an improved calculation of the Sr ground-state molecular potential and  $C_6$  coefficient,

which could be compared with this high-accuracy measurement of the halo binding energy.

The work presented in this proposal is a natural extension of previous work done in our lab using an optical Feshbach resonance and one color photoassociation to manipulate the quantum state of a Bose-Einstein condensate. The creation and characterization of a novel type of Feshbach molecule is of fundamental interest to complete the analogy between optical and magnetic Feshbach resonances as well as to test the mechanism of Feshbach molecule stability in the presence of closed channel decay. This experiment provides a practical first demonstration of an optical lattice on our apparatus, which can be readily extended to a number of experiments such as out of equilibrium unitarity quenches [43], strongly interacting Bose gases stabilized by the quantum zeno effect [? 72, 67, 60], and the observation of exotic spin phases [7? , 15]. Moreover, additional insight might also be drawn from revisiting OFR and photoassociation in an optical lattice and employing new measurement techniques in the lattice [61]. These and future experiments will take advantage of the variety of interactions and narrow intercombination transitions available in strontium as well as the control and selectivity afforded through an optical lattice.

## Bibliography

- [1] Aman, J. A., J. C. Hill, R. Ding, K. R. A. Hazzard, T. C. Killian, and W. Y. Kon, 2018, Physical Review A **98**(5), 053441, ISSN 2469-9926, URL <https://link.aps.org/doi/10.1103/PhysRevA.98.053441>.
- [2] Anker, T., 2005, *Ultracold quantum gases in one-dimensional optical lattice potentials*, Ph.D. thesis, Ludwig-Maximilians-Universität München, URL [https://edoc.ub.uni-muenchen.de/968/1/Greiner{\\_}Markus.pdf](https://edoc.ub.uni-muenchen.de/968/1/Greiner{_}Markus.pdf).
- [3] Bartenstein, M., A. Altmeyer, S. Riedl, R. Geursen, S. Jochim, C. Chin, J. H. Denschlag, R. Grimm, A. Simoni, E. Tiesinga, C. J. Williams, and P. S. Julienne, 2005, Physical Review Letters **94**(10), 103201, ISSN 00319007.
- [4] Bauer, D. M., M. Lettner, C. Vo, G. Rempe, and S. Durr, 2009, Nature Physics **5**, 339.
- [5] Begun, V., and M. Gorenstein, 2007, Proceedings of Science **82**(4), 041602, ISSN 18248039, URL <http://link.aps.org/doi/10.1103/PhysRevA.82.041602>.
- [6] Bergman, D. J., and D. Stroud, 1992, *Solid state Physics* (Saunders College), ISBN 047141526X.
- [7] Beverland, M. E., G. Alagic, M. J. Martin, A. P. Koller, A. M. Rey, and A. V.

- Gorshkov, 2016, Physical Review A **93**(5), 051601, ISSN 24699934, URL <http://link.aps.org/doi/10.1103/PhysRevA.93.051601>.
- [8] Blatt, S., T. L. Nicholson, B. J. Bloom, J. R. Williams, J. W. Thomsen, P. S. Julienne, and J. Ye, 2011, Physical Review Letters **107**(7), 073202, ISSN 00319007, URL <http://link.aps.org/doi/10.1103/PhysRevLett.107.073202>.
- [9] Bohn, J. L., and P. S. Julienne, 1997, Physical Review A - Atomic, Molecular, and Optical Physics **56**(2), 1486, ISSN 10941622, URL <http://journals.aps.org/prl/abstract/10.1103/PhysRevA.56.1486>.
- [10] Borkowski, M., A. A. Buchachenko, R. Ciuryło, P. S. Julienne, H. Yamada, Y. Kikuchi, K. Takahashi, Y. Takasu, and Y. Takahashi, 2017, Physical Review A **96**, 63405, ISSN 24699934.
- [11] Borkowski, M., R. Ciuryło, P. S. Julienne, S. Tojo, K. Enomoto, and Y. Takahashi, 2009, Physical Review A - Atomic, Molecular, and Optical Physics **80**(1), 1, ISSN 10502947.
- [12] Braaten, E., and H. W. Hammer, 2006, Physics Reports **428**, 259, ISSN 03701573.
- [13] Braaten, E., and H.-W. Hammer, 2007, Annals of Physics **322**(1), 120, ISSN 00034916, URL <http://linkinghub.elsevier.com/retrieve/pii/S0003491606002387>.
- [14] Bradley, C. C., C. A. Sackett, J. J. Tollett, and R. G. Hulet, 1995, Physical

- Review Letters **75**(9), 1687, ISSN 00319007, URL <http://link.aps.org/doi/10.1103/PhysRevLett.75.1687>.
- [15] Chen, G., K. R. Hazzard, A. M. Rey, and M. Hermele, 2016, Physical Review A **93**(6), ISSN 24699934, URL <http://arxiv.org/abs/1501.04086>.
- [16] Chin, C., R. Grimm, P. Julienne, and E. Tiesinga, 2010, Reviews of Modern Physics **82**(2), 1225, URL <https://link.aps.org/doi/10.1103/RevModPhys.82.1225>.
- [17] Chin, C., and P. S. Julienne, 2005, Physical Review A - Atomic, Molecular, and Optical Physics **71**(1), 12713, ISSN 10502947.
- [18] Ciurylo, R., E. Tiesinga, and P. S. Julienne, 2006, Physical Review A **74**, 22710.
- [19] Ciurylo, R., E. Tiesinga, P. S. Julienne, R. Ciuryło, E. Tiesinga, P. S. Julienne, R. Ciurylo, E. Tiesinga, and P. S. Julienne, 2005, Physical Review A - Atomic, Molecular, and Optical Physics **71**(3), 030701, ISSN 10502947, URL <http://link.aps.org/doi/10.1103/PhysRevA.71.030701>.
- [20] Ciuryło, R., E. Tiesinga, S. Kotochigova, and P. S. Julienne, 2004, Physical Review A - Atomic, Molecular, and Optical Physics **70**(6), 062710, ISSN 10941622, URL <http://link.aps.org/doi/10.1103/PhysRevA.70.062710>.
- [21] Clark, L. W., L. C. Ha, C. Y. Xu, and C. Chin, 2015, Physical Review Letters **115**, 155301, ISSN 10797114.
- [22] Claussen, N. R., S. J. J. M. F. Kokkelmans, S. T. Thompson, E. A. Donley,

- E. Hodby, and C. E. Wieman, 2003, Physical Review A **67**(6), 60701, ISSN 1050-2947, URL <https://link.aps.org/doi/10.1103/PhysRevA.67.060701>.
- [23] Denschlag, J. H., J. Hecker Denschlag, J. E. Simsarian, H. Häffner, C. McKenzie, A. Browaeys, D. Cho, K. Helmerson, S. L. Rolston, and W. D. Phillips, 2002, Journal of Physics B: Atomic, Molecular and Optical Physics **35**(14), 3095, ISSN 09534075, URL <http://stacks.iop.org/0953-4075/35/i=14/a=307?key=crossref.143851fdbd4f795110e47d745ef41278c>.
- [24] Fatemi, F. K., K. M. Jones, and P. D. Lett, 2000, Physical Review Letters **85**(21), 4462, ISSN 00319007, URL <http://link.aps.org/doi/10.1103/PhysRevLett.85.4462>.
- [25] Fisher, M. P., P. B. Weichman, G. Grinstein, and D. S. Fisher, 1989, Physical Review B **40**(1), 546, ISSN 01631829, URL <http://link.aps.org/doi/10.1103/PhysRevB.40.546>.
- [26] Gao, B., 2001, Physical Review A - Atomic, Molecular, and Optical Physics **64**, 10701, ISSN 10941622.
- [27] Gao, B., 2004, Journal of Physics B: Atomic, Molecular and Optical Physics **37**(21), 4273, ISSN 0953-4075, URL <http://stacks.iop.org/0953-4075/37/i=21/a=004?key=crossref.2818e17c48ea9c152598f4de6d7b11ce>.
- [28] Greiner, M., O. Mandel, T. Rom, A. Altmeyer, A. Widera, T. W. Hänsch, and I. Bloch, 2003, Physica B: Condensed Matter **329-333**(6867), 11, ISSN 09214526, URL <http://www.nature.com/doifinder/10.1038/415039a>.

- [29] Greiner, M., C. A. Regal, and D. S. Jin, 2003, *Nature* **426**, 537.
- [30] Gribakin, G. F., and V. V. Flambaum, 1993, *Physical Review A* **48**(1), 546, ISSN 1050-2947, URL <http://link.aps.org/doi/10.1103/PhysRevA.48.546>.
- [31] Ido, T., Y. Isoya, and H. Katori, 2000, *Physical Review A - Atomic, Molecular, and Optical Physics* **61**(6), 4, ISSN 10941622, URL <http://link.aps.org/doi/10.1103/PhysRevA.61.061403>.
- [32] Jaksch, D., and P. Zoller, 2005, *Annals of Physics* **315**(1), 52, ISSN 00034916, URL <http://linkinghub.elsevier.com/retrieve/pii/S0003491604001782>.
- [33] Jensen, A. S., K. Riisager, D. V. Fedorov, and E. Garrido, 2004, *Reviews of Modern Physics* **76**(1), 215, ISSN 00346861, URL <https://journals.aps.org/rmp/pdf/10.1103/RevModPhys.76.215>.
- [34] Jochim, S., M. Bartenstein, A. Altmeyer, G. Hendl, S. Riedl, C. Chin, J. Hecker-Denschlag, and R. Grimm, 2003, *Science* **302**, 2101.
- [35] Jones, K. M., E. Tiesinga, P. D. Lett, and P. S. Julienne, 2006, *Reviews of Modern Physics* **78**(2), 483, ISSN 00346861, URL <http://link.aps.org/doi/10.1103/RevModPhys.78.483><http://journals.aps.org/rmp/abstract/10.1103/RevModPhys.78.483>.
- [36] Köhler, T., T. Gasenzer, and K. Burnett, 2003, *Physical Review A* **67**(1), 13601, ISSN 1050-2947, URL <http://link.aps.org/doi/10.1103/PhysRevA.67.013601>.

- [37] Köhler, T., K. Góral, and P. S. Julienne, 2006, *Reviews of Modern Physics* **78**(4), 1311, ISSN 00346861, URL <http://link.aps.org/doi/10.1103/RevModPhys.78.1311>.
- [38] Köhler, T., K. Góral, and P. S. Julienne, 2006, *Reviews of Modern Physics* **78**(4), 1311, URL <http://link.aps.org/abstract/RMP/v78/p1311>.
- [39] Lang, F., K. Winkler, C. Strauss, R. Grimm, and J. H. Denschlag, 2008, *Physical Review Letters* **101**(13), 133005, ISSN 00319007, URL <http://link.aps.org/doi/10.1103/PhysRevLett.101.133005>.
- [40] Lin, Y. J., K. Jiménez-García, and I. B. Spielman, 2011, *Nature* **471**(7336), 83, ISSN 00280836, URL <http://www.nature.com/doifinder/10.1038/nature09887>.
- [41] Loftus, T. H., T. Ido, M. M. Boyd, A. D. Ludlow, and J. Ye, 2004, *Physical Review A - Atomic, Molecular, and Optical Physics* **70**(6), 063413, ISSN 10502947, URL <http://link.aps.org/doi/10.1103/PhysRevA.70.063413>.
- [42] Luo, F., G. C. Mcbane, G. Kim, C. F. Giese, and W. R. Gentry, 1993, *The Journal of Chemical Physics The Journal of Chemical Physics The Journal of Chemical Physics* **98**1(10), URL <http://dx.doi.org/10.1063/1.464079http://aip.scitation.org/toc/jcp/98/4>.
- [43] Makotyn, P., C. E. Klauss, D. L. Goldberger, E. A. Cornell, and D. S. Jin, 2014, *Nature Physics* **10**(2), 116, ISSN 17452473, URL <http://www.nature.com/doifinder/10.1038/nphys2850>.

- [44] Méndez-Visag, C., 2014, Revista Peruana de Medicina Experimental y Salud Publica **31**(4), 725, ISSN 17264642, URL <http://www.ncbi.nlm.nih.gov/pubmed/10481000>.
- [45] Mestrom, P. M. A., J. Wang, C. H. Greene, and J. P. D'Incao, 2017, Physical Review A **95**, 32707, ISSN 24699934.
- [46] Mickelson, P. G., Y. N. Martinez De Escobar, M. Yan, B. J. Desalvo, and T. C. Killian, 2010, Physical Review A - Atomic, Molecular, and Optical Physics **81**(5), 5, ISSN 10502947, URL <http://link.aps.org/doi/10.1103/PhysRevA.81.051601>.
- [47] Moritz, H., T. Stoferle, K. Gunter, M. Kohl, and T. Esslinger, 2005, Physical Review Letters **94**, 210401.
- [48] Mukaiyama, T., H. Katori, T. Ido, Y. Li, and M. Kuwata-Gonokami, 2003, Physical Review Letters **90**(11), 4, ISSN 10797114, URL <http://link.aps.org/doi/10.1103/PhysRevLett.90.113002>.
- [49] Nagel, S. B., C. E. Simien, S. Laha, P. Gupta, V. S. Ashoka, and T. C. Killian, 2003, Physical Review A - Atomic, Molecular, and Optical Physics **67**(1), 4, ISSN 10941622, URL <http://link.aps.org/doi/10.1103/PhysRevA.67.011401>.
- [50] Naidon, P., and S. Endo, 2017, Reports on Progress in Physics **80**, 56001, ISSN 00344885.
- [51] Nicholson, T. L., S. Blatt, B. J. Bloom, J. R. Williams, J. W. Thomsen, J. Ye, and P. S. Julienne, 2015, Physical Review A - Atomic, Molecular, and Optical

- Physics **92**(2), 022709, ISSN 10941622, URL <http://journals.aps.org/prabSTRACT/10.1103/PhysRevA.92.022709>.
- [52] Pachomow, E., V. P. Dahlke, E. Tiemann, F. Riehle, and U. Sterr, 2017, Physical Review A **95**(4), 043422, ISSN 24699934, URL <http://arxiv.org/abs/1702.00710><http://link.aps.org/doi/10.1103/PhysRevA.95.043422>.
- [53] Ratcliff, L. B., J. L. Fish, and D. D. Konowalow, 1987, J. Mol. Spectrosc. **122**, 293.
- [54] Regal, C. A., C. Ticknor, J. L. Bohn, and D. S. Jin, 2003, Nature **424**, 47.
- [55] Rey, A. M., 2004, *Ultracold Bosonic Atoms in Optical Lattices*, Ph.D. thesis, University of Maryland, URL <http://hdl.handle.net/1903/1802>.
- [56] Sakurai, J. J., 1994, *Modern Quantum Mechanics, Supplement I* (Pearson), ISBN 978, URL [http://www.amazon.com/gp/product/0805382917/ref=pd\\_lpo\\_sbs\\_dp\\_ss\\_1?pf\\_rd\\_p=1535523722&pf\\_rd\\_s=lpo-top-stripe-1&pf\\_rd\\_t=201&pf\\_rd\\_i=0201539292&pf\\_rd\\_m=ATVPDKIKX0DER&pf\\_rd\\_r=0F9ZVFXMSJ1718HT9VN2](http://www.amazon.com/gp/product/0805382917/ref=pd_lpo_sbs_dp_ss_1?pf_rd_p=1535523722&pf_rd_s=lpo-top-stripe-1&pf_rd_t=201&pf_rd_i=0201539292&pf_rd_m=ATVPDKIKX0DER&pf_rd_r=0F9ZVFXMSJ1718HT9VN2).
- [57] Scholikopf, W., and J. P. Toennies, 1994, Science **266**(5189), 1345, URL <http://science.sciencemag.org/content/sci/266/5189/1345.full.pdf>.
- [58] Stein, A., H. Knöckel, and E. Tiemann, 2010, Eur. Phys. J. D **57**, 171.
- [59] Stenholm, S., 1988, *Laser cooling and trapping*, volume 9 of *Graduate Texts in Contemporary Physics* (Springer New York, New York, NY), ISBN

978-0-387-98728-6, NIHMS150003, URL <http://link.springer.com/10.1007/978-1-4612-1470-0>.

- [60] Syassen, N., D. M. Bauer, M. Lettner, T. Volz, D. Dietze, J. J. García-Ripoll, J. I. Cirac, G. Rempe, and S. Dürr, 2008, Science **320**(5881), 1329, ISSN 00368075, URL <http://www.ncbi.nlm.nih.gov/pubmed/18535241>.
- [61] Taie, S., S. Watanabe, T. Ichinose, and Y. Takahashi, 2016, Physical Review Letters **116**(4), 043202, ISSN 10797114, URL <http://link.aps.org/doi/10.1103/PhysRevLett.116.043202>.
- [62] Tey, M. K., S. Stellmer, R. Grimm, and F. Schreck, 2010, Physical Review A - Atomic, Molecular, and Optical Physics **82**(1), 011608, ISSN 10502947, URL <http://journals.aps.org/prl/abstract/10.1103/PhysRevA.82.011608>  
<http://link.aps.org/doi/10.1103/PhysRevA.82.011608>.
- [63] Thalhammer, G., M. Theis, K. Winkler, R. Grimm, and J. H. Denschlag, 2005, Physical Review A - Atomic, Molecular, and Optical Physics **71**(3), 033403, ISSN 10502947, URL <http://link.aps.org/doi/10.1103/PhysRevA.71.033403>.
- [64] Thalhammer, G., K. Winkler, F. Lang, S. Schmid, R. Grimm, and J. H. Denschlag, 2006, Physical Review Letters **96**(5), 050402, ISSN 10797114, URL <http://link.aps.org/doi/10.1103/PhysRevLett.96.050402>.
- [65] Theis, M., G. Thalhammer, K. Winkler, M. Hellwig, G. Ruff, R. Grimm, and J. H. Denschlag, 2004, Physical Review Letters **93**(12), 123001, ISSN 0031-9007, URL <http://link.aps.org/doi/10.1103/PhysRevLett.93.123001>.

- [66] Wang, J., J. P. D’Incao, B. D. Esry, and C. H. Greene, 2012, Phys. Rev. Lett. **108**, 263001.
- [67] Wong, L. S., B. W. N. Voon, S. C. Teo, and A. Balakrishnan, 2016, Ecology, Environment and Conservation **22**(3), 1107, ISSN 0971765X, URL <http://link.aps.org/doi/10.1103/PhysRevLett.102.040402>.
- [68] Wynar, R., R. S. Freeland, D. J. Han, C. Ryu, and D. J. Heinzen, 2000, Science **287**, 1016.
- [69] Yamazaki, R., S. Taie, S. Sugawa, and Y. Takahashi, 2010, Physical Review Letters **105**(5), 050405, ISSN 00319007, URL <https://link.aps.org/doi/10.1103/PhysRevLett.105.050405>.
- [70] Yan, M., B. J. DeSalvo, B. Ramachandhran, H. Pu, and T. C. Killian, 2013, Physical Review Letters **110**(12), 123201, ISSN 0031-9007, URL <http://link.aps.org/doi/10.1103/PhysRevLett.110.123201><https://arxiv.org/abs/0906.1837>.
- [71] Zhang, X., M. Bishof, S. L. Bromley, C. V. Kraus, M. S. Safronova, P. Zoller, A. M. Rey, and J. Ye, 2014, Science **345**(6203), 1467, ISSN 0036-8075, URL <http://www.sciencemag.org/cgi/doi/10.1126/science.1254978><http://arxiv.org/abs/1403.2964>.
- [72] Zhu, B., B. Gadway, M. Foss-Feig, J. Schachenmayer, M. L. Wall, K. R. Hazzard, B. Yan, S. A. Moses, J. P. Covey, D. S. Jin, J. Ye, M. Holland, *et al.*, 2014, Physical Review Letters **112**(7), 070404, ISSN 00319007, URL <http://link.aps.org/doi/10.1103/PhysRevLett.112.070404>.

## Appendices

## Appendix A

### Two-particle momentum probability distribution

#### A.1 Standard form

Typical derivation of relative momentum probability distribution function

We begin by considering the single particle momentum probability distribution function (gotten how)? Single particle momentum probability distribution

$$f^1(\mathbf{p}) = \left( \frac{1}{2\pi k_B T} \right)^{3/2} e^{\left( \frac{-p^2}{2mk_B T} \right)} \quad (\text{A.1})$$

Extension of this simple Boltzmann equation into the two-particle regime is complicated due to dependence of each particle on the others. If however, we make the assumption that particle collisions are rapid (on some timescale) we can approximate the two particle momentum distribution as the product of two single particle functions. This is known as the molecular chaos assumption and is important for what???

The two particle distribution for a homogeneous system is then

$$\begin{aligned} f^2(\mathbf{p}_1, \mathbf{p}_2) &= f^1(\mathbf{p}_1)f^1(\mathbf{p}_2) \\ &= \left( \frac{1}{2\pi m k_B T} \right)^3 \exp \left( \frac{-(p_1^2 + p_2^2)}{2mk_B T} \right) \end{aligned} \quad (\text{A.2})$$

Next, we'd like to consider a center-of-mass frame for the distribution. So we'll define

we define the relative and center-of-mass momenta of the two particles by defining

$$\mathbf{P}_c = \mathbf{p}_1 + \mathbf{p}_2 \quad M = m_1 + m_2 = 2m$$

$$\mathbf{p}_r = \frac{\mathbf{p}_1 - \mathbf{p}_2}{2} \quad \mu = \frac{m_1 m_2}{m_1 + m_2} = \frac{m}{2}$$

from these equations we can use conservation of energy to determine the quadrature sum of the two momenta

$$\begin{aligned} \frac{p_1^2}{2m} + \frac{p_2^2}{2m} &= \frac{P_c^2}{2M} + \frac{p_r^2}{2\mu} \\ p_1^2 + p_2^2 &= \frac{P_c^2}{2} + 2p_r^2 \end{aligned}$$

thus the momentum probability distribution take the form

$$f^2(\mathbf{P}_c, \mathbf{p}_r) = \left( \frac{1}{2\pi M k_B T} \right)^{3/2} \left( \frac{1}{2\pi \mu k_B T} \right)^{3/2} \exp \left( \frac{-P_c^2}{2M k_B T} \right) \exp \left( \frac{-p_r^2}{2\mu k_B T} \right) \quad (\text{A.3})$$

## A.2 Truncated form

Here I will derive, motivate, and test limiting cases. Plots showing the effects of truncation will be in the main text

Two particle distribution (for correcting notation, use C and R when denoting CoM and Rel)

$$\begin{aligned} f_{\mathbf{r},trunc}^2(\mathbf{p}_1, \mathbf{p}_2) &= A^2 \left( \frac{1}{2\pi m k_B T} \right)^3 \exp \left( \frac{-(p_1^2 + p_2^2)}{2m k_B T} \right) \\ &\times \Theta \left( \epsilon_{max} - U(\mathbf{r}) - \frac{p_1^2}{2m} \right) \Theta \left( \epsilon_{max} - U(\mathbf{r}) - \frac{p_2^2}{2m} \right) \end{aligned} \quad (\text{A.4})$$

We have introduced a normalization constant  $A$  here to ensure the that integration over the truncated probability distribution remains equal to one.

The meaning of  $f_r$  is such that  $f$  should be evaluated at each point in space. Furthermore since the atoms are held in a trapping potential, each point in space has a local trap depth relative to the lip at the top of the trap [need some figure to try and denote this]

Want distribution of relative momenta so integrate out center of mass. Going to drop the two and trunc for now

$$\begin{aligned}\tilde{f}_r(\mathbf{p}_{rel}) &= \int d^3\mathbf{P}_c f_r(\mathbf{p}_1, \mathbf{p}_2) \\ &= \left(\frac{1}{2\pi Mk_B T}\right)^{3/2} \left(\frac{1}{2\pi\mu k_B T}\right)^{3/2} A^2 \int d^3\mathbf{P}_c e^{\left(\frac{-P_c^2}{2Mk_B T}\right)} e^{\left(\frac{-p_r^2}{2\mu k_B T}\right)} \\ &\times \Theta\left(\epsilon_{max} - U(\mathbf{r}) - \frac{P_c^2}{8m} - \frac{p^2}{2m} - \frac{\mathbf{P}_c \cdot \mathbf{p}}{2m}\right) \Theta\left(\epsilon_{max} - U(\mathbf{r}) - \frac{P_c^2}{8m} - \frac{p^2}{2m} + \frac{\mathbf{P}_c \cdot \mathbf{p}}{2m}\right)\end{aligned}\quad (\text{A.5})$$

Spherically symmetrix collisions so can integrate by transforming into spherical coordinates with the radius aligned along the interatomic axis

$$\begin{aligned}\tilde{f}_r(\mathbf{p}) &= \left(\frac{1}{2\pi Mk_B T}\right)^{3/2} \left(\frac{1}{2\pi\mu k_B T}\right)^{3/2} e^{\left(\frac{-p_r^2}{2\mu k_B T}\right)} A^2 \int_0^\pi \sin\theta d\theta \int_0^{2\pi} d\phi \int_0^\infty dP_c P_c^2 e^{\left(\frac{-P_c^2}{2Mk_B T}\right)} \\ &\times \Theta\left(\epsilon_{max} - U(\mathbf{r}) - \frac{P_c^2}{8m} - \frac{p^2}{2m} - \frac{P_c p \cos\theta}{2m}\right) \Theta\left(\epsilon_{max} - U(\mathbf{r}) - \frac{P_c^2}{8m} - \frac{p^2}{2m} + \frac{P_c p \cos\theta}{2m}\right)\end{aligned}\quad (\text{A.6})$$

$$X = \cos\theta$$

$$dX = -\sin\theta d\theta$$

Substitute and integrate over  $\phi$

$$\begin{aligned} \tilde{f}_r(\mathbf{p}) &= \left( \frac{1}{2\pi M k_B T} \right)^{3/2} \left( \frac{1}{2\pi \mu k_B T} \right)^{3/2} e^{\left( \frac{-p_r^2}{2\mu k_B T} \right)} 2\pi A^2 \int_{-1}^1 dX \int_0^\infty dP_c P_c^2 e^{\left( \frac{-P_c^2}{2M k_B T} \right)} \\ &\times \Theta \left( \epsilon_{max} - U(\mathbf{r}) - \frac{P_c^2}{8m} - \frac{p^2}{2m} - \frac{P_c p X}{2m} \right) \Theta \left( \epsilon_{max} - U(\mathbf{r}) - \frac{P_c^2}{8m} - \frac{p^2}{2m} + \frac{P_c p X}{2m} \right) \end{aligned} \quad (\text{A.7})$$

Recognize that the Heaviside functions cancel each other out on either side of zero, so can eliminate one of the Heavisides and multiply by 2

$$\begin{aligned} \tilde{f}_r(\mathbf{p}) &= \left( \frac{1}{2\pi M k_B T} \right)^{3/2} \left( \frac{1}{2\pi \mu k_B T} \right)^{3/2} e^{\left( \frac{-p_r^2}{2\mu k_B T} \right)} 4\pi A^2 \int_0^1 dX \int_0^\infty dP_c P_c^2 e^{\left( \frac{-P_c^2}{2M k_B T} \right)} \\ &\times \Theta \left( \epsilon_{max} - U(\mathbf{r}) - \frac{P_c^2}{8m} - \frac{p^2}{2m} - \frac{P_c p X}{2m} \right) \end{aligned} \quad (\text{A.8})$$

From here we can rewrite using the infinite relative momentum probability distribution  $f_{r,\infty}(\mathbf{p})$  from some equation

$$\begin{aligned} \tilde{f}_r(\mathbf{p}) &= \left( \frac{1}{2\pi \mu k_B T} \right)^{3/2} e^{\left( \frac{-p_r^2}{2\mu k_B T} \right)} \mathcal{G}(T, \epsilon_{max}, p_{rel}) \\ &= f_{r,\infty}(\mathbf{p}) \mathcal{G}(T, \epsilon_{max}, p_{rel}) \end{aligned} \quad (\text{A.9})$$

where  $\mathcal{G}(T, \epsilon_{max}, p_{rel})$  is given by

$$\begin{aligned} \mathcal{G}(T, \epsilon_{max}, p_{rel}) &= A^2 \left( \frac{4\pi}{2\pi M k_B T} \right)^{3/2} \int_0^1 dX \int_0^\infty dP_c P_c^2 e^{\left( \frac{-P_c^2}{2M k_B T} \right)} \\ &\times \Theta \left( \epsilon_{max} - U(\mathbf{r}) - \frac{P_c^2}{8m} - \frac{p^2}{2m} - \frac{P_c p X}{2m} \right) \end{aligned} \quad (\text{A.10})$$

Now define two dimensionless variables  $\tilde{\epsilon}$  and  $\tilde{E}$  which will be used to change variables once more

$$\begin{aligned}
\tilde{\epsilon} &= \frac{p_{rel}^2}{2\mu k_B T} & \tilde{E} &= \frac{P_c^2}{2Mk_B T} \\
p &= \sqrt{2\mu k_B T \tilde{\epsilon}} & P_c &= \sqrt{2Mk_B T \tilde{E}} \\
dpp^2 &= \frac{\sqrt{\tilde{\epsilon}}}{2} (2\mu k_B T)^{3/2} d\tilde{\epsilon} & dP_c P_c^2 &= \frac{\sqrt{\tilde{E}}}{2} (2Mk_B T)^{3/2} d\tilde{E}
\end{aligned}$$

Plugging these expressions into Eq.A.10 and rearranging

$$\begin{aligned}
\tilde{f}_{\mathbf{r}}(\mathbf{p}) &= A^2 \frac{e^{-\tilde{\epsilon}}}{(2\pi\mu k_B T)^{3/2}} \int_0^1 dX \frac{2}{\sqrt{\pi}} \int_0^\infty d\tilde{E} e^{-\tilde{E}} \sqrt{\tilde{E}} \\
&\quad \times \Theta \left( \eta(\mathbf{r}) - \frac{\tilde{E}}{2} - \frac{\tilde{\epsilon}}{2} - X\sqrt{\tilde{E}\tilde{\epsilon}} \right) \quad (\text{A.11})
\end{aligned}$$

would like to turn this distribution into a relative energy distribution. Collisions are isotropic so we can use the relation

$$\begin{aligned}
\int dpp^2 \int d\Omega_p \tilde{f}_{\mathbf{r}}(\mathbf{p}) &= \int d\tilde{\epsilon} \hat{f}_{\mathbf{r}}(\tilde{\epsilon}) = 1 \\
\Rightarrow 4\pi p^2 \tilde{f}_{\mathbf{r}}(\mathbf{p}) dp &= \hat{f}_{\mathbf{r}}(\tilde{\epsilon}) d\tilde{\epsilon} \quad (\text{A.12})
\end{aligned}$$

using  $dpp^2$  given above we then write

$$\hat{f}_{\mathbf{r}}(\tilde{\epsilon}) = A^2 \sqrt{\tilde{\epsilon}} e^{-\tilde{\epsilon}} \frac{2}{\sqrt{\pi}} \int_0^1 dX \frac{2}{\sqrt{\pi}} \int_0^\infty d\tilde{E} e^{-\tilde{E}} \sqrt{\tilde{E}} \Theta \left( \eta(\mathbf{r}) - \frac{\tilde{E}}{2} - \frac{\tilde{\epsilon}}{2} - X\sqrt{\tilde{E}\tilde{\epsilon}} \right) \quad (\text{A.13})$$

We can now choose the normalization constant  $A^2$  using

$$\int_0^{2\eta(\mathbf{r})} d\tilde{\epsilon} \hat{f}_{\mathbf{r}}(\tilde{\epsilon}) = 1$$

where we have used an energy cutoff of  $2\eta(\mathbf{r})$  since either particle may have an energy in the range  $[0 \rightarrow \eta(\mathbf{r})]$ . With the normalization, the complete expression for  $\hat{f}_{\mathbf{r}}(\tilde{\epsilon})$  is then

$$\hat{f}_{\mathbf{r}}(\tilde{\epsilon}) = \frac{2}{\sqrt{\pi}} \sqrt{\tilde{\epsilon}} e^{-\tilde{\epsilon}} \hat{\mathcal{G}}(\eta_{\mathbf{r}}, \tilde{\epsilon}) \quad (\text{A.14})$$

where all the effects of the truncation have been moved to  $\hat{\mathcal{G}}$ , given by

$$\hat{\mathcal{G}}(\eta_{\mathbf{r}}, \tilde{\epsilon}) = \frac{\int_0^1 dX \frac{2}{\sqrt{\pi}} \int_0^\infty d\tilde{E} e^{-\tilde{E}} \sqrt{\tilde{E}} \Theta \left( \eta(\mathbf{r}) - \frac{\tilde{E}}{2} - \frac{\tilde{\epsilon}}{2} - X \sqrt{\tilde{E}\tilde{\epsilon}} \right)}{\int_0^{2\eta(\mathbf{r})} d\tilde{\epsilon} \frac{2}{\sqrt{\pi}} \sqrt{\tilde{\epsilon}} e^{-\tilde{\epsilon}} \int_0^1 dX \frac{2}{\sqrt{\pi}} \int_0^\infty d\tilde{E} e^{-\tilde{E}} \sqrt{\tilde{E}} \Theta \left( \eta(\mathbf{r}) - \frac{\tilde{E}}{2} - \frac{\tilde{\epsilon}}{2} - X \sqrt{\tilde{E}\tilde{\epsilon}} \right)}$$

we can check the limiting behavior of this equation since we expect when

$$\lim_{\eta \rightarrow \infty} \hat{\mathcal{G}}(\eta_{\mathbf{r}}, \tilde{\epsilon}) = 1$$

. Indeed, remembering that

$$\int_0^\infty dx \sqrt{x} e^{-x} = \frac{\sqrt{\pi}}{2}$$

then this requirement is fulfilled.

## Appendix B

### Imagefit analysis routine

”Lorem ipsum dolor sit amet, consectetur adipiscing elit, sed do eiusmod tempor incididunt ut labore et dolore magna aliqua. Ut enim ad minim veniam, quis nostrud exercitation ullamco laboris nisi ut aliquip ex ea commodo consequat. Duis aute irure dolor in reprehenderit in voluptate velit esse cillum dolore eu fugiat nulla pariatur. Excepteur sint occaecat cupidatat non proident, sunt in culpa qui officia deserunt mollit anim id est laborum.”

General procedure, should probably suggest moving to Github and warn about software migration breaking older versions of code.

Currently everything is working in 2015b? Can it work in a newer version?

#### B.1 Background removal

Covers *imagefit\_Background\_PCA*

Would like to remove noisy fringes to fit more easily

##### B.1.1 Principal component analysis

be sure to discuss tradeoffs such as matrix size, basis size, and number of images

The Anderson and Cornell groups have adapted two statistical techniques used in astronomical data processing to the analysis of images of ultracold atom gases.

Image analysis is necessary for obtaining quantitative information about the behavior of an ultracold gas under different experimental conditions. Until now, the preferred method has been to find a shape (such as a Gaussian) that looks like the results and write an image-fitting routine to probe a series of photographs. The drawback is that information extracted this way will be biased by the model chosen.

The two groups recently employed model-free analysis techniques to extract results from interferometry experiments on Bose-Einstein condensates (BECs). The statistical processing techniques were able to rapidly pinpoint correlations in large image sets, helping the researchers uncover unbiased experimental results. Using the techniques, graduate student Steve Segal, former graduate student Quentin Diot, Fellows Eric Cornell and Dana Anderson, and a colleague from Worcester Polytechnic Institute calibrated their interferometer, identified and mitigated some noise sources, and unearthed signal information partially buried in the noise generated during the BEC experiment. By looking for correlations and relationships between pixels in a series of images (a), the researchers were able to clearly "see" changes in the overall number of atoms (d), changes in the vertical positions of three peaks in a momentum distribution (c), and changes in the fraction of atoms in the central peak (b), which was the primary experimental signal.

The results were obtained with principal component analysis (PCA) and independent component analysis (ICA). PCA identified simple pixel correlations and looked for areas of maximum variance. Such areas provided an idea about where to look for changes in size, structure, or position of the ultracold atom cloud. The PCA analysis was sufficient for calibrating the interferometer and debugging the experiment. It also provided an idea of size changes in one or more features of the experiment. However,

the PCA analysis alone wasn't perfect. ICA was required to extract the most important information about the experiment, i.e., the fraction of the total number of atoms in one of three clouds. Using preprocessed data from a PCA analysis, ICA was able to test whether the values of neighboring pixels were statistically independent from one another. With this information, ICA could then determine relative differences in the experimental signal and separate its individual features.

Segal thinks physicists in the ultracold atomic physics field will be intrigued by the potential of using the PCA and ICA techniques to probe their experimental images. There are only two caveats: The techniques require 10–100 images, and their application to ultracold atom-cloud experiments is still in its infancy. - Julie Phillips

### B.1.2 Comparison of PCA implementations

## B.2 Fitting the spatial distribution

Covers *imagefit\_NumDistFit*

## B.3 Evaluating fit parameters

Covers *imagefit\_ParamEval*

### B.3.1 Writing new plug-ins

### B.3.2 Suggested improvement

Move all data structures (or at least the experimental plugin ones) to be table based so that everything is held at the same level. This would make it much easier to be

flexible with different analyses (since you're not imposing a structure that might be restrictive later)

One of the key lessons I've learned is to be flexible when starting new projects. You don't know where the data is going to take you or what may come up as an interesting/useful perspective for developing and questioning hypotheses. Tables are a scheme that I've have realized are very common in data management and analysis. The popular python package Pandas, uses datatables exclusively and was the impetus for my interest in the data structure. Tables also make it easy to export and share your data via spreadsheet applications (assuming you use simple datatypes within each cell) Lastly, this is a warning that no matter what you end up doing with the data, you will inevitably have to spend time organizing and reorganizing it at times. With less structure imposed on the data you'll be able to manipulate things more easily and (most importantly to Tom) more quickly.

## Appendix C

### **neuKLEIN - Killian lab experimental interface**

During my time working on the neutral apparatus, Joe Whalen began a rewrite of the Labview based experimental control software which had grown organically through the first decade of the neutral apparatus' existence. Following this refactor, the user interface was also revamped to help reduce human errors and improve overall data collection efficiency. This chapter will outline the major components of the neuKLEIN software package and how this system integrates with the hardware control system and the software analysis algorithm.

#### **C.1 Labview code**

Need to have description of state machine.

Need to

Use of references for updating front panel

Need to get references for LV documentation for this stuff

Discuss triggered waveform oddity (retriggerable setup)

#### **C.2 FPGA code**

The versatility of FPGA led us to want to simple system for setting static voltages and switching them at will. We built such a system using an National Instrument

FPGA device (Xilinx something). The hardware details and circuitry are available in [appendix blah](#). This section will focus on the software side of programming and using the FPGA system.

This was originally a project started by a summer student named Weixuan Li in summer 2018. He did a good job.

Talk about special programs (the custom operation builder specifically)

### C.3 Possible future improvements

Specifically thinking about the ability to do network shared variables. Then we could dedicate a machine to an instrument and share the data using a networking layer instead of a hard connection.

Movement to full state machine

Standardization of the triggered waveform VI

implementation of coupled scanning mechanism (how is this currently handled)

## Appendix D

### Experimental control computer hardware

”Lorem ipsum dolor sit amet, consectetur adipiscing elit, sed do eiusmod tempor incididunt ut labore et dolore magna aliqua. Ut enim ad minim veniam, quis nostrud exercitation ullamco laboris nisi ut aliquip ex ea commodo consequat. Duis aute irure dolor in reprehenderit in voluptate velit esse cillum dolore eu fugiat nulla pariatur. Excepteur sint occaecat cupidatat non proident, sunt in culpa qui officia deserunt mollit anim id est laborum.”

#### D.1 Overview of status

#### D.2 Migration to a new machine

#### D.3 PixelFly camera system

What is the datasheet? Where are the drivers? What OS is it compatible with?

Double shot system, the difference in camera exposure times, how we mitigate that difference and what errors might result because of this timing.

Get the double shot timing diagram.

Somewhere I need to talk about the discretization (in time) of the lattice card as it is not obvious

## Appendix E

### Neutral apparatus

”Lorem ipsum dolor sit amet, consectetur adipiscing elit, sed do eiusmod tempor incididunt ut labore et dolore magna aliqua. Ut enim ad minim veniam, quis nostrud exercitation ullamco laboris nisi ut aliquip ex ea commodo consequat. Duis aute irure dolor in reprehenderit in voluptate velit esse cillum dolore eu fugiat nulla pariatur. Excepteur sint occaecat cupidatat non proident, sunt in culpa qui officia deserunt mollit anim id est laborum.”

#### E.1 Opening vacuum - data and process

#### E.2 Nozzle redesign - neuNozzle 2018

Data about firerod I had some trouble finding the part number associated with the firerod in the Neutral chamber but luckily I found one of the broken firerods still had it's part number on it, SK7J-2953. Below is the info from Valin Corporation who seems to be the local reseller of Watlow products.

SPECIAL DIAMTER HT FIREROD T/C CENTER CORE LOC “A” TYPE “J”  
 120 Volts 240 watts 0.580 +/- 0.004 Diameter firerod 7.5” length 12” of MGT  
 leads 12” of TC leads 6 13/32” of no heat section at lead end. Crimped of leads  
 construction.

Don't forget the plan was to incorporate a design feature from Plasma's nozzle

redesign which addressed the fragility of the feedthrough connection to the heater wire. This was a problem because the heater wire connection is very thin and we used large clamp type connection for them before which was problematic due to the fragility of the heater wire and the necessity that the bulky clamp couldn't touch the nozzle body (as this would short the heater connection). The new connection would allow us to use a smaller crimp to the heater wire, use the rigidity of the feedthrough itself, and use alumina screws to insulate the connection from the nozzle body.

Other reason for redesign was to attach the heat shield directly to the flange.

All the pieces were ordered and built but a mistake on turning the nozzle body meant that we couldn't use the nozzle we built. As of April 2019, this construction is located in [somewhere](#)

## Appendix F

### Gaussian Beam Programs

”Lorem ipsum dolor sit amet, consectetur adipiscing elit, sed do eiusmod tempor incididunt ut labore et dolore magna aliqua. Ut enim ad minim veniam, quis nostrud exercitation ullamco laboris nisi ut aliquip ex ea commodo consequat. Duis aute irure dolor in reprehenderit in voluptate velit esse cillum dolore eu fugiat nulla pariatur. Excepteur sint occaecat cupidatat non proident, sunt in culpa qui officia deserunt mollit anim id est laborum.”

#### F.1 Simple beam propagation

Talk about normal ABCD matrix formalism and then extend to the M2 idea

#### F.2 Laser beam profile fitting

##### F.2.1 Data taking template

Give the data taking template here

Include a figure with all the distance measured off

Pictures of the profiler head and the important distance (I think this is in the manual on the drobo)

## Appendix G

### Concise derivation of effective volumes

The following derivation is meant to serve as a quick reference for finding the analytic form of the effective volumes for ultracold gases held in a optical dipole trap. This section follows the arguements presented by Mi's paper which considers and numerically evalutes the general case of power-law potentials and the corresponding ddensity distribution at arbitrary temperatures less than the trap depth.

If instead one restricts to the experimentally reasonable conditions of high- $\eta$  (recall  $\eta$  is the ratio of trap depth to sample temperature,  $\eta = \epsilon_t/k_B T$ ) and harmonic trapping potentials, then a useful analytic expression can be found for the effective volumes of the gas.

Following eff volume derivation from first year

## Appendix H

### Repair of 922 Lynx master

”Lorem ipsum dolor sit amet, consectetur adipiscing elit, sed do eiusmod tempor incididunt ut labore et dolore magna aliqua. Ut enim ad minim veniam, quis nostrud exercitation ullamco laboris nisi ut aliquip ex ea commodo consequat. Duis aute irure dolor in reprehenderit in voluptate velit esse cillum dolore eu fugiat nulla pariatur. Excepteur sint occaecat cupidatat non proident, sunt in culpa qui officia deserunt mollit anim id est laborum.”

## Appendix I

### Custom circuitry

”Lorem ipsum dolor sit amet, consectetur adipiscing elit, sed do eiusmod tempor incididunt ut labore et dolore magna aliqua. Ut enim ad minim veniam, quis nostrud exercitation ullamco laboris nisi ut aliquip ex ea commodo consequat. Duis aute irure dolor in reprehenderit in voluptate velit esse cillum dolore eu fugiat nulla pariatur. Excepteur sint occaecat cupidatat non proident, sunt in culpa qui officia deserunt mollit anim id est laborum.”

#### I.1 AC line zero crossing trigger

#### I.2 Hard drive shutters

#### I.3 Power locks

#### I.4 Photodiodes

#### I.5 Infinite sample and hold

##### I.5.1 Reduced intensity fluctuations for sub-hertz exposures

Don't forget to talk about whatever noise I observed. I think there is a picture on my phone of this.

## Appendix J

### Miscellaneous tips and tricks

”Lorem ipsum dolor sit amet, consectetur adipiscing elit, sed do eiusmod tempor incididunt ut labore et dolore magna aliqua. Ut enim ad minim veniam, quis nostrud exercitation ullamco laboris nisi ut aliquip ex ea commodo consequat. Duis aute irure dolor in reprehenderit in voluptate velit esse cillum dolore eu fugiat nulla pariatur. Excepteur sint occaecat cupidatat non proident, sunt in culpa qui officia deserunt mollit anim id est laborum.”

#### J.1 Alignment of GHz AOM

#### J.2 Using the Picoscope in Labview(TM)

#### J.3 Liquid crystal retarder

#### J.4 Newport(TM) optomotion control

#### J.5 Fast analog lock for 689 nm

#### J.6 Porta CoM technique

#### J.7 Measuring Rabi frequencies

#### J.8 CAD drawing for shallow angle Bragg setup